Transport phenomena on the molecular and subcellular scale

On molecular spiders, limited resources, and motor-motor interactions

Matthias Rank

München 2017

Transport phenomena on the molecular and subcellular scale

On molecular spiders, limited resources, and motor-motor interactions

Matthias Rank

A dissertation
submitted to the Faculty of Physics at the
Ludwig–Maximilians–Universität München
for the degree of

DOCTOR RERUM NATURALIUM

München, 14 December 2017

First Referee: Prof. Dr. Erwin Frey
Second Referee: Prof. Dr. Ulrich Gerland
Date of the oral examination: 15 January 2018

Zusammenfassung   (German summary)

Das Verständnis von Transportphänomenen auf molekularer und subzellulärer Ebene ist wichtig für essenzielle Prozesse wie Zellteilung oder -migration. Eine zentrale Rolle kommt dabei Molekularen Motoren zu, die auf den Filamenten des Zytoskeletts gerichtete Bewegung verrichten. In dieser Doktorarbeit präsentiere ich Resultate zu drei Projekten, die wesentliche Aspekte von Transportphänomenen behandeln: I Das Entstehen von gerichtetem Transport, II dessen Einfluss auf die Regulierung der Längen der Filamente, sowie III die Rolle von Interaktionen zwischen Molekularen Motoren für das kollektive Transportverhalten.

I Gruppen von Molekularen Spinnen als Prototyp für kooperierende Molekulare Motoren

Im ersten Teil dieser Arbeit befassen wir uns mit künstlich hergestellten Molekularen Motoren, sogenannten Molekularen Spinnen, die ihre gerichtete Bewegung durch die enzymatische Reaktion mit einem DNA-Substrat erreichen. Wir haben herausgefunden, dass essenzielle Transporteigenschaften verbessert werden können, wenn mehrere Spinnen zu einer inelastisch gekoppelten Gruppe kombiniert werden. Durch eine Aufteilung in Phasen gerichteter und diffusive Bewegung entwickeln wir eine mathematische Theorie, mit der wir eine optimale Kopplungsstärke vorhersagen können, bei der sich die Spinnen beinahe ballistisch bewegen.

II Die Rolle endlicher Volumina für die Längenregulation von Mikrotubuli

Im zweiten Teil wird die Rolle von Molekularen Motoren des Typs Kinesin-8 für die Längenregulation von Mikrotubuli in endlichen Volumina untersucht. Wir betrachten die Auswirkungen zweier ressourcenlimitierter antagonistischer Prozesse, nämlich Polymerisation und Depolymerisation der Mikrotubuli, indem wir den Transport von Motoren mithilfe eines Gittergasmodells beschreiben. Ein zentrales Ergebnis unserer Arbeit ist, dass drei verschiedene regulatorische Regimes existieren, in denen die Länge der Mikrotubuli entweder von den Motoren oder der Verfügbarkeit der Proteine kontrolliert wird, oder beide Verhalten gleichermaßen möglich sind. Dieses Verhalten resultiert heuristisch betrachtet von einer unterschiedlichen Verknappung von Motoren und Tubulin aufgrund deren erheblich verschiedener Anzahl. Mithilfe einer Mean-Field-Theorie und Monte-Carlo-Simulationen führen wir eine umfangreiche theoretische Analyse des Verhaltens durch. Um insbesondere die physiologische Signifikanz bistabiler Längenregulation zu untersuchen, werden im Anschluss Ergebnisse einer Reihe von *in vitro* Experimenten dargestellt, die einer Kollaboration entstammen. Unter anderem zeigen wir somit, dass Bistabilität zu einer bimodalen Verteilung der Längen von Mikrotubuli führt.

III Die Bedeutung von Interaktionen zwischen Motoren für deren kollektiven Transport

Da sich eine große Zahl von Molekularen Motoren und anderen Proteinen auf Mikrotubuli befinden, ist es wichtig, deren Interaktionen miteinander und den Effekt auf den kollektiven Transport zu untersuchen. Wir betrachten daher im letzten Teil dieser Arbeit ein Gittergasmodell, bei dem Motoren des Typs Kinesin-1 ihre Bindungsstärke an Mikrotubuli gegenseitig beeinflussen. Wir beobachten, dass durch diese Interaktion die Motorendichte auf Mikrotubuli gesenkt, aber gleichzeitig deren Fluss erhöht werden kann. Indem wir experimentell zugängliche Observablen definieren, erhalten wir in einem Vergleich mit Daten aus einem veröffentlichten *in vitro* Experiment quantitative Übereinstimmung. Dadurch können wir auch auf die individuellen Eigenschaften eines Motors rückschließen und finden unter anderem, dass Kinesin gelegentlich vorübergehend inaktiv wird. Auf diese Art kann somit auf minimal invasive Weise ein Einblick in den Schrittmechanismus dieses Motors gewonnen werden.

Overview of the thesis

In this thesis, I consider different aspects of transport phenomena on the molecular and subcellular scale, which are important for essential processes ranging from cell division to muscle contraction. This work is organised into three parts corresponding to the different projects which I have investigated during my doctoral studies. I will provide a brief overview of these projects in the following. A more detailed summary is presented in the next chapter.

I Teams of molecular spiders: a model for groups of molecular motors — *with Louis Reese, and Erwin Frey.*

The first part of this thesis deals with molecular spiders, which are artificially constructed molecular motors. We examine how the coupling of several spiders to a team impacts their transport dynamics. A mathematical analysis is developed which allows us to predict coupling parameters which optimise the collective dynamics of spider teams. The results of this project have been published under the title "Cooperative effects enhance the transport properties of molecular spider teams" in *Physical Review E, 87, 3 (2013)* (1); I contributed to this publication as first author. A reprint is included in this thesis.

II The impact of finite resources for microtubule length regulation by molecular motors — *with Aniruddha Mitra, Louis Reese, Stefan Diez, and Erwin Frey.*

A project on a molecular motor from the kinesin-8 family, which is known to depolymerise microtubules, constitutes the second part of this work. We are specifically interested in how finite volumes and limitation of resources impact the transport dynamics of the motors and the stationary state properties of the filament. In Chapter 6, we follow a combined theoretical and experimental approach and find that microtubule length regulation is bistable for a certain concentration regime. The findings derived here have been published in *Physical Review Letters, 120, 148101 (2018)* (2) under the title "Limited Resources Induce Bistability in Microtubule Length Regulation". For this letter, I share co-authorship with Aniruddha Mitra from the group of Stefan Diez (Dresden), who conducted the experiments. The presentation of this project is completed in Chapter 7, where we report on a simplified model, which shows the same phenomena, but can be analysed in a more extensive form.

III Motor-induced unbinding: the role of interactions for the collective dynamics of molecular motors — *with Erwin Frey.*

In the last part of this thesis, we present results obtained in the context of a project on the molecular motor kinesin-1. Our focus lies on the interactions of motors with each other. The model predictions compare well with experimental data, and we can therefore infer information on the stepping behaviour of individual motors from their collective transport dynamics. The results shown in this part are currently considered for publication in *Biophysical Journal*; I will be the first author of this publication. A preprint with the title "Crowding and pausing strongly affect dynamics of kinesin-1 motors along microtubules" is available at *arXiv:1805.03432* (3).

Abstracts of the projects

Intracellular transport is vital for the functioning of a cell. So-called *molecular motors* play a crucial role for a wide range of processes from muscle contraction over cell migration to cell division. For example, motors of the kinesin families use *microtubules* (MTs), long filamentous polymers, as molecular tracks, along which they perform directed motion (4, 5). In a complex interplay between MTs, molecular motors, and other proteins, the mitotic spindle is formed which orchestrates the segregation of chromosomes into the daughter cells during cell division (6, 7).

The projects presented in this thesis have been inspired by *in vitro* studies. These experiments provide deep insight into the biophysical processes, because they allow that the role of individual proteins is examined without their interference with other proteins. Here, we focus on three aspects of molecular motors and transport phenomena on the molecular and subcellular scale. In Part I, the results of a study on an artificial molecular motor are presented. While the origin of the biased motion of these *molecular spiders* has been characterised previously (8, 9), our specific goal here is to analyse the stepping behaviour of teams of molecular spiders as a prototypic model of the motion of groups of molecular motors (10). In Part II of this work, we turn to the collective dynamics of a specific molecular motor of the *kinesin-8* family, which has been observed to shrink MTs. Our specific interest lies in the impact of finite resources on the dynamics of the motors and the MT. In the last part of this thesis, Part III, we consider interactions of *kinesin-1* motors with each other. More specifically, we examine a motor-induced unbinding process which is based on experimental findings, and explore its implications on the collective transport and individual motion of molecular motors.

I Teams of molecular spiders: a model for groups of molecular motors   In order to understand how molecular motors function, a particularly fruitful approach has been to create recombinant molecular motors, or to construct artificial molecular motors from scratch (11). In such constructions, motors can be equipped with well-defined properties. The impact of these properties on the individual and collective motion of the motors can subsequently be studied. With recent advances in DNA nanotechnology, so-called molecular spiders have been constructed (12, 13). These spiders bind to and enzymatically cleave a substrate, which can be tuned in a way that the binding of spiders to the original substrate is stronger than to its cleaved form. As a consequence, spiders can distinguish between sites where they have already been, and previously unvisited sites. It has been shown (8, 9) that this memory effect leads to biased motion, as long as the spider remains at the interface between visited and unvisited sites.

In the project presented here, we consider a model of a group of multiple molecular spiders, where the spiders comprising a "team" are coupled via an inelastic "leash". We find in simulations that spider teams move superdiffusively; the motion of some large teams becomes almost ballistic. The runs of spider teams can be classified into boundary periods where they move in a biased

fashion, and diffusive periods where they have lost contact to the interface between cleaved and uncleaved sites. We develop a mathematical theory in which both these cases are considered. An insightful quantity to characterise boundary periods is the average number of steps for which the spider team remains in contact with the boundary and therefore can utilise the bias. In the limit where the time scales for spider stepping and the cleaving of a substrate separate, a combinatorial approach leads to exact expressions for this quantity. For the diffusive periods, we obtain a mapping of the one-dimensional motion of a team comprising n spiders to the diffusive motion of a single particle in an n-dimensional constrained environment. Furthermore, we conclude that the team's coupling strength is crucial to achieve and maintain significantly biased motion. This is due to the payoff between the ability to explore previously unvisited sites, and the prevention of retracting to the domain of cleaved substrates. Our theoretical understanding allows us to determine the optimal coupling strength of a spider team depending on its size, at which the bias becomes maximal and the motion is least random.

In a broader context, our study shows the importance of team work for efficient and directed transport on the nanoscale, where diffusion is dominant. It is therefore also prototypic for the collective motion of groups of molecular motors, as found inside cells.

It will be interesting to see in the future how our findings compare with real molecular motors (10, 14–18). Furthermore, the role of cooperativity between motors as a design principle for novel artificial motors (11) will need to be studied in more detail, and in an interdisciplinary context of theoretical physics, chemistry, and engineering.

The project which is presented in this work has been published under the title "Cooperative effects enhance the transport properties of molecular spider teams" in *Physical Review E, 87, 3 (2013)* (1). A reprint of the publication is included in this thesis.

II The impact of finite resources for microtubule length regulation by molecular motors

Tight regulation of the length of microtubules (MTs) is important for the assembly of the mitotic spindle (19). Many proteins are involved in this process through a complex interplay. These proteins include molecular motors of the kinesin-8 family, which are known to depolymerise MTs at their plus ends. In *in vitro* experiments (20, 21), as well as in theoretical studies (22, 23), it has previously been found that a motor density gradient — arising from the combined effect of random motor attachment to the MT, and directed motion on it — leads to a mechanism for how these polymers can regulate their length.

Based on experimental observations that the formation of the mitotic spindle depletes the concentration of protein (24, 25), we extend and refine an earlier model (22, 23). In Chapter 6, we describe the motion of molecular motors on a MT in terms of a driven lattice gas with a dynamically changing lattice length. The role of limited resources is specifically taken into account by assuming that the motor attachment rate to the MT, as well as the MT elongation rate, depend on the availability of motors and tubulin dimers in the cytosol, respectively. It is found in Monte Carlo simulations that three regulatory regimes exist: a regime where depolymerisation dominates, i.e., where motors control the length of the (hence short) MTs; a second regime which is dominated by polymerisation: here, the availability of tubulin determines MT length; and a bistable regime where both behaviour is possible. We derive an effective description of the model in terms of the TASEP/LK. The collective dynamics are obtained from a mean-field theory, and

we find good agreement with simulation data. This allows us to associate the different regulatory regimes of MT length with specific phases of the collective motion. In order to test the theoretical predictions, we subsequently present a set of *in vitro* experiments, conducted in the group of Stefan Diez (Dresden). These experiments confirm our key results. In particular we find that MTs with two specific lengths coexist for certain concentrations. The correspondence of these bimodal length distributions with our theoretical understanding of bistabile length regulation is argued via a separation of length scales: At stationarity, MTs in spatial proximity, so close that they share a common pool of resources, assume the same length. In contrast, distant MTs behave independently, and may therefore evolve towards the different fixed points of the bistable system.

In the second part of this project, Chapter 7, we consider a simplified model where attachment and detachment of motors is possible only at the MT ends. This model has the advantage that a full theoretical analysis is possible without having to rely on numerical methods, while all essential phenomena of the full model are maintained. We derive a closed set of expressions from which the existence of a bistable regime follows inevitably. This also allows us to uncover the prerequisite of bistability on a heuristic level: In particular, we argue that bistability results from a differential shortage of resources at different MT lengths, and therefore demands that motors and tubulin dimers are available at vastly different concentrations.

On a broader perspective, phenomena such as bistability are important also because they change the nature of phase transitions: We show explicitly that, in the absence of a bistable phase, MT length changes continuously with protein concentrations, whereas discontinuous phase transitions are observed as bistability sets on. The changes of the phase transition may be of particular importance in the cell cycle, where flexible and quick adaption of certain physical properties such as MT length are important. Our study is exemplary for a system where two volume-limited processes compete with each other, and is not limited to the specific *in vitro* case here. It reveals how emergent phenomena arise in a very simple setting when resources are limited.

Future studies will need to include the role of diffusion of protein between MTs more explicitly, as in this work, only the limits of isolated and well-mixed systems, respectively, were examined. Such investigations will draw upon insights from both the fields of motor dynamics on MTs, as well as reaction-diffusion models. This research promises to uncover fascinating phenomena such as Turing instabilities, and hence provide links to different research topics such as Min oscillations (26). Furthermore, the role of our findings for *in vivo* systems, the mitotic spindle, or the cell, has not been considered in this thesis. In fact, it has been observed that the length distribution of MTs inside spindles is bimodal (27), but the exact reasons are unresolved. We believe that our generic model setup, comprising two antagonistic, resources-limited processes, is applicable also to filaments showing, e.g., dynamic instability (28), but this will need to be critically tested in the future. Moreover, additional research on the role of different types of motors, influencing MT length in a different way, needs to be undertaken. An essential prerequisite for advances in these directions will be close communication of theory and experiment.

At the time of the original submission of this thesis, a manuscript containing the first part of the project presented here had been under review for publication. While preparing the final version of this work, the manuscript has been accepted and published in *Physical Review Letters, 120, 148101 (2018)* (2). The *in vitro* experiments are result of a very fruitful collaboration with Aniruddha Mitra and Stefan Diez, which I initiated during the course of my doctoral studies.

III Motor-induced unbinding: the role of interactions for the collective dynamics of molecular motors   The ability to achieve efficient transport is a central characteristic of kinesin-1, a molecular motor which is involved in transporting organelles and other cargoes along MTs (29). However, the highly crowded conditions inside cells and on MTs require optimised strategies to circumvent traffic jams, as well as to avoid wasting time and energy. In the last part of this thesis, we report on a project which describes a way how motors may overcome crowding on filaments.

Our study is based on data from a published *in vitro* experiment (30), where it was found that the dwell time of kinesin-1 motors decreases on crowded filaments. Based on these observations, we consider a dimeric driven lattice gas, where the unbinding of motors from the MT is enhanced when two motors are adjacent. We find that the general effect of this interaction is to reduce the motor density on filaments; thereby it contributes to maximising the motor current. A mean-field theory is developed for the motors' collective dynamics. In the following, we derive experimentally accessible quantities, and find accurate agreement of the model with experimental data (30). An additional model test is imposed from experimental observations that motors occasionally pause on the MT for an extensive time, and that the pauses' frequency depends on the motor concentration (30). Because this behaviour cannot be witnessed in our original model, we hypothesise that kinesin-1 may become inactive stochastically; in effect, the crowding-dependent pausing frequency follows from the emergence of traffic jams behind inactive motors. This indicates that motors align very densely in a traffic jam, with a stoichiometry of one kinesin per tubulin subunit, as opposed to one motor per two tubulin dimers as kinesin moves. Subsequently, an interpretation of the origin of the motor-motor interaction is discussed. We conjecture that motors in the vicinity of other motors remain in a weakly bound state for an extended period of time compared to an unperturbed step. This allows us to estimate the lifetime of this state, and we find that it comprises a significant fraction of kinesin's mechanochemical cycle.

From a broader point of view, the close connection of our theoretical approach with published experimental data represents an appealing example for how properties of individual motors can be obtained from their collective behaviour. Since only a small fraction of the motors was labelled in the experiment used for gauging our model (30), and since no force is exerted on them except for the forces which they apply on each other, our method is minimally invasive, and yet we gain deep insight into the motion of molecular motors.

It will be interesting to see whether and how the implications of our study such as the existence of an inactive mode of kinesin's motion will manifest in future experiments. In addition, the proposed dense alignment of motors in a traffic jam needs to be verified, although experimental data from immobilised kinesin motors support our findings (31). Future theoretical studies describing the details of the collective motion of kinesin-1 motors will explicitly have to take into account recent observations that kinesin function, and in particular their velocity, is heterogeneous (32). This may lead to stop-and-go-like traffic jams (33), and may thus have similar effects as motors that spontaneously become inactive. The methods developed here are not specific to kinesin-1. We therefore hope that our findings will stimulate both experimental and theoretical efforts, and also provide insights into the collective and individual motion of other molecular motors.

By the time the final version of this thesis is being completed, a manuscript containing the results presented in this chapter has been submitted to *Biophysical Journal*, where it is currently under consideration for publication. A preprint is available at *arXiv:1805.03432* (3).

Contents

Introduction

Efficient and optimised transport is important on length scales ranging from astronomical units down to the molecular level. For example, the swing-by method (34) is employed as a strategy to transport space probes outside our solar system with minimal use of propellant. On an intermediate length scale, the search for an economic transport route has led to the discovery of America by Christopher Columbus in 1492 (35). Down on the cellular level, highly complex mechanisms have developed which orchestrate the transport and motion of, e.g., enzymes, proteins, and organelles to their target (7). In this work, we want to focus on two particular components essential for transport on this scale: *Molecular motors*, such as kinesin, are molecular machines that are highly optimised for their function to perform directed motion. They walk on filamentous polymers called *microtubules*, which are involved in the formation of the mitotic spindle that drives cell division.

Many disciplines have worked on various aspects of microtubules (MTs) and molecular motors. Biologists have developed ingenious experiments to illuminate the function and properties of motors and MTs. Chemists have analysed the structure of the involved proteins. Physicists have designed microscopes to observe, and developed models to understand the underlying principles of molecular transport. Computer scientists have established algorithms to test the theoretical methods which mathematicians have derived. Physicians have discovered how the malfunction of the interplay of motors with MTs can create diseases against which pharmacists have developed drugs.

As a consequence, studies on molecular motors and MTs have to deal with these interdisciplinary problems. In this work, we will report on three different projects which all unite various aspects of physics, biology, chemistry, mathematics and computer science. After an introduction we will consider a theoretical model for molecular spiders, which are experimentally established artificial molecular motors, capable of walking along a substrate. Subsequently, we will examine the collective dynamics of molecular motors as they interact with MTs in a volume of finite size; parts of this chapter are the result of a theoretical-experimental collaboration with the group of Stefan Diez (Dresden). In the last part of our work, we will, based on published data of an *in vitro* experiment, in detail shed light on the interactions of molecular motors with each other.

1. Biological background

1.1. Microtubules and the cytoskeleton

Size, shape and function of cells differ enormously between different species and even within an organism. Among the properties which eukaryotic cells have in common is the existence of the cytoskeleton, illustrated in Fig. 1a. It comprises actin filaments, intermediate filaments, and microtubules (MTs). All of these components are involved in different function: Actin shapes the cells and is important for cell migration; intermediate filaments provide mechanical strength to the cell. In this work, we will mostly focus on the third type of filaments: MTs serve as intracellular tracks for the traffic of molecular motors. Hereby, they provide an essential and effective way to transport and position organelles and other macromolecules. The complex interplay of these different types of filaments with each other, and with proteins associated with them, gives rise to fascinating intracellular machineries. A prototypic example is the mitotic spindle, see Fig. 1b, which is crucial for the coordinated segregation of chromosomes into daughter cells. (6)

It was the desire for a deeper understanding of mitosis and especially the mitotic spindle that led to a surge of studies about cytoskeletal filaments, and in particular MTs, in the 1950s (38). By that time, it had been long established that the spindle is composed of "traction fibers". However, it was not before 1951 that Inoué and Dan observed a change of the spindle's birefringence during cell division, which led them to conclude that these filaments are dynamic (39). Borisy and Taylor discovered in 1967 that the "microtubules" (40) are polymers built from subunits (41, 42), termed tubulin (43). At the same time, the structure of MTs became increasingly well characterized: Ledbetter and Porter constrained the diameter of MTs to roughly 25 nm (40), and Roberts discovered that a MT consists of 13 one-dimensional subfilaments (44), called protofilaments. A key property of MTs was brought into focus in a landmark study conducted by Mitchison and Kirschner (28) who discovered that these filaments can undergo dynamic instability, alternating periods of relatively slow elongation and rapid shrinkage of MTs. Since then, novel and more advanced microscopy techniques (45, 46), as well as the emergence of genetic engineering and nanotechnology (47–49), have led to a detailed understanding of many physical properties of MTs.

A sketch of a MT with today's knowledge is shown in Fig. 2. MTs are built from tubulin subunits, heterodimers (50) comprising α- and β-tubulin. These subunits, measuring 8.4 nm (49, 51), align head-to-tail in order to form a protofilament (52). Thirteen of these protofilaments, 14 or 15 for some *in vitro* assembled MTs (53, 54), form the MT. MTs inherit the polarity of tubulin dimers, and therefore possess a plus end (right in Fig. 2) and minus end (left). An important difference between these ends is that — while both ends are dynamic and tubulin dimers can be exchanged with the cytosol — the kinetics of the dynamic processes occurring at the minus end are relatively slow, whereas they are quick at the plus end (52, 55–57).
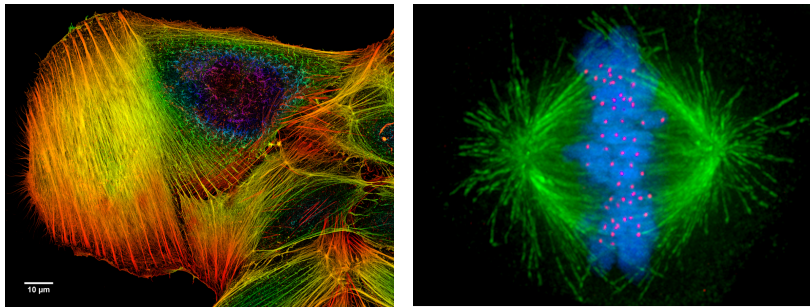
Figure 1.: (a) Actin filaments visualised in a phalloidin stained cancer cell as observed in a confocal microscope. Image published under the Creative Commons Attribution-Share Alike 4.0 International licence (36). (b) Image of the mitotic spindle in a human cell. MTs are shown in green, chromosomes in blue, and kinetochores in red. Source: (37)
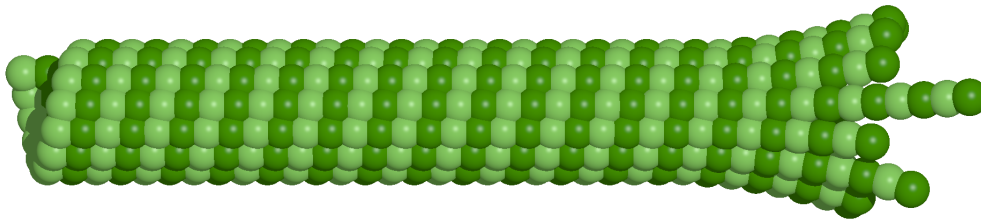
Figure 2.: Sketch of a microtubule (MT). It is built from tubulin which itself comprises α-tubulin (light green) and β-tubulin (dark green). The resulting heterodimers align head-to-tail to form one-dimensional protofilaments, of which (typically) 13 constitute the MT. MTs are polar in the same way as their subunits. The different ends have unequal physical properties: The dynamics at the minus end (left) are relatively slow, while the are fast at the plus end (right).
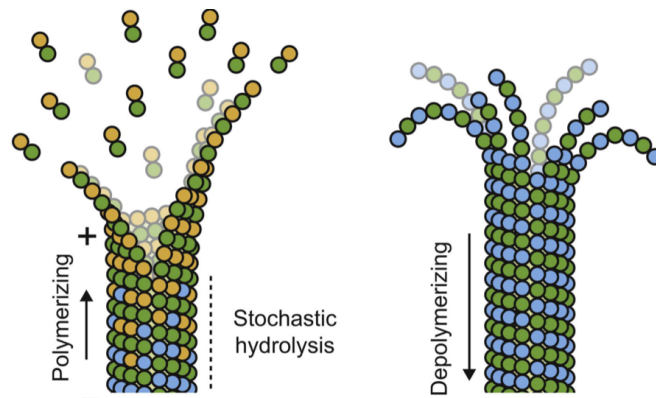
Figure 3.: Polymerising and depolymerising MTs. In the left part, a growing MT is shown. Here, the newly incorporated tubulin subunits are in the GTP state (yellow/green); this has the effect that young protofilaments are relatively straight. As GTP is hydrolysed to GDP (blue/green), tubulin undergoes a conformational change, and the filaments are curved and unstable (right part). Image taken from Ref. (58).

It is also at the plus end where dynamic instability occurs. Although a complete understanding of its physical principles is still missing, it is generally accepted that dynamic instability results from the association of tubulin with a guanosine nucleotide. In particular, as a MT is polymerised, a "cap" of newly added GTP-tubulin (28, 57) is formed at the plus end. This tubulin has a relatively straight conformation (59) so that the longitudinal bonds of newly polymerised protofilaments are stable. Incorporation into the MT triggers the hydrolysis of GTP. The resulting GDP-tubulin is in a bent conformation (59). As a consequence, the longitudinal bonds of GDP-tubulin, artificially held straightly in a protofilament by lateral interactions, are relatively weak. The impact of the conformational difference on the shape of the protofilaments is also visualised in Fig. 3: While GTP-protofilaments, present in particular when MTs are polymerised, are straight and stable (left part of this Figure), GDP-protofilaments (present on depolymerisation) are curved and unstable. It is therefore essential whether or whether not the MT is capped by a layer of GTP-tubulin: When the end of the MT is formed by GTP-tubulin, bonds are stable there and the MT can continue to grow. If the MT stochastically loses its GTP cap, the weakly bound GDP-tubulin, now at the outside of the MT, quickly dissociates from the end, leading to rapid shrinkage ("catastrophe").

Different models for how exactly the loss of the cap occurs, or how hydrolysis is executed, have been suggested. In particular, there has been a long debate (60) about whether hydrolysis of GTP-tubulin occurs randomly (28, 61), vectorially (60, 62–64), or by a mixture of both (65). Similarly, the size of the stabilizing cap has been subject to discussion: Some studies indicated only a short GTP-layer of very few tubulin dimers (66–68), thereby conflicting results of other groups suggesting that the cap should be hundreds of nm long (28, 68, 69). Significant progress on this question has been reported recently, when Gardner et al. found that the exchange of tubulin dimers at the MT plus end happens much more rapidly as thought previously, which strongly hints towards the existence of a long cap (70). A similar conclusion was made by Surrey and coworkers, who made use of the property of the protein EB1 to bind particularly to GTP-tubulin (71). In particular, they observed that the size of the EB1 comet is of the order of several hundred nm (72). The extension of the EB1 binding region shrinks before catastrophe (72) and determines the instantaneous MT stability (68). Altogether, it therefore becomes increasingly evident that MTs are stabilised by a long GTP cap and GTP is hydrolysed randomly.

However, many aspects of MT dynamics and dynamic instability remain unclear. Among these is MT ageing: It has been found (65, 73–76) that catastrophe is not a single-step process, but that probably $\geq$ 3 sub-steps are necessary to reach catastrophe. Also, a mechanical understanding of the longitudinal and lateral interactions within and between protofilaments is missing (77). Furthermore, while it has been observed that MTs are dynamic also inside living cells (78) and probably also show dynamic instability (79), the impact of the large number of MT associated proteins (MAPs) and molecular motors on the dynamic behaviour of MTs is far from being understood (80).

1.2. Molecular motors

A crucial function of MTs and actin filaments is that they serve as intracellular tracks along which so-called molecular motors perform directed motion. Three families of molecular motors can be found inside cells: two of them, namely kinesin and dynein motors, walk on MTs.
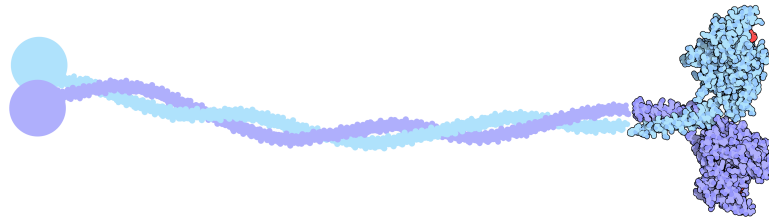
Figure 4.: The structure of kinesin. The two heads are located on the right, the stalk links them to the cargo-binding domain on the left. Image created by David Goodsell and published under the Creative Commons Attribution 3.0 Unported licence (81).

Kinesin is (usually) directed to their plus end (82), and dynein to the minus end (29). Motors of the third type, myosin, move towards the plus end of actin filaments (83). Inside cells, many different motors of these families are present, so that the function of a cell relies on a complex interplay of molecular motors with each other, and with other proteins associated with MTs or actin (83–87). In general, the function of the different motors can be characterised as follows: Kinesin motors are very processive (21, 30), and are therefore ideal for long-range transport, e.g., of organelles (29). Furthermore, some kinesin motors possess catalytic activity which they can develop at the MT plus end (20). Likewise, dynein motors are very processive (88); these motors are involved, amongst other functions, in sliding MTs against each other (89), and the movement of chromosomes (90–93). Motors of the third family, myosin, play a crucial function for transport in membrane protrusion (94), but many motors of this type can only make a single or very few processive steps, unless they act in larger groups (10). Because myosin does for this reason not need to follow a complex coordination cycle of its heads, it is are able to perform fast motion, which is particularly important for example for short-range transport (83), or the contraction of muscles (95).

In this work, we are mostly interested in molecular motors of the kinesin family. Most motors falling into this class have two heads, but also some non-processive monomeric kinesin motors can be found inside cells (82, 96, 97). Fig. 4 shows a sketch of a dimeric kinesin, such as the "conventional" kinesin-1. Its two heads, structurally similar to dynein's heads (98), on the right in this Figure bind to distinct sites on the tubulin dimer; a neck linker between the heads holds them tightly together. The coiled-coiled stalk connects the motor domain to the motor's tail, where cargoes can be attached (99). The impact of the structure of kinesin on its motility properties has been investigated by creating recombinant kinesin (96, 100), as well as introducing genetic modifications of its components. In particular, it has been found that the neck linker is crucial for a kinesin step: Disruption of the stability of kinesin's neck domain causes the motor to spiral around the MT (101, 102). Similarly, variations of the length of the neck linker modulate processivity and velocity of the motors (100, 103). In contrast, removing wide parts of the motor's tail conserves kinesin's kinetic parameters (30, 104, 105).

As a result, kinesin motors of different types, despite having similar heads, have differential physical properties: for example, kinesin-2 (101) and kinesin-8 (106, 107) occasionally side-step to neighbouring protofilaments. In contrast, kinesin-1 walks straight, i.e., along to a MT's protofilament (108), and therefore requires special strategies to circumvent obstacles on the MT (30, 109).

Among all kinesin motors, also motor velocity and processivity vastly differs. For instance, kinesin-1 is very fast but walks only for a few hundred steps (30), while kinesin-8 is slow by comparison but virtually never detaches from the MT before reaching its plus end (21).

A critical question which may ultimately help to unravel the origin of the differences of kinesin's motility is how exactly a step of kinesin functions. By now it has been established that kinesin follows a hand-over-hand mechanism (110, 111), and during a step hydrolyses a single molecule of ATP (112). However, the exact transitions between a two-head-bound (2HB) state into a transient one-head-bound (1HB) state, and back to the 2HB state one site progressed, are very controversial (113). In particular, disagreement is found in the literature about the moment of ATP binding to the rear head: Some groups report that the rear head dissociates from the MT followed by ATP binding (114–117), while other studies suggest the opposite (103, 111), see Ref. (113) for an overview. Similarly, it is not clear how the neck linker binds to the MT, and whether ATP binding to the head is sufficient for its binding (118) or not (100, 119, 120). Furthermore, the reported kinetics of the individual substeps differ vastly: Conflicting results have been reported considering the rate-limiting transition, and there is even disagreement about the number of such transitions. In particular, optical trapping experiments indicate that a single transition (although it is not clear which transition this is) comprises most of the time of the kinesin step (100, 121), whereas dark-field (122) and interferometric scattering (120) measurements suggest that two transitions are of similar duration. A reason for these conflicting reports may be that the unbinding of heads strongly depends on the applied force (119, 123). On the other hand, the gold particles used for visualising kinesin's heads are large compared to them (120, 122). As a consequence, there is a need of less invasive methods of determining properties of the motor's step. For example, studies analysing the statistics of steps indicate at least two rate limiting steps (124), and the time for the diffusion of the tethered head, as it "overtakes" the head bound to the MT, may actually have been underestimated (125). At the time of writing this work, no consent has been reached on many questions regarding kinesin's mechanochemical cycle, and it does not seem that a complete understanding is nigh. It will be interesting to see how the different results will be reconciled in the future, and how they will contribute to a general understanding to kinesin's function.

At the end of this very short review about molecular motors, let us briefly mention the behaviour and function of some molecular motors of the kinesin family, which have become particularly important in the past years:

- Many kinesin motors are able to influence the dynamics of MT filaments. For example, kinesin-8 and kinesin-13 have been extensively studied recently, and they are able to depolymerise MTs at their plus end. More specifically, it has been shown that kinesin-8 depolymerises MTs in a length-dependent manner (20, 21); This motor also has impact on spindle size (126, 127). A density gradient of this motor on the MT, arising from the interplay of attachment to the MT and directed transport, enables MTs to "sense" their length (22, 23). Kinesin-13, such as MCAK, uses a different mechanism to track plus ends. More specifically, motors of this family diffuse along the lattice (128), and follow a diffusion and capture mechanism (129, 130), which is highly optimised to their physical properties. We will report on a project about the kinesin-8 motor Kip3 in Part II.

- Kinesin-1 motors influence each other's binding to the MT (30, 31). Furthermore, they show

functional heterogeneity, and can proceed along the MT with characteristically different speed (32). A project on the motion of kinesin-1 is presented in Part III. Various aspects of the motion of this motors have also been motivation for the master theses of Alessandro Bottero (33), and Moritz Striebel (131).

- More recently, also the interactions of many molecular motors with each other, or with other motors have come into focus (72, 87, 132, 133). These studies have inspired the master thesis of Maria Eckl (134).

- With the emergence of nanotechnology, leading to fascinating techniques such as DNA origami (135, 136), the construction of artificial molecular motors has become a flourishing field of study (12, 13, 137–143). A chapter of this thesis will be devoted to so-called molecular spiders, see Part I. Self assembly of DNA-coated structures furthermore motivated the master thesis of Timo Krüger (144).

2. Theoretical framework: The TASEP

In this Section we review the *Totally Asymmetric Simple Exclusion Process* (TASEP), which is the theoretical model underlying wide parts of this work. Chou and coworkers summarise the impact of TASEP as "a paradigmatic model for [non-equilibrium statistical mechanics], much like the role the Ising model played for equilibrium statistical mechanics" (145). Originally discussed in the context of ribosomes translating and moving along mRNA by Gibbs and coworkers (146), TASEP has quickly attracted attention in various different contexts from Brownian processes with hard-core interactions (147) to traffic flow (148), but its implications even range towards the evolution of surfaces and zero-range processes (149).

The TASEP with open boundaries is depicted in Fig. 5. It describes the driven motion of particles along a one-dimensional lattice. Particles enter the lattice at the left end with rate α if the first site is not occupied by another particle. They proceed towards the right of the lattice at rate v, provided the next site is empty. Having arrived at the right end, particles exit the lattice with rate β. By convention, α and β are measured in units of v, which amounts to define the basic time scale in terms of the hopping rate, $v \equiv 1$. The TASEP has attracted significant attention in the past years not only due to its role as the basic process for a wide range of applications, but also because it shows boundary-induced non-equilibrium phase transitions. In the following, we proceed along the lines of Krapivsky et al. (149) in order to derive the collective motion and the phase behaviour of this stochastic process.

The state of the lattice can be described in terms of occupation numbers. Here, $n_i = 1$ indicates that site i is occupied by a particle, whereas $n_i = 0$ implies its vacancy. n_i changes whenever a particle steps to, or leaves from site i. The former is possible if a motor is located at site $i-1$, and site i is empty. With the Kronecker δ, this can be written as $\delta_{n_{i-1},1}\delta_{n_i,0}$. Correspondingly, the leaving of a motor from site i comprises the term $\delta_{n_i,1}\delta_{n_{i+1},0}$. The probability that the occupation number n_i flips per time dt, is then given by the sum of these terms. In consequence, this implies

$$n_i(t + dt) = \begin{cases} 1 - n_i(t) & \text{with prob. } dt\left[\delta_{n_{i-1}(t),1}\delta_{n_i(t),0} + \delta_{n_i(t),1}\delta_{n_{i+1}(t),0}\right] \\ n_i(t) & \text{with prob. } 1 - \% \end{cases} \tag{1}$$

for any site i in the lattice bulk. Similar Equations can also be derived for the first lattice site ($i = 1$,
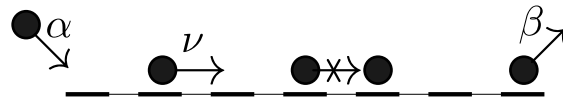
Figure 5.: The Totally Asymmetric Simple Exclusion Process (TASEP) with open boundaries. Particles enter the one-dimensional lattice at the left end at rate α. They step towards to right with rate v, obeying exclusion. From the lattice site on the right end, they may detach at β.

particle entrance with rate α) and the last lattice site of a lattice of length N ($i = N$, exit with rate β), see Ref. (149).

Equation (1) can be rewritten in terms of expectation values, and when $dt \to 0$, the time derivative of the average occupation number is obtained:

$$\partial_t \langle n_i \rangle = \begin{cases} \alpha \langle 1 - n_1 \rangle - \langle n_1(1 - n_2) \rangle, & i = 1 \text{ (left end)}, \\ \langle n_{i-1}(1 - n_i) \rangle - \langle n_i(1 - n_{i+1}) \rangle, & 1 < i < N \text{ (lattice bulk)}, \\ \langle n_{N-1}(1 - n_N) \rangle - \beta \langle n_N \rangle, & i = N \text{ (right end)}. \end{cases} \quad (2)$$

These Equations have been solved exactly by Derrida and coworkers (150) by using a matrix ansatz. While this method has been applied to several related models (151), an approximate way to find the steady state solutions is sufficient for the models and problems discussed in this work. More specifically, the mean-field approximation has been successfully applied on a variety of TASEP-related models. This approximation essentially amounts to disregard any correlations between the occupation of different lattice sites. Consequently, we approximate $\langle n_i n_j \rangle \approx \langle n_i \rangle \langle n_j \rangle$, and denote with ρ_i the probability that site i is occupied by a particle ("particle density"). Furthermore, we consider the limit of a long lattice, $1/N \to 0$, such that instead of discrete lattice sites we may consider a continuous spatial variable, $\{1, \dots, N\} \to [0, 1]$. This leads to

$$\partial_t \rho(x) \approx \partial_x \rho(x) [2\rho(x) - 1] \quad (3)$$

in the lattice bulk. It is important to note that Eq. (3) has the form of a continuity equation $\partial_t \rho = -\partial_x j$ with the motor current $j(x) = \rho(x)[1 - \rho(x)]$. This can be understood as a conservation of mass law in the lattice bulk: particles which have entered the lattice at the left end cannot leave it before they have arrived at the right end. In the stationary state, when $\partial_t \rho(x) = 0$, Eq. (3) directly implies that the density ρ must be constant along the lattice.

Along the same lines, the density at the left and right lattice end can be obtained. In the stationary state, this leads to

$$\rho(0) = \alpha, \qquad \rho(1) = 1 - \beta. \quad (4)$$

A subtlety of Eqs.(3)–(4) is that other than for $\alpha = \beta = 1/2$, there exists no solution which has constant density and meets the two boundary conditions. For parameters different from these values, the solution must therefore violate one of the boundary conditions, or have non-constant density somewhere. In general, this can be resolved by assuming that constant densities meeting the boundary conditions, $\rho_l = \alpha$ and $\rho_r = 1 - \beta$, extend into the lattice bulk and are connected by a (virtual) domain wall (DW). Assuming that the DW is located in the lattice bulk originally, the density profile in the stationary state can then be obtained by exploring the direction in which the DW is driven. To this end, a traveling wave ansatz $\rho = \rho(x - Vt)$ is inserted into the continuity equation, Eq. (3); it gives rise to the DW velocity $V = \beta - \alpha$ (152). If the DW starts inside the lattice bulk, it will be shifted towards the right lattice end provided $\alpha < \beta$, while for $\beta < \alpha$ it moves to the left. For the stationary state this implies that as long as the injection rate is small, the DW is located at the right lattice end, such that the density $\rho_l = \alpha$ extends over the whole lattice except for the immediate vicinity of the right end. Correspondingly, for small particle exit rate, the DW is located at the left end, and the bulk density ρ_b is given by $\rho_r = 1 - \beta$.
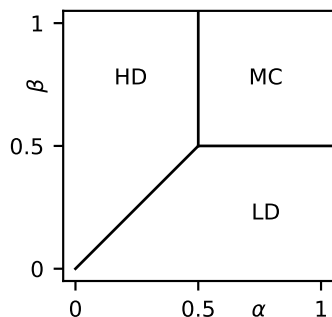
Figure 6.: The phase diagram of TASEP. Depending on the rates of particle injection into the lattice, α, and the exit rate β, we find three different phases: The low density (LD) phase, where the bulk density $\rho_b = \alpha$; the high density (HD) phase, where $\rho_b = 1 - \beta$; and the maximal current phase: here, $\rho_b = 1/2$.

However, it is clear from a heuristic point of view that the densities ρ_l and ρ_r cannot be maintained for arbitrarily high values of α and β. Consider, for example, a very high exit rate, implying that particles are quickly removed from the last site. Because the only way particles can "feel" each others' presence is via exclusion, indicating that particles can only be influenced by other particles in their direction of motion, removing particles from the last site cannot have arbitrarily high impact on the bulk dynamics. Assuming that the boundary rates have direct influence on the bulk dynamics for some α and β, the threshold value, at which these rates cease to determine ρ_b can be computed by considering the collective velocity V_{coll}. Essentially, this quantity signifies in which direction a density perturbation is driven. Let us for instance assume that α is slightly raised from its initial value: If the sign of the collective velocity is positive, the particle density will adapt to the new α; in the opposite case, the bulk density will show no reaction on an increased injection rate. With the motor current defined above, the collective velocity evaluates as $V_{\text{coll}} = \partial_\rho j(\rho) = 1 - 2\rho$. For the case of the left boundary, where $\rho_l = \alpha$, this implies that as α exceeds $1/2$, no more impact on the bulk density can be found. Similarly, for the density matching the exit density, $\rho_r = 1 - \beta$, an increase of β beyond $1/2$ does not change the bulk density. As a consequence, if both α and β exceed $1/2$, the bulk density is not determined from one of the boundaries but from the amount of particles which can be transported through the lattice.

With these considerations, we have explored the full dependence of the bulk dynamics on the boundary rates. It can be summarised in a phase diagram, see Fig. 6.

Three different phases are found:

- For $\alpha < \beta$ and $\alpha < 1/2$, the bulk density is determined via the injection rate at the left end; α is the *bottleneck* of these dynamics. Because the bulk density $\rho_b = \alpha$ is small in this case, this phase is termed the low density (LD) phase. The density rises to its boundary value $1 - \beta$ only in the immediate vicinity of the right lattice end ("boundary layer").

- For the opposite case, $\beta < \alpha$ and $\beta < 1/2$, the exit rate governs the bulk behaviour, $\rho_b = 1 - \beta$. Here, a boundary layer is found at the left lattice end. This phase is called high density (HD) phase.

- When both $\alpha > 1/2$ and $\beta > 1/2$, we have concluded from the sign of the collective velocity of the particles that none of the boundary rates directly determines the bulk behaviour. As a consequence, the density assumes the value $\rho_b = 1/2$, at which the particle current $j = \rho(1 - \rho)$ becomes maximal. Therefore, this phase is termed maximal current (MC) phase. Boundary layers can be found both at the left and the right end for this phase.

- For the special case $\alpha = \beta < 1/2$, the velocity of the DW vanishes, which can therefore be found anywhere on the lattice. Because the DW undergoes diffusive motion, the *average* particle density profile shows a straight line in this case, although the *momentary* density profile is flat before and after the DW.

A great number of models have used TASEP as their basis and have served applications in numerous physical and biological contexts. Several extensive reviews (145, 153) on this topic exist. The focus of this Section is therefore to briefly summarise results of TASEP-related models which are important for the motion of molecular motors and for the studies presented in this work.

TASEP with Langmuir kinetics (LK)   When the motion of molecular motors is considered, it is important to note that they can attach to any site on the MT. Likewise, motors may prematurely detach before having reached the plus end. However, in its original version, the TASEP allows for particle binding to and unbinding from the lattice only at the first and last site, respectively. A model including attachment and detachment of particles in the lattice bulk is the TASEP with Langmuir kinetics (TASEP/LK), which was first considered by Lipowsky et al. (154), and Parmeggiani et al. (155, 156). It combines an equilibrium process obeying detailed balance (attachment/detachment) with a non-equilibrium process violating detailed balance (directed motion). When the kinetics of these processes are comparable (mesoscopic limit), a motor density gradient forms on the lattice as a result of this interplay. Moreover, phase coexistence is found on the lattice. This implies that different parts of the lattice may show different collective dynamics. As a result, the domain wall (DW), separating the coexisting density domains, becomes localised.

TASEP on dynamic lattices   As a molecular motor moves along the MT, the length of this polymer can change because of the quick polymerisation and depolymerisation dynamics at the MT plus end. Therefore, the study of a TASEP on a lattice of dynamic length is a crucial problem. Originally motivated from filamentous fungal growth (157, 158), Sugden and Evans studied a model in which the lattice dynamically extends (159). A central implication of their study is that for certain conditions, a DW is found which moves away from the tip in a frame co-moving with the end. Nowak et al. (160) examined a lattice with a fluctuating wall marking the right end of the lattice. By invoking a moving-frame finite segment approach, they discovered different regimes in which the wall either acquires a steady-state position, or moves towards one of the ends. A very similar phenomenology was observed by Reese et al. (22) and Melbinger et al. (23): In these studies, the molecular motor kinesin-8 is considered which is known to depolymerise MTs. Similar to Ref. (160), different regulatory regimes exist, where the MT either approaches a stationary length, or shrinks or grows indefinitely.

TASEP with limited resources   Inside cells, the volume concentration of molecular motors is depleted as they attach to MTs. As a consequence, the attachment rate of motors is thought to decrease with the number of motors on the lattice. Several studies have thus considered variants of the TASEP with limited particle numbers. It was found (161, 162) that finite availability of particles can lead to phase coexistence and a localised DW, similar to the behaviour of TASEP/LK. Also multiple TASEP lattices with shared reservoirs have been examined. When all lattices have the same length (162), the collective dynamics are similar to the case of a single filament; as a mixed population of lattices is studied (163), non-trivial phase transitions can be observed. Furthermore, a TASEP with limited resources has been considered together with attachment and detachment kinetics (164). An interesting aspect was added by Brackley and coworkers (165) who discovered a rich phase diagram when both the number of particles as well as the availability of "fuel carriers", necessary for particle movement, were limited.

TASEP of extended particles   When molecular motors are considered, it is important to keep in mind that the majority of all processive motors are dimers which occupy two adjacent binding sites on the MT. Addressing this problem, Shaw et al. (166), and Lakatos and Chou (167) have considered a TASEP with extended objects. A theoretical challenge arising from this generalisation is that spatial correlations of particles due to their finite size have to be considered explicitly, which necessarily requires refined mean-field theories. For a more direct application to molecular motors, a TASEP of dimeric particles has recently been studied together with attachment and detachment kinetics (168). In the past years, several studies have furthermore examined laterally extended particles or particles with lateral interactions (131, 169, 170), as well as multi-lane systems (171–175). These extensions of TASEP have revealed qualitatively new phases of the collective dynamics (131).

TASEP with interacting particles   While the only possibility how particles can interact with each other in the TASEP is via hard-core exclusion, molecular motors are thought to show additional interactions. Already in the early days of TASEP, studies have looked at related, more complex models in this direction. One of the most prominent models was introduced by Katz, Lebowitz and Spohn (176, 177), who considered a two-dimensional lattice gas with particles in an electric field. More recently, TASEP extensions have been studied in which the hopping rate of particles depends on whether they are "pushed" by another particle (178). It was shown that the associated repulsive interaction can optimise the particle flux. Moreover, the dependence of particle attachment to and detachment from the lattice on the occupation of neighbouring lattice sites has been taken into account by considering so-called "mutually interactive Langmuir kinetics" (179, 180). As a consequence of these interactions, up to three domains with particles in different phases coexist on the lattice. More recently, also interactions between motors of two different species have come into focus (33, 181, 182). Highly interesting effects such as phase separation of the species can be observed (183), similar to observations in recent experiments (87).

Part I.

Teams of molecular spiders: a model for groups of molecular motors

3. Introduction

The desire to understand the biophysical principles which enable molecular motors to step processively along microtubules has created a whole new field of research: Recent advances in nanotechnology have led to construction of artificial molecular motors from scratch (11, 137, 184). An important approach in this direction comprise so-called DNA walkers which move or diffuse along a substrate (140–142). In this work, we examine properties of a specific DNA built motor termed molecular spider which was originally described by Pei and coworkers (12). Their name derives from the multivalent design which was employed: A spider comprises a body to which several legs of single-stranded DNA are attached. The legs have catalytic activity and can cleave the substrate to which they bind. Based on these principles, processive motion was observed; furthermore the spider as a whole remained firmly attached to the substrate for hours due to their multipedal architecture (12). More recently, prescriptive substrate landscape self-assembled with DNA origami (135) have been used to assign well-defined tasks to spiders which, for example, comprised control of their movement. Lund and coworkers even report "elementary robotic behaviour" of these spiders (13).

Molecular spiders have also had significant impact in theoretical studies: Antal et al. (9) and Antal and Krapivsky (8) proposed a simple model in which the catalytic cleaving reaction led to a binary discrimination between previously visited and unvisited sites; ultimately, this introduces a memory effect in the substrate (8). In particular for the case of a slow cleaving reaction, it was found that spiders are biased towards unvisited sites on a one-dimensional lattice (8). Several studies have built on these findings. For instance, variations of the rate constants involved in the chemical reactions (185, 186) have been examined, but also the number and length of legs (187). Furthermore, different stepping mechanisms have been studied (186). However, the amount of superdiffusion which spiders show in the long run (185) remained relatively small, showing that an important task is to improve their efficiency and processivity.

This was the starting point for our project. In the following, we examine dynamic and stochastic properties of a novel molecular spider design: n molecular spiders are constrained due to their joint attachment to a single linking node which may be considered as a primitive model of a cargo. The resulting spider-spider interactions lead to collective effects which enhance the motor properties of the n-spider team. We show that spider teams are faster and move more persistently along their track than individual spiders. We also predict that the spider teams move at reduced randomness and thus are candidates for applications that require reliable, i.e. predictable motion (139). In conclusion, molecular spiders provide a versatile system where cooperativity on the nanoscale can be studied in great detail.

The findings of our study have been published in *Physical Review E, 87, 3 (2013)* under the title "Cooperative effects enhance the transport properties of molecular spider teams". With kind permission from the American Physical Society, we will reprint this publication in the following and present our results in details there.

4. Publication

Cooperative effects enhance the transport properties of molecular spider teams

by

Matthias Rank[1], Louis Reese[2], and Erwin Frey[1]

[1] Arnold Sommerfeld Center for Theoretical Physics (ASC) and Center for NanoScience (CeNS), Department of Physics, Ludwig-Maximilians-Universität München, Theresienstraße 37, 80333 München, Germany

[2] Department of Bionanoscience, Kavli Institute of Nanoscience, Faculty of Applied Sciences, Delft University of Technology, Van der Maasweg 9, 2629 HZ Delft, The Netherlands

published in

Cooperative effects enhance the transport properties of molecular spider teams

Matthias Rank, Louis Reese, and Erwin Frey[*]

Arnold Sommerfeld Center for Theoretical Physics (ASC) and Center for NanoScience (CeNS) and Department of Physics,
Ludwig-Maximilians-Universität München, Theresienstraße 37, 80333 München, Germany
(Received 12 December 2012; published 8 March 2013)

Molecular spiders are synthetic molecular motors based on DNA nanotechnology. While natural molecular motors have evolved towards very high efficiency, it remains a major challenge to develop efficient designs for man-made molecular motors. Inspired by biological motor proteins such as kinesin and myosin, molecular spiders comprise a body and several legs. The legs walk on a lattice that is coated with substrate which can be cleaved catalytically. We propose a molecular spider design in which n spiders form a team. Our theoretical considerations show that coupling several spiders together alters the dynamics of the resulting team significantly. Although spiders operate at a scale where diffusion is dominant, spider teams can be tuned to behave nearly ballistic, which results in fast and predictable motion. Based on the separation of time scales of substrate and product dwell times, we develop a theory which utilizes equivalence classes to coarse-grain the microstate space. In addition, we calculate diffusion coefficients of the spider teams, employing a mapping of an n-spider team to an n-dimensional random walker on a confined lattice. We validate these results with Monte Carlo simulations and predict optimal parameters of the molecular spider team architecture which makes their motion most directed and maximally predictable.

I. INTRODUCTION

How the motion of molecules along predefined traffic routes emerges and how these molecules self-organize has become an experimentally tractable question due to advances in nanotechnology. Molecular motors that have evolved inside cells and perform well-defined tasks [1] inspired the engineering of DNA devices performing motor business on the nanoscale [2–4]: So-called DNA walkers have been built that move or diffuse along a substrate [5–7]. Among the first autonomous synthetic walkers was a motor design that used a catalytic reaction to cleave a substrate in order to move forward [8]. Since then, a plethora of different motor molecules have been built from scratch in the laboratory. They not only serve technological advances, but also shed light on the basic principles of molecular movement, e.g., of biological molecular motors. One class of molecules that attracted a great deal of attention is molecular spiders [9]. They combine the catalytic activity of nucleic acids with a multivalent design: Attached to a body are several legs of single-stranded DNA. These DNA legs can bind to and catalytically cleave a substrate. This can be repeated over and over again, which in turn generates processive motion: While individual legs dissociate from the substrate on a time scale of seconds, the multipedal architecture ensures tight binding of the spider to the substrate for hours [9]. Recent experiments used DNA origami to build quasi-one-dimensional tracks for molecular spiders [10]. A predescribed substrate landscape allows one to assign special tasks to a spider and, for instance, control its movement. The simple yet well-defined design makes it possible to study spiders in great detail and probe theoretical predictions.

Molecular spiders have also been theoretically studied extensively in recent years. Antal *et al*. [11] and Antal and Krapivsky [12] were the first to propose an abstract model that describes the dynamics of molecular spiders. They analyzed the spiders' kinetics for various architectures and found a variety of interesting effects which arise due to the mutual exclusion of spider legs on the lattice and the presence of the substrate. Substrates are cleaved slowly in comparison to hopping from already cleaved sites. This distinction leads to subtle memory effects that affect the spiders' dynamics and result in a bias towards the substrate [12]. When the spider is in an all-cleaved area, principles emerging from simple exclusion processes [13,14] allow a derivation of the spiders' diffusion constants [11,15].

In the meantime, mechanistically more detailed systems have been considered. These include the variation of the rate constants involved in the chemical reactions [16,17] and boundary conditions [17], as well as the number and length of legs [18]. Samii *et al*. [17] investigated the spiders' stepping gait and considered inchworm as well as hand-over-hand spiders. Semenov *et al*. [16] showed that spiders experience a rather extended time period of superdiffusion given that the cleavage rate r is small. More complex spiders in quasi-one [19] and in two dimensions [20] have also been studied. Moreover, there have been studies focusing on mathematical aspects such as recurrence, transience, and ergodicity [21,22], as well as random environments [23,24]. These investigations have examined molecular spiders independently from their chemical motivation as a general class of multivalent random walkers [19].

The rich variety and diversity of these recent studies show that molecular spiders are a versatile system to study artificial molecular motors both theoretically as well as experimentally. However, many challenges still remain in improving their efficiency and tailoring the spiders' design for possible biotechnological applications [7].

In this study, we examine dynamic and stochastic properties of a molecular spider team design: n molecular spiders are constrained due to their joint attachment to a single linking

---

[*]frey@lmu.de

node which may be considered as a primitive model of a cargo. The resulting spider-spider interactions lead to collective effects which enhance the motor properties of the n-spider team. We show that spider teams are faster and move more persistently along their track than individual spiders. We also predict that the spider teams move at reduced randomness and thus are candidates for applications that require reliable, i.e., predictable motion [4].

This paper is organized as follows: In Sec. II we provide a detailed picture of how molecular spiders function and give a comprehensive introduction to the existing theoretical models before we define an n-spider team. Subsequently, in Sec. III A we present our main results: spider teams have enhanced motor properties. To explain these numerical observations, we present a comprehensive analysis of the stochastic dynamics of a spider team. In particular, we perform a reduction of the state space of the spider teams and thereby calculate the mean number of consecutive directed steps a spider team performs while attached to the substrate boundary (Sec. III B). Moreover, we explore the validity of the resulting network representation of the spider team dynamics and also show how it breaks down (Sec. III C). In addition to this approach, we provide an exact mapping of the n-spider team to an n-dimensional confined random walk (Sec. III D). This enables us to quantify the diffusion coefficient which describes the motion of a spider team during diffusive periods (Sec. III E). Finally, in Sec. IV we bridge theoretical and experimental observables and predict the existence of optimal parameters which maximize the spider teams' predictability. Finally (Sec. V), we conclude and identify connections to related fields.

II. MODEL DEFINITION

Our model is based on the theoretical description of molecular spiders introduced by Antal *et al.* [11] and Antal and Krapivsky [12] that was motivated by experiments of Pei *et al.* [9]. They propose a spider design that consists of a central body and l legs that are attached to it. Each leg has a certain length and thus the overall spider can span a maximal distance s. In the experiment, a spider is exposed to a (one-dimensional) lattice, to which a substrate is attached. Since binding of leg and substrate happens through the Watson-Crick mechanism [25], only one leg may bind to a lattice site at a time. In the model, this corresponds to an exclusion process in that the movement of one spider leg is constrained by the spider's remaining legs. The lattice prevails in two states: with and without substrate. Legs which bind to lattice sites with substrate can remove it (chemically: they cleave it, only a shorter part remains bound to the lattice), which happens along with unbinding from that site at rate r. By contrast, spiders unbind from sites without substrate (i.e., from product sites) at rate 1. In the model, a substrate is *always* cleaved when a leg steps away from it, and rebinding of a leg to a new lattice site happens instantaneously. Two different rules to rebind to a new lattice site have to be distinguished: Spiders' legs either have a certain ordering, i.e., they cannot "overtake" each other; these spiders are termed *inchworm* spiders [11,12,16]. Alternatively, spider legs have no ordering, i.e., they can step over each other; those spiders have been called "quick spiders" [11] or "hand-over-hand"

spiders [17,18] in previous studies. Both types of spiders show quite different behavior [18] and have to be well distinguished. In this paper, we will concentrate on inchworm spiders.

In our model a leg which has just unbound from the lattice rebinds to the lattice instantaneously. Furthermore, we allow a spider's leg to rebind to any lattice site as long as the new leg configuration does not violate any of the restrictions imposed by the leg length or the ordering of the legs (in particular, this implies that rebinding to the lattice site from which the leg just unbound is possible [26]); this can be motivated from experiments where the typical time scales for binding to substrates exceed those for diffusion by orders of magnitude [17]. In addition, our choice obviates unphysical situations that might occur for spider teams due to the complete blockage of a leg.

Hollow circles (○) denote unoccupied lattice sites and filled circles (●) indicate that a leg is attached to that site. The presence of substrate is marked with a hat, i.e., ●̂ or ○̂. Throughout this paper, we consider bipedal spiders (i.e., $l = 2$) with a maximal leg span of $s = 2$. Spiders may thus only arise in either the spanned (● ○ ●) or the relaxed (● ●) configuration. For this case, the geometry of the cleaved sites, which is usually called *product sea*, is an interval on the one-dimensional lattice; it gives rise to memory effects which stem from irreversible substrate cleavage [11].

Samii *et al.* [18] suggested that the lattice could be prepared with substrates on the right, and products on the left-hand side from the very beginning, and called this initial condition *P-S lattice*. This asymmetry makes some calculations easier, and it provides a symmetry breaking direction already at the beginning of the dynamics. We are going to use this kind of lattice throughout the paper.

Taken together, the spiders which we examine in this study are bipedal ($l = 2$) inchworm spiders with a maximal span of $s = 2$, which walk on a one-dimensional P-S lattice. Every spider's leg may rebind to any accessible lattice site as long as the ordering is preserved, including the site from where it just unbound.

Based on this model for molecular spiders, we propose a minimal model for a team of molecular spiders. Several, say n, molecular spiders are linked to a (virtual) cargo with an inelastic leash (i.e., a string; sometimes this is also called cable [27]) of a well-defined length. Each of these spiders runs on its own one-dimensional track. This is similar to biological molecular motors like kinesin-1 [28,29] that walk along one-dimensional microtubule filaments [1]. We call these ensembles of spiders that jointly pull a cargo a spider team. For a cartoon of a team of two spiders, see Fig. 1(a).

Note that the role of the "cargo" is not primarily to put load on the spiders; actually we set the mass of the cargo equal to zero. In contrast, the cargo mediates the interaction among the n spiders comprising the team: Since the strings used for linking the spiders to the cargo are inelastic with some length a, any two of the spiders' bodies may mostly be $2a$ away from each other. From the bodies, the furthermost reachable lattice site is given by the spiders' legs' length, call it b, so that the *maximal* distance between the leftmost and the rightmost leg of all the spiders in the team is given by $2(a + b) =: d$. Mathematically, letting λ_i (ρ_i) denote the position of the ith
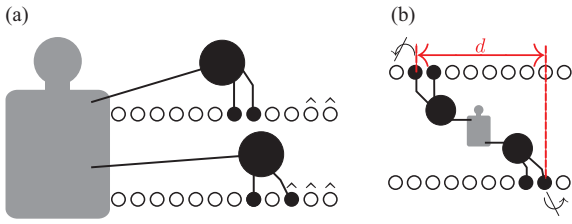
FIG. 1. (Color online) Cartoon of the spider team model and definition of the leash length d. (a) Two spiders are attached to a joint cargo with an inelastic string. Both spiders walk on their respective one-dimensional track. Hats indicate the presence of substrate. (b) The finite length of the linking string induces a maximal distance between the spiders' bodies which gives rise to a maximal span of the spider team, characterized by the "leash length" d.

spider's left (right) leg, this restriction reads

$$|\rho_i - \lambda_j| \leqslant d \;\; \forall i, j. \tag{1}$$

Note that this is a global constraint which restricts the spider *team*, in contrast to the local constraint limiting the span of an *individual* spider,

$$|\rho_i - \lambda_i| \leqslant s \equiv 2 \;\; \forall i. \tag{2}$$

The definition of d is visualized for a two-spider team in Fig. 1(b). For simplicity of language, and to capture an intuitive understanding especially for two-spider teams, we will call d the *leash length* in the following.

III. RESULTS

A. Enhanced properties of *n*-spider teams

We performed extensive numerical simulations to characterize the dynamic properties of n-spider teams. Our simulation data show that the constraint arising through the leash that holds the spider team together induces collective effects among the n spiders. We find that the incorporation of a spider into a team enhances many of the motor properties: The mean traveled distance of a spider team exceeds that of single spiders by far, up to orders of magnitude, for a rather small cleavage rate $r = 0.01$ [see Figs. 2(a) and 2(b)]. In addition, a spider team's movement is a lot more "predictable." This can be inferred from the width of the probability distributions, see Fig. 2(a), and the shaded areas depicted in Fig. 2(b), which illustrate the standard deviation of the mean displacement.

Another important quantity is the mean square displacement (MSD) of the spider teams [see Fig. 2(c)]. It shows a steep increase at intermediate time scales, similar but stronger and longer lasting compared to recent results by Semenov *et al.* [16] for single spiders: In this regime spiders move superdiffusively. To quantify the time-dependent effects of superdiffusion, we evaluated the "slope" of the variance in a double logarithmic scaling, i.e., the effective exponent

$$\alpha(t) = \frac{d \log\langle [x(t) - \langle x(t)\rangle]^2\rangle}{d \log t}, \tag{3}$$

which provides a measure for diffusivity (see also Refs. [16,19,30]). Figure 2(d) shows $\alpha(t)$ for a single spider and several different spider teams. Remarkably, the four-spider team travels almost ballistically ($\alpha \approx 2$) for rather

long times and the periods of "instantaneous superdiffusion" of spider teams (i.e., times with $\alpha > 1.1$ [16]) last much longer compared to single spiders. The nontrivial shape of $\alpha(t)$ indicates the multitude of dynamic processes that are involved in the spider team's dynamics: Initially, $\alpha \approx 1$ for $t \lesssim 1$ for all configurations, reflecting the very first hop of the spiders' left legs. In succession, until $t \lesssim r^{-1} = 100$, the spiders' right legs have typically not yet cleaved a substrate, whereas the left legs jump back and forth, hence the variance is approximately constant and thus $\alpha < 1$ (for these two regimes, see also a more explicit discussion in Ref. [16]). Had we chosen other starting conditions for the spiders, the behavior at short time would look different. Likewise, also the following regime until $t \lesssim 10^2 \dots 10^3$ results from the fixed starting conditions: While at early times the spider team does not feel the leash and all spiders can move independently from each other, at some point the leash is fully spanned and the spiders at the most extreme position (i.e., those contributing most to the variance) are retarded. This leads to a transient decrease of α. This regime is unique to spider teams since it is an effect constituted by the leash. Finally, for large times $t \gtrsim 10^2 \dots 10^3$, the memory of initial conditions is lost and α becomes maximal. Clearly, the maximal value of α is greatest for $n = 4$ of the displayed configuration. As time increases further, α decreases slowly which is due to the fact that more and more spiders move away from the product-substrate boundary (see also Ref. [16]). Figure 2(e) shows the velocity of the spider team by means of the derivative of the mean displacement with respect to time. Clearly, the velocity of a four-spider team outperforms that of a single spider by more than one order of magnitude.

These pronounced effects are in a way surprising: At first sight, one might speculate that the coupling leash which imposes an additional constraint on the spiders would handicap the spider team's motion and make it slower. This is clearly not the case. To the contrary, the dynamic properties of the spider teams are enhanced. In the remainder of this section we will explain this behavior using analytical arguments.

B. Boundary periods

a. Single spiders. Key to the understanding of an individual molecular spider's motion is to unravel the mechanism for biased motion. To this end we distinguish between two qualitatively different dynamic states of the spiders: Looking at single trajectories of molecular spiders we find that there are periods of time in which the spider's motion is strongly directed, and other periods with undirected, diffusive motion [see Fig. 2(f)]. In the following, we will call these dynamic states *boundary periods* and *diffusive periods*, respectively. To define the notion of these periods, it is convenient to distinguish between the steps of the spider's legs and the step of the spider as a whole. We define a *spider step* as a transition from a spread configuration ($\circ\bullet\circ\bullet\circ$) to another spread configuration shifted by one lattice unit forwards or backwards, i.e., $\circ\circ\bullet\circ\bullet$ or $\bullet\circ\bullet\circ\circ$, irrespective of the sites being products or substrates. During a diffusive period all the spider's legs are attached to product sites and therefore the spider steps with equal probability in both directions [11]. In contrast, biased spider motion can emerge in the vicinity of the boundary between product and substrate sites. We define a boundary
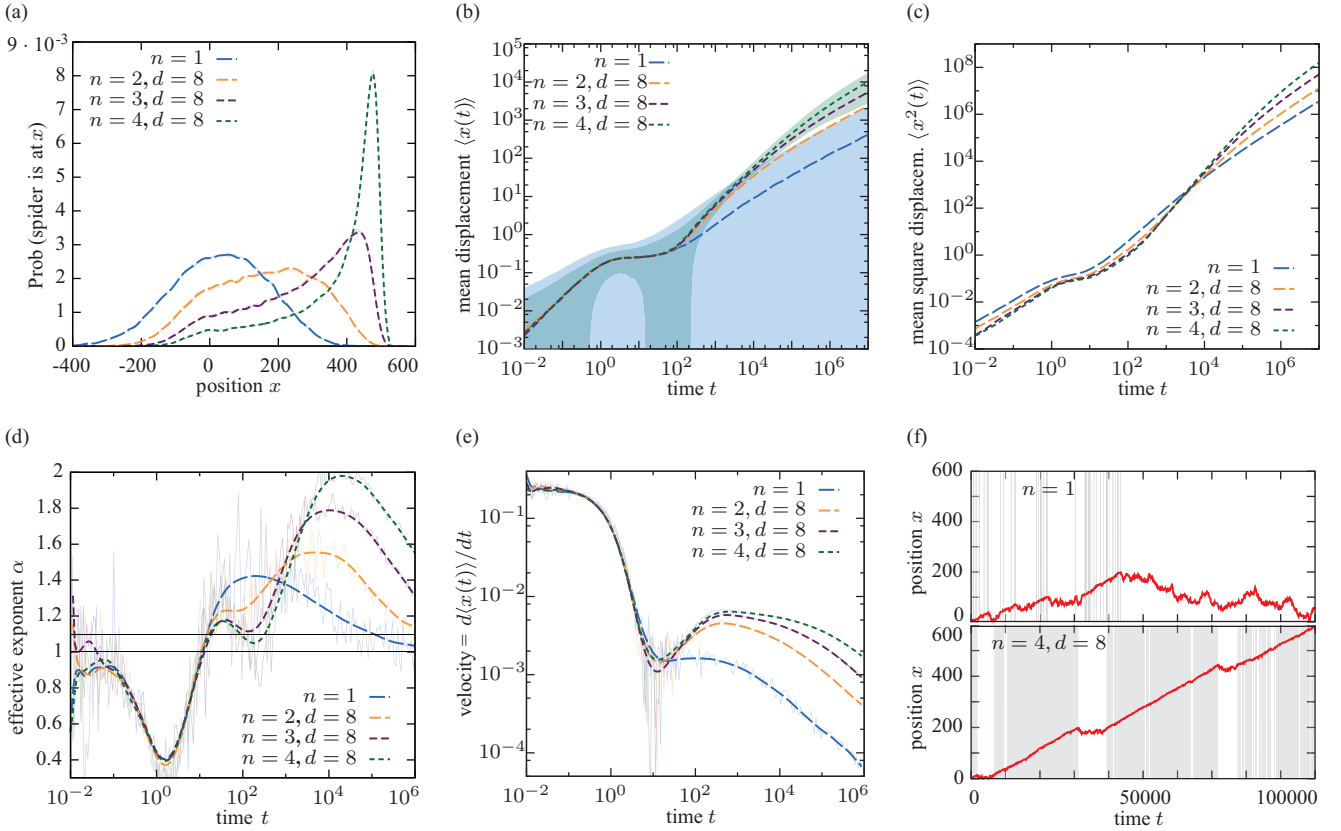
FIG. 2. (Color online) Dynamic properties of spider teams. Positions are given in lattice units throughout this work; time is defined by setting the hopping rate from products to 1. Thin shaded lines show data from finite difference approximations; thick lines show smoothing Bezier curves. (a) Probability distributions (histograms) of spiders to be at position x at time $t = 10^6$; simulation data were binned with a box size 1. Depicted are distributions for a single spider ($n = 1$) and spider teams comprised of $n = 2,3,4$ spiders and leash length $d = 8$, and cleavage rate $r = 0.01$. While the single spider distribution follows nearly a Gaussian centered close to the origin, the distributions of spider teams are clearly skewed and shifted towards larger x. The asymmetry stems from the P-S preparation of the lattice at $t = 0$ (products at the left, substrates at the right) [17]. (b) Mean displacement as a function of time (lines). The shaded areas represent the standard deviation around the mean displacement for a single spider and the four-spider team, respectively, and provide a measure for the randomness of the spiders' motion. Note that the *visual* impression of the standard deviation is rather that of a relative deviation, since the plot is in double logarithmic scale. (c) MSD as a function of time, $\langle x^2(t) \rangle$. (d) The variance's effective exponent $\alpha(t)$ [see Eq. (3)]. For diffusion, $\langle [x(t) - \langle x(t) \rangle]^2 \rangle \propto t^1$, hence $\alpha = 1$; superdiffusion corresponds to $\alpha > 1.1$ [16], and ballistic motion to $\alpha = 2$. The superdiffusive regime of spider teams lasts longer than that of single spiders; large spider teams reach nearly ballistic motion for significantly long times. For a more detailed discussion, see the main text. (e) Mean velocity of the spiders as a function of time. The mean velocity is defined as the time derivative of the mean displacement, $d\langle x(t) \rangle/dt$. Spider teams outperform single spiders by an order of magnitude. (f) Sample trajectory of a single spider (top), and a four-spider team with $d = 8$ (bottom). Periods in which the spider (team) is in the vicinity of the product-substrate boundary are shaded.

period as follows: It starts with a spread configuration where the right spider leg is attached to a substrate ($\cdots \circ \bullet \circ \hat{\bullet} \hat{\circ} \cdots$), and ends when the spider has fully stepped away from the substrate boundary ($\cdots \bullet \circ \bullet \circ \hat{\circ} \cdots$) (the dots indicate that the block of displayed lattice sites may have been shifted during the boundary period), as illustrated in Fig. 3(a). As a consequence, during a boundary period the substrate boundary is shifted by an integer number of lattice units forward.

For single spiders the bias can be measured by calculating the *first passage probability*, p_+, for the spider to progress one step forward during a boundary period, i.e., $p_+ =$ Prob$\{\bullet \circ \bullet \circ \hat{\circ} \nleftarrow \circ \bullet \circ \hat{\bullet} \hat{\circ} \to \circ \circ \bullet \circ \hat{\bullet}\}$ [see also Fig. 3(a) for an illustration of the corresponding dynamic processes]. By analyzing all possible sequences of transitions, Antal and Krapivsky found an explicit expression for the bias, namely, $p_+(r) = \frac{5+r}{8+4r}$ [12], valid for spiders with legs always jumping

to *neighboring* sites. Similar calculations can be performed for spiders whose legs may also rebind to the *same* site again (like those we consider throughout this paper), leading to $\tilde{p}_+(r) = \frac{5+3r}{8+8r}$. The mathematical expressions for p_+ and $\tilde{p}_+$ differ only slightly; in particular, they are equal in the limits $\lim_{r\to 0} \tilde{p}_+(r) = \lim_{r\to 0} p_+(r) = \frac{5}{8}$ and $\tilde{p}_+(r = 1) = p_+(r = 1) = \frac{1}{2}$ [31].

There is a special feature of single spiders which makes the definition of p_+ straightforward in this case: The spread configuration $\bullet \circ \bullet$ of the spider's legs is unique, since a spider step to the right corresponds to a translation of both legs to the right, and hence the configuration before and after a step is the same [cf. Fig. 3(a) states (i), (iii), and (vii)]. As we will show below, this is a property which unfortunately does not extend to spider teams.
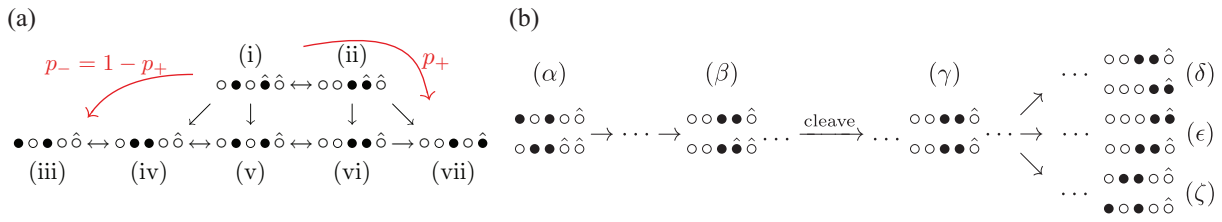
FIG. 3. (Color online) Definition of a boundary period. (a) Path of a single spider through a boundary period. The period *always* starts in state (i). From there, the spider can change to (ii), and back. When the right leg cleaves the substrate, the spider arrives at (iv), (v), (vi), or (vii). Arriving at (vii) corresponds to continuing the same boundary period from a new substrate [with "(vii) being the new (i)"], since (vii) and (i) are equivalent up to translation. Hence, the number of steps is raised by one upon arriving at (vii). If, by contrast, the spider reaches (iii), the boundary period ends and a diffusive period begins. The probability to make a successful step, i.e., to reach (vii) before (iii), is the bias p_+ calculated by Antal and Krapivsky [12]. The number of steps during a boundary period is then the number of transitions (i) → (vii), without reaching (iii) in between. This is equivalent to the number of cleavages during a boundary period, not counting the very last cleavage (which is not counted since by definition the spider steps away from the boundary after the last cleavage, and we only count forward steps). (b) Example of a boundary period of a two-spider team. (α) None of the spiders is in a boundary period, hence none of them experiences a bias. Thus, the spider *team* is in a diffusive period. When the lower spider reaches a substrate (β) it enters a boundary period. Thus, also the spider *team* enters a boundary period. In succession, the lower spider's right leg happens to cleave the substrate (γ). The lower spider can then find its way to a new substrate (δ) what constitutes a $\frac{1}{2}$ successful step for the spider team and preserves the boundary period. If the upper spider, in this case, steps to a substrate (ϵ), this does not yet, however, constitute a step. This is because although the spider team is in a boundary period, the *upper* spider has not been in a boundary period itself during this team's boundary period. Since a step essentially reflects a cleavage, no step can be integrated in this case. If the lower spider steps away from the new substrate (ζ), the spider team enters a diffusive period. In analogy to single spiders, the number of steps during a spider team's boundary period is equivalent to the number of cleavages during that period, divided by the number of spiders, and not counting each spider's *last* cleavage event.

A quantity which does not require this uniqueness is the mean number of consecutive directed steps that a spider performs during one boundary period. This quantity will be denoted $\langle S \rangle$ in the following. With

$$p_j = (p_+)^j (1 - p_+) \qquad (4)$$

being the probability that the spider walks precisely j steps during a boundary period, before it leaves the boundary and enters a diffusive period, $\langle S \rangle$ can be calculated as

$$\langle S(p_+) \rangle = \sum_{j=0}^{\infty} j p_j = \frac{p_+}{1 - p_+} \qquad (5)$$

for single spiders. Let us emphasize that $\langle S \rangle$ is different from the mean "number of steps the spider makes in the B state" [16], $\langle S_B \rangle$, as defined by Semenov *et al.*, which counts the number of leg movements ("leg steps" in our terminology). By contrast, $\langle S \rangle$ only counts a step if *both* legs have been shifted to the right without having moved to the left ("spider steps"), i.e., the number of times the spider consecutively reaches (vii) before (iii), starting from (i) in Fig. 3(a).

The number of consecutive spider steps, $\langle S \rangle$, is equivalent to the number of cleavage events during a boundary period. Not counted is the last cleavage before the spider leaves the boundary period, since this corresponds to a backward step of the spider [cf. Eq. (4)].

b. Spider teams. Clearly, the motion of a single spider is biased only during boundary periods, and undirected during diffusive periods. However, it is manifest that a spider *team*'s motion is not completely diffusive as long as *any of the spiders comprising the team* is in a boundary period. Hence, we consider the spider *team* being in a boundary period if at least one of its spiders resides in a boundary period. In order to compare the performance of individual spiders with that of

spider teams, it is now essential to find a way how to count the number of a spider team's steps during a boundary period. Basically, a team moves forward by one step if the boundary between substrate and product sites is shifted forward by one lattice unit on average. To this end we count every cleavage event but for each spider's last cleavage before the *team* leaves the boundary period. In analogy to a single spider, the latter avoids counting those events where the spider team moves away from the boundary and thereby steps backward [cf. Fig. 3(b)]. The number of steps of a spider team is then given by the number of such cleavage events divided by the number of spiders in a team, in accord with fractional steps of molecular motors like kinesin [32]. For example,

$$\begin{matrix} \circ \bullet \circ \hat{\bullet} \hat{\circ} \\ \circ \bullet \hat{\bullet} \hat{\circ} \hat{\circ} \end{matrix} \rightarrow \begin{matrix} \circ \circ \bullet \hat{\bullet} \hat{\circ} \\ \circ \circ \bullet \circ \hat{\bullet} \end{matrix} \qquad (6)$$

corresponds to two steps of the lower spider and thus one step for the spider team.

As we consider two or more coupled spiders, the translational symmetry of the state before and after a complete step ($\bullet \circ \hat{\bullet} \hat{\circ}$ and $\circ \bullet \circ \hat{\bullet}$, respectively, for a single spider) is broken, likewise the uniqueness of the state which is the first during a boundary period ($\bullet \circ \hat{\bullet}$ for a single spider), is lost. For example,

$$\begin{matrix} \bullet \circ \hat{\bullet} \hat{\circ} \hat{\circ} \\ \circ \bullet \bullet \circ \hat{\circ} \end{matrix}, \quad \begin{matrix} \circ \bullet \circ \hat{\bullet} \hat{\circ} \\ \circ \bullet \bullet \hat{\circ} \hat{\circ} \end{matrix}, \quad \begin{matrix} \circ \bullet \circ \hat{\bullet} \hat{\circ} \\ \circ \bullet \circ \bullet \hat{\circ} \end{matrix} \qquad (7)$$

all are possible states at the beginning of a boundary period. It is therefore no longer possible to calculate the probability to step to the right (denoted p_+ for single spiders) without further specification of these initial states. For spider teams the probability for a forward step explicitly depends on the particular state from which it starts.

This complexity prohibits an analytic treatment of the stochastic dynamics in general. However, if the relative rate of substrate cleavage is small compared to the rate of hopping from product sites, i.e., $r \ll 1$, the dynamics become amenable to a theoretical analysis. While in this limit the motion of the boundary between substrate and product sites is slow, the dynamics of spider legs bound to product sites are fast. This suggests to group states into classes characterized by the slow variable, i.e., the distance between the ends of the product seas, denoted by Δ. In addition, it turns out to be convenient to introduce subclasses according to the number of spiders attached to substrates, σ. In the following we will illustrate this for teams comprised of $n = 2$ spiders and a leash length $d = 2$. All states

$$\begin{smallmatrix} \circ\,\bullet\,\circ\,\hat\bullet\,\hat\circ \\ \circ\,\bullet\,\circ\,\hat\bullet\,\hat\circ \end{smallmatrix} \sim \begin{smallmatrix} \circ\,\circ\,\bullet\,\hat\bullet\,\hat\circ \\ \circ\,\bullet\,\circ\,\hat\bullet\,\hat\circ \end{smallmatrix} \sim \begin{smallmatrix} \circ\,\bullet\,\circ\,\hat\bullet\,\hat\circ \\ \circ\,\circ\,\bullet\,\hat\bullet\,\hat\circ \end{smallmatrix} \sim \begin{smallmatrix} \circ\,\circ\,\bullet\,\hat\bullet\,\hat\circ \\ \circ\,\circ\,\bullet\,\hat\bullet\,\hat\circ \end{smallmatrix} \tag{8}$$

comprise the class

$$\begin{bmatrix} \circ\,\bullet\,\circ\,\hat\bullet\,\hat\circ \\ \circ\,\bullet\,\circ\,\hat\bullet\,\hat\circ \end{bmatrix} =: [0_2] = [\Delta_\sigma]. \tag{9}$$

Likewise, configurations with $\Delta = 0$ and $\sigma = 1$, i.e., with only one spider having a leg at the boundary, are possible:

$$\begin{bmatrix} \circ\,\bullet\,\circ\,\hat\bullet\,\hat\circ \\ \circ\,\bullet\,\bullet\,\hat\circ\,\hat\circ \end{bmatrix} =: [0_1]. \tag{10}$$

Here, we made use of the invariance under renumbering of spiders, it is irrelevant if we label the "upper" spider as 1 and the "lower" as 2, or the other way round. Hence, irrespective of whether the lower or the upper spider's leg is bound to a substrate, both contribute to class $[0_1]$. That same renumbering symmetry can also be applied when one considers states where the lower and the upper product seas do not end at the same position. This leads to the classes

$$\begin{bmatrix} \circ\,\bullet\,\circ\,\hat\bullet\,\hat\circ \\ \circ\,\bullet\,\hat\bullet\,\hat\circ\,\hat\circ \end{bmatrix} =: [1_2] \quad \text{and} \quad \begin{bmatrix} \circ\,\bullet\,\bullet\,\hat\circ\,\hat\circ \\ \circ\,\bullet\,\bullet\,\hat\circ\,\hat\circ \end{bmatrix} =: [1_1], \tag{11}$$

as well as

$$\begin{bmatrix} \circ\,\circ\,\bullet\,\bullet\,\hat\circ \\ \circ\,\bullet\,\hat\bullet\,\hat\circ\,\hat\circ \end{bmatrix} =: [2_1]. \tag{12}$$

This completes the list of possible classes with $\sigma \neq 0$ since the constraint $d = 2$ imposed by the leash forbids class $[2_2]$, as well as classes $[\Delta_\sigma]$ with $\Delta > 2$. For general d, class $[d_2]$ and classes with $\Delta > d$ are not allowed.

One can show that the classification of states by means of the distance of the product seas' ends and the number of spiders at the boundary is reflexive, symmetric, and transitive, and hence defines an equivalence relation. Therefore, we tentatively used the symbols $\sim$ and $[\cdot]$ in the previous equations.

Instead of a large number of "micro" states, we are now left with only five equivalence classes which include all the spider states at the boundary. The reduction of complexity can be pushed even further: classes $[\Delta_1]$ with only one leg attached to the substrate are only transient in the sense that they will always decay into classes with two legs attached $[\Delta_2]$ (as long as $\Delta < d$). Consider, for example, a spider team in class $[0_1]$ where one spider's right leg is attached to a substrate while the other spider's legs are free to move on product sites. Since the diffusion time of legs on products is small compared

to the expected residence time $1/r$ of the leg on the substrate, the transition $[0_1] \rightarrow [0_2]$ is almost certain and happens on a time scale ~ 1 (fast compared to substrate cleavage).

All possible transitions between the classes can be visualized as the following reaction scheme:

$$\begin{array}{ccccc} & & [(d-1)_0] & \Rightarrow & \textbf{diffusive} \\ & & & & \textbf{period} \\ & & \Downarrow & \nwarrow & \\ [0_1] \quad [1_1] & & [(d-1)_1] & \leftarrow & [\boldsymbol{d_1}] \\ \Downarrow \quad \bowtie \quad \Downarrow \quad \bowtie \cdots \bowtie & & \Downarrow & \nearrow & \\ [\mathbf{0_2}] \rightleftarrows [\mathbf{1_2}] \rightleftarrows \cdots \rightleftarrows & [\mathbf{(d-1)_2}] & & & \end{array} \tag{13}$$
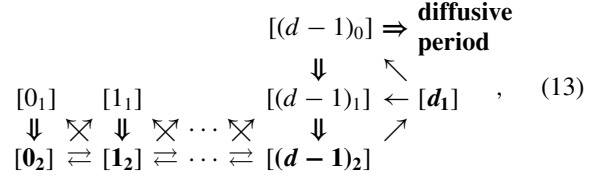
where Δ is constant along a column and σ along a row, respectively. As explained above, vertical transitions from $[\Delta_1]$ to $[\Delta_2]$ are fast [emphasized with double arrows in Eq. (13)]. In contrast, horizontal and diagonal transitions involving substrate cleaving events and hence leading to $\Delta \rightarrow \Delta \pm 1$ are slow. Since vertical transitions occur with certainty and fast, we can eliminate the transient classes $[\Delta_1]$ and reduce to a reaction scheme for the most stable subclass of each class, shown in boldface in Eq. (13) and signified $[\Delta]$ in the following:

$$[0] \underset{\frac{1}{2}}{\overset{1}{\rightleftharpoons}} [1] \underset{\frac{1}{2}}{\overset{\frac{1}{2}}{\rightleftharpoons}} \cdots \underset{\frac{1}{2}}{\overset{\frac{1}{2}}{\rightleftharpoons}} [d-1] \underset{\Pi}{\overset{\frac{1}{2}}{\rightleftharpoons}} [d] \overset{1-\Pi}{\longrightarrow} \begin{matrix} \text{diffusive} \\ \text{period} \end{matrix}. \tag{14}$$

The numbers above and below the arrows are transition probabilities into the respective classes, reflecting that each of the two spiders may cleave a substrate with equal probability for $\Delta < d$. The class $[d]$ has to be treated separately as it constitutes a gate from the boundary into the diffusive period.

Our next set of tasks is now threefold: First, in order for our classification scheme to be a consistent reduction of the stochastic processes, all states comprising the gate class $[d] = [d_1]$ should have the same *survival probability* Π, i.e., the same probability not to exit into a diffusive period. This is indeed the case for sufficiently small cleavage rates r: In the limit $r \rightarrow 0$, substrate cleavage events are rare compared to hopping from product sites. Therefore, the dynamics exhibit a time scale separation where all the legs attached to products quickly visit any accessible lattice site while the legs on substrate sites remain stuck. In other words, the dynamics within class $[d_1]$ are ergodic and equilibrate, and all micro states effectively reduce to one coarse-grained "macro" state, namely, the class $[d_1]$. Second, we have to calculate the survival probability Π by analyzing all the various routes between the micro states. Third, in order to determine the mean number of consecutive steps $\langle S \rangle$, the reduced reaction scheme of Eq. (14) has to be solved.

We now address the calculation of the survival probability Π. In principle, this can be done for arbitrary complex spider teams. For the purpose of illustration, we continue the example from above with two spiders and a leash length $d = 2$. We consider all states comprising class $[2_1]$. These are

$$① = \begin{smallmatrix} \circ\,\circ\,\bullet\,\bullet\,\hat\circ \\ \circ\,\bullet\,\hat\bullet\,\hat\circ\,\hat\circ \end{smallmatrix}, \quad ② = \begin{smallmatrix} \circ\,\bullet\,\circ\,\bullet\,\hat\circ \\ \circ\,\bullet\,\hat\bullet\,\hat\circ\,\hat\circ \end{smallmatrix}, \quad ③ = \begin{smallmatrix} \circ\,\bullet\,\bullet\,\circ\,\hat\circ \\ \circ\,\bullet\,\hat\bullet\,\hat\circ\,\hat\circ \end{smallmatrix},$$

$$④ = \begin{smallmatrix} \bullet\,\circ\,\circ\,\bullet\,\hat\circ \\ \circ\,\bullet\,\hat\bullet\,\hat\circ\,\hat\circ \end{smallmatrix}, \quad ⑤ = \begin{smallmatrix} \bullet\,\bullet\,\circ\,\circ\,\hat\circ \\ \circ\,\bullet\,\hat\bullet\,\hat\circ\,\hat\circ \end{smallmatrix}, \quad ⑥ = \begin{smallmatrix} \circ\,\bullet\,\bullet\,\circ\,\hat\circ \\ \bullet\,\circ\,\hat\bullet\,\hat\circ\,\hat\circ \end{smallmatrix}, \tag{15}$$

$$⑦ = \begin{smallmatrix} \bullet\,\circ\,\bullet\,\circ\,\hat\circ \\ \bullet\,\circ\,\hat\bullet\,\hat\circ\,\hat\circ \end{smallmatrix}, \quad ⑧ = \begin{smallmatrix} \bullet\,\bullet\,\circ\,\circ\,\hat\circ \\ \bullet\,\circ\,\hat\bullet\,\hat\circ\,\hat\circ \end{smallmatrix},$$

FIG. 4. (Color online) Justification for the equivalence classes in the limit $r \to 0$. Shown are the analytically calculated probabilities that a spider team ($n = d = 2$) successfully completes one step during a boundary period, starting from the specific states ①–⑧ as given in Eq. (15). Each line corresponds to a state of the equivalence class $[2_1]$ [cf. Eq. (12)]. In the limit $r \to 0$, the probability to step forward for all eight states collapses to a fixed value $\Pi \approx 0.65$.

and their respective "mirrored" states, i.e., the states with spiders 1 and 2 interchanged. Let us illustrate the calculation for the particular initial state ① . Legs unbind from products at rate 1 and from substrates with rate r. Hence, from this configuration, the probability that the upper right, or the lower right leg is the first one to unbind is $1/(3 + r)$ and $r/(3 + r)$, respectively. The left legs unbind first with probability $1/(3 + r)$ each. If now, for instance, the lower right leg detaches, it may either reattach to the very same lattice site again, or it may step one site to the right. In either case it cleaves a substrate. Both processes happen with equal probability. Hence, altogether, the transition probability for the lower right leg to step to the right is given by $r/2(3 + r)$. The analysis can be continued from the resulting states until either a step is completed or the team has left the boundary period, finally leading to a high dimensional system of linear equations. The results obtained by solving the ensuing sets of equations are shown in Fig. 4 for all initial states comprising class $[d_1]$.

Clearly, as r approaches 0, all survival probabilities, i.e., all probabilities to make a step within the team's boundary period, approach a single value

$$\Pi = \tfrac{115}{176} \approx 0.65. \qquad (16)$$

This result is reassuring, as it confirms our heuristic arguments on the equilibration of states within class $[d_1]$, and thereby justifies combining several different states into one class in the limit $r \to 0$.

All the complexity of calculating the mean number of steps $\langle S \rangle$ of a spider team during a boundary period has now been reduced to analyzing the various routes between the *equivalence classes*. Since each transition [33] in Eq. (14) corresponds to a directed step done during a boundary period, the number of these steps $\langle S \rangle$ is equivalent to the number of (undirected) jumps performed by a simple random walker with reflective and absorbing boundary conditions on the left, and right ends of the reaction scheme, respectively. As detailed in the Appendix, the general solution for the mean number of

TABLE I. Comparison of analytic and simulation results for the mean number of steps during a boundary period, $\langle S \rangle$. Analytic values were derived in the limit $r \to 0$; simulation results were obtained for very small $r \lesssim 10^{-4}$. Simulations and analytical calculations show excellent agreement.

	$\langle S(r \to 0)_d^n \rangle$, analytic	$\langle S(r \lesssim 10^{-4})_d^n \rangle$, simulation
$n = 1$	$\tfrac{5}{3} \approx 1.6667$	1.6672 ± 0.0015
$n = 2, d = 2$	$\tfrac{291}{61} \approx 4.770$	4.769 ± 0.003
$n = 2, d = 3$	$\tfrac{3\,170\,931}{443\,341} \approx 7.152$	7.146 ± 0.005
$n = 2, d = 4$	$\tfrac{4\,055\,316\,673}{414\,459\,263} \approx 9.785$	9.785 ± 0.008
$n = 3, d = 2$	$\tfrac{340\,881}{48\,391} \approx 7.044$	7.042 ± 0.006
$n = 3, d = 3$	$\tfrac{16.3745\ldots}{1.34258\ldots} \approx 12.196$	12.204 ± 0.012

steps during a boundary period in the limit $r \to 0$, and for arbitrary d, reads

$$\langle S(d, r \to 0) \rangle = \frac{\Pi}{1 - \Pi} + (d - 1)\frac{1}{1 - \Pi}. \qquad (17)$$

For our example of a two-spider team with $d = 2$, we obtain, using Eq. (16),

$$\left\langle S(r \to 0)_{d=2}^{n=2} \right\rangle = \tfrac{291}{61} \approx 4.77. \qquad (18)$$

We also analyzed more complex spider teams with size $n = 2, 3$ and up to a leash length of $d = 4$, and found even larger mean step numbers, compared to $\tfrac{5}{3}$ for a single spider. Obviously, during boundary periods even the simplest spider teams behave significantly more directed and progress a lot further on average, compared to individual spiders. This result is remarkable since directed motion is desirable for applications and a rare feature at the nanoscale. The analytical results are summarized in Table I where they are also compared with Monte Carlo simulations which match them at a very high accuracy.

C. Validity of the equivalence classes

With increasing d, the spiders forming a team become more and more independent since it is increasingly unlikely that a spider "feels" the constraint of its teammates. In particular, the probability Π that a spider in class $[d_1]$ reaches $[(d - 1)_2]$ without exiting the boundary period [cf. Eq. (14)], converges towards the probability p_+ that a single spider makes a step to the right which is $\tfrac{5}{8}$ for $r \to 0$. Hence, assuming $\Pi = \tfrac{5}{8}$ for large d, Eq. (17) would imply that the mean number of steps increases linearly with d. Indeed, in the asymptotic limit $r \to 0$ this agrees well with the simulation data. However, with increasing r deviations from this linear behavior become more and more significant (cf. Fig. 5).

This can be explained as follows: For increasing leash length d, the configuration space accessible to the spider team becomes progressively larger, so that it takes longer to completely exploit it, i.e., the *equilibration time* grows. Conversely, the average time of substrate cleavage scales as $1/r$. With increasing r and/or d these two time scales become comparable. The assumption of time scale separation, on which the reduction of the dynamics to equivalence classes was based, then becomes invalid. In conclusion, the equivalence class concept which we derived in the previous sections provides a very good approximation for small but finite
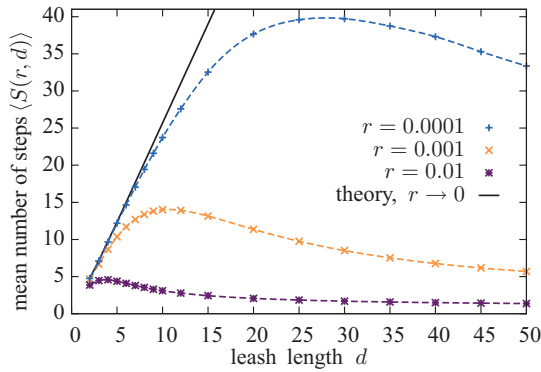
FIG. 5. (Color online) Validity of the equivalence class formalism. Shown are the simulation results for the mean number of steps $\langle S \rangle$ for a two-spider team and different values of d and cleavage rates $r = 0.0001, 0.001, 0.01$; broken lines are a guide to the eye. The theoretical result derived within the equivalence class formalism for $r \to 0$ (black) is exact for $d = 2, 3, 4$ (Table I), and we assumed $\Pi = \frac{5}{8}$ for $d \geqslant 5$ [Eq. (17)].

substrate cleavage rates r, as long as the leash length d is not too large.

D. An exact mapping to a confined random walker

For a bipedal spider with a maximal span of $s = 2$, a single coordinate, the "center of mass" coordinate, fully describes the position of the spider's legs. Hence, it is possible to map the motion of the single spider's legs on $\frac{1}{2}\mathbb{Z}$, the set of integers and half-integers, with hopping of the legs corresponding to changes of the center of mass [11,12]. This mapping can be
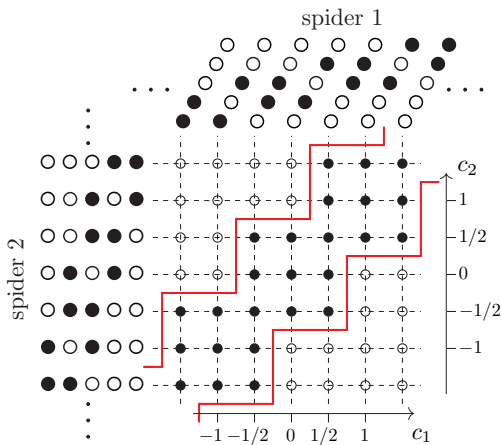
FIG. 6. (Color online) A spider team can be mapped to a random walk in a confined environment: Transitions of a spider's leg correspond to a change of its center-of-mass coordinate c_i of $\pm\frac{1}{2}$. Shown is the mapping of a two-spider team with a leash length $d = 2$. The shape of the environment (solid) follows from the leash constraint which confines the span of the spider team. From $d = 2$ follows that the leftmost left and the rightmost right legs of the two spiders may be at most two lattice sites apart. With that restriction, the allowed configurations of the team follow directly, as can be seen with some explicit configurations in the left and the top part of the figure.

extended for a spider team: The position of an n-spider team is characterized by a position on an n-dimensional square lattice where each of the n axes corresponds to the center of mass of one of the spiders comprising the team. The dynamics of a spider team then corresponds to a trajectory on that lattice. However, due to the leash constraint, not all sites on this lattice are accessible to the spider team. To illustrate this, let us for the moment focus on a two-spider team with leash length $d = 2$. Fixing the first spider's center of mass c_1, the other spider's center of mass c_2 is restricted to be near c_1 due to the leash constraint. We have to distinguish between two cases. Spider 1 is either in a spread or a relaxed configuration, e.g., $c_1 = 0$ or $c_1 = \frac{1}{2}$, respectively. If it is in the spread configuration $c_1 = 0$, then the other spider may be in one of three configurations: $c_2 \in \{-\frac{1}{2}, 0, \frac{1}{2}\}$. For the relaxed configuration $c_1 = \frac{1}{2}$, there are five configurations possible for the second spider: $-\frac{1}{2}$, 0, $\frac{1}{2}$, 1, and $\frac{3}{2}$. Geometrically, this leads to a *staircase* shape for the accessible set of states. For arbitrary d, the step width of this staircase generalizes to $4d - 3$ and $4d - 5$ (cf. Fig. 6).

While in Sec. III E this mapping will be employed to calculate diffusion constants during diffusive periods, we use it here to illustrate the concept of equivalence classes again. To this end, the mapping is generalized to incorporate substrates as illustrated in shaded colors in Fig. 7: Each substrate can be drawn as a box. This is seen as follows: Because each spider being at a specific substrate site may either be in a spread or
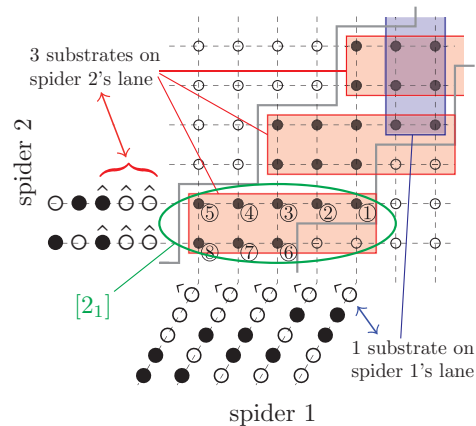
FIG. 7. (Color online) Substrate in the staircase random walker picture ($n = d = 2$ as before). Like in Fig. 6, explicit configurations are shown for some points. In addition, boxes are drawn which correspond to the substrates on spider 1's (vertical blue box), or spider 2's (horizontal red boxes) lane. This can be understood as follows: When a spider is attached to a substrate with its right leg, it can be either in the spread or the relaxed configuration. Hence a substrate at position c has to be indicated at *two* points in the center of mass space, namely, at $c - \frac{1}{2}$ and $c - 1$; therefore the substrate boxes have width 2. Encircled in the figure are the eight states which have spider 2 at $\bullet \circ \hat{\bullet} \hat{\circ} \hat{\circ}$ or $\circ \bullet \hat{\bullet} \hat{\circ} \hat{\circ}$, respectively, and spider 1 in one of the five states $\bullet \bullet \circ \circ \hat{\circ}, \ldots, \circ \circ \bullet \bullet \hat{\circ}$. The resulting states correspond clearly to those of Eq. (15) and Fig. 4. In the figure, there are three horizontal red boxes (substrates on spider 2's lane), and only one vertical blue box (substrate on lane 1). Hence, the difference of the product sea's ends is $\Delta = 2$. Since the encircled states ①–⑧ have, by direct reading, *only* spider 2 at a substrate (i.e., they are only contained in $\sigma = 1$ box), they form the equivalence class $[\Delta_\sigma] = [2_1]$.

a relaxed configuration, a substrate has to be indicated at *two* different locations in the center of mass space (thus the width of every box equals 2). Furthermore, since spider 1 being or not being at a substrate does not affect spider 2, every box indicating a substrate at spider 1's track has to be of a size that it contains all allowed configurations of spider 2, and vice versa.

We now return to an example discussed in Sec. III B: Equation (15) shows all configurations in which spider 1 has cleaved two more substrates than spider 2 and only spider 2 is attached to a substrate. We referred to this set of configurations as the equivalence class $[\Delta_\sigma] = [2_1]$. This situation is illustrated in Fig. 7, where there are $\Delta = 2$ more boxes (i.e., substrates) for spider 2 than for spider 1. The eight allowed configurations contained by the ellipse in this figure are only contained in *one* box ($\sigma = 1$), such that these states provide a geometrical interpretation of the equivalence class $[2_1]$. Leaving the boundary period in this picture corresponds to removing the encircled box (i.e., cleaving the substrate) and stepping down (i.e., away from the substrate boundary).

E. Diffusive periods

We now employ the mapping of the spider team motion to a confined random walk in order to analyze the spider team's dynamics during a diffusive period. Let us first examine the transition rates between neighboring points in the confined random walk picture. Consider, for example, the point

$$(c_1, c_2) = (0,0) = \begin{smallmatrix} \bullet & \circ & \bullet \\ \bullet & \circ & \bullet \end{smallmatrix} \qquad (19)$$

in Fig. 6. From this configuration, every *leg* may unbind from its product with rate 1, and then rebind to either the same product site again, or move to the allowed neighboring site at equal *probability* $\frac{1}{2}$. In the confined random walk picture, this leads to transition *rates* of $1 \times \frac{1}{2}$ along each connection between adjacent sites from (0,0). The same argument applies to any site within the allowed region, so that the transition rate between any two lattice sites equals $\frac{1}{2}$ [cf. Fig. 8(a)]. This leads to the following master equation for the occupation probability P_{c_1,c_2} on the confined lattice:

$$\frac{d}{dt} P_{c_1,c_2} = \sum_{\langle c_1,c_2 \rangle} \frac{1}{2} \left(P_{\langle c_1,c_2 \rangle} - P_{c_1,c_2} \right), \qquad (20)$$

where the sum runs over all nearest neighbors $\langle c_1, c_2 \rangle$ of (c_1, c_2). In order to calculate the diffusion coefficient $D = \frac{1}{2} \lim_{t \to \infty} \frac{d}{dt} \langle x^2(t) \rangle$ we determine the time derivative of the mean square displacement of the spider team:

$$\frac{d}{dt} \langle x^2(t) \rangle = \sum_{(c_1,c_2) \in \mathcal{C}} x_{c_1,c_2}^2 \sum_{\langle c_1,c_2 \rangle} \frac{1}{2} \left(P_{\langle c_1,c_2 \rangle} - P_{c_1,c_2} \right), \qquad (21)$$

where $x_{c_1,c_2} = \frac{1}{2}(c_1 + c_2)$ is the position of the spider team on the molecular track for given values of c_1 and c_2, and the summation extends over all (c_1, c_2) within the allowed region $\mathcal{C}$. This equation can be reorganized such that

$$\frac{d}{dt} \langle x^2(t) \rangle = \sum_{\mathcal{C}} P_{c_1,c_2} \sum_{\langle c_1,c_2 \rangle} \frac{1}{2} \left(x_{\langle c_1,c_2 \rangle}^2 - x_{c_1,c_2}^2 \right). \qquad (22)$$
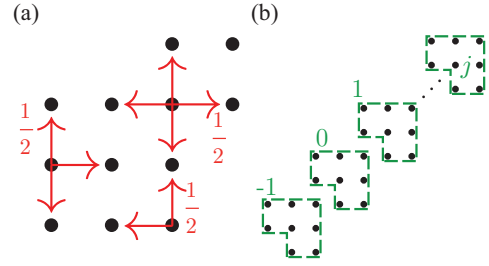
FIG. 8. (Color online) Diffusion in the staircase environment. (a) Transition rates between the sites of the staircase environment. Along every arrow drawn, the rate is $\frac{1}{2}$ leading to local detailed balance. (b) The staircase can be split into elementary cells, numbered with integers.

To evaluate this expression we split the lattice into elementary cells as shown in Fig. 8(b), and use that for asymptotically large times $t \to \infty$, the probability density P varies only little between neighboring elementary cells. This follows from translational symmetry; every cell obeys the same master equation. The master equation, Eq. (20), then implies a nearly uniform probability distribution within each elementary cell j [34]. Upon assuming a constant value P_j within each unit cell, carrying out the sum over an arbitrary elementary cell j leads to a further simplification

$$\sum_{\mathcal{C}_j} P_j \sum_{\langle c_1,c_2 \rangle} \frac{1}{2} \left(x_{\langle c_1,c_2 \rangle}^2 - x_{c_1,c_2}^2 \right) = \frac{1}{2} P_j, \qquad (23)$$

independent of j. Altogether, we obtain

$$\lim_{t \to \infty} \frac{d}{dt} \langle x^2(t) \rangle \approx \sum_{j=-\infty}^{\infty} \frac{1}{2} P_j \overset{(*)}{\approx} \sum_{j=-\infty}^{\infty} \sum_{\mathcal{C}_j} \frac{\frac{1}{2}}{8} P_{c_1,c_2}$$

$$= \frac{1}{16} \sum_{\mathcal{C}} P_{c_1,c_2} \overset{(\dagger)}{=} \frac{1}{16} = 2D, \qquad (24)$$

where in $(*)$ we used that each elementary cell comprises eight points, and in $(\dagger)$ we employed the normalization condition for P. This procedure can be generalized for arbitrary d. The formula for the diffusion constants for $n = 2$ then reads

$$D(d) = \frac{1}{16} + \frac{1}{32(1-d)}. \qquad (25)$$

This theoretical result agrees well with simulation data for the diffusion constant D, as a function of the leash length d (see Fig. 9).

IV. OPTIMIZATION OF DIRECTED MOTION

In the previous sections we mainly focused on ensemble properties of spider teams. However, in experiments or applications one has to deal with single realizations of the stochastic process, i.e., single trajectories [cf. Fig. 2(f)]. Since it is desirable to achieve a molecular motor design that works reliably, one would like to minimize the randomness of the trajectory, i.e., the motion's standard deviation

$$\sigma = \sqrt{\langle (x - \langle x \rangle)^2 \rangle}. \qquad (26)$$

It is interesting to ask how the microscopic properties of the spider team (n,d) influence σ: Can we optimize the
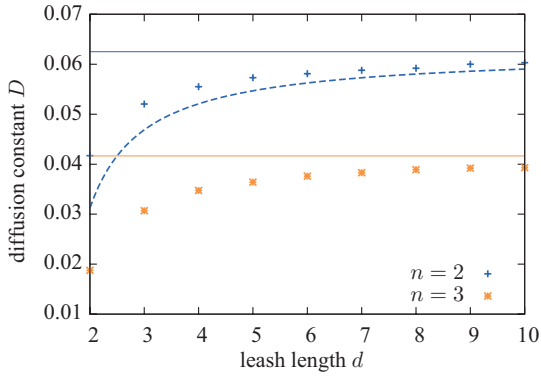
FIG. 9. (Color online) Diffusion constants as a function of the leash length d for $n = 2$ and 3 spiders. The dashed line shows the theoretical result for $n = 2$ [Eq. (25)]; solid lines are asymptotics for $d \to \infty$. Our theoretical approximation is in good agreement with simulation data (points).

performance of a spider team? Is there an optimal choice of parameters n and d which reduces the randomness of a spider teams' motion to a minimum?

The randomness is determined by the interplay between the dynamics of the spider team during its different episodes of motion, i.e., the boundary periods and the diffusive periods. For each episode we found a characteristic feature: During boundary periods the spider team motion is essentially ballistic which can be quantified in terms of the mean number of consecutive steps $\langle S \rangle$ [cf. Eq. (17)]. In contrast, during a diffusive period the spider team performs a random walk with a diffusion constant D [cf. Eq. (25)].

We have already learned in Sec. III C and Fig. 5 that there is an optimal choice of parameters for the number of consecutive directed steps during a boundary period (see Fig. 5). One could now naïvely conclude that the predictability of a spider team's motion can as well be optimized with the same set of parameters. However, this argument would overlook the impact of the diffusive periods. Indeed, there are several effects which influence the randomness during these episodes:

(i) In Sec. III E we noted that the diffusion constant D grows with the leash length d [Eq. (25) and Fig. 9]. Since D determines the mean square displacement during a diffusive period, increasing d would then also imply a *greater* randomness, σ.

(ii) Conversely, a higher diffusion coefficient during diffusive periods speeds up all dynamic processes. Thus, in a given time window, larger d make it more probable for a spider team to return to the boundary and start moving ballistically [35].

The combined effect of these two processes can be estimated by analyzing a random walker with an absorbing boundary. In one dimension, one finds that $\langle x^2(t) \rangle \propto \sqrt{Dt}$ [36,37]. Hence, (i) and (ii) together would lead to an *increase* of σ with d.

(iii) Consider the geometrical interpretation of the transition from the boundary period to the diffusive period as given in Fig. 7. In this picture, entering a diffusive period corresponds to removing the lowermost red box, and stepping to one of the three points below states ⑥−⑧. Right after this transition, the average minimal distance $\langle x_0 \rangle$ of the spider team from the
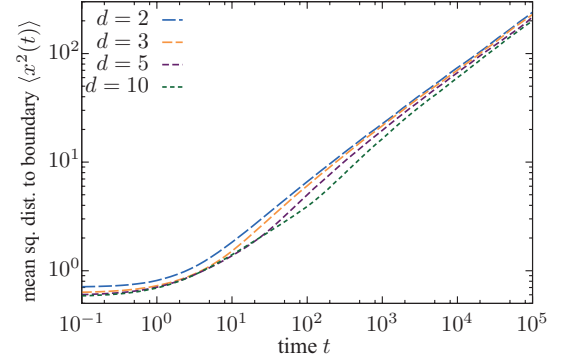
FIG. 10. (Color online) Randomness during a diffusive period. Shown is the mean-squared minimal distance to the boundary of a random walker in the staircase environment ($n = 2$), Fig. 6. The walkers start randomly along every point which provides an entrance to the diffusive period (for $d = 2$, these are the three points below states ⑥-⑧ in Fig. 7); they are absorbed when they reach the boundary (which is the second substrate box in Fig. 7; note that the lowermost box has been removed when the walker entered the diffusive period). Obviously, the mean-squared distance is greater the smaller d is. Increasing d thus decreases the randomness.

boundary is therefore given by

$$\langle x_0 \rangle = \frac{1}{4}\left(3 + \frac{3}{4d - 5}\right), \qquad (27)$$

as can be inferred from counting the different transition pathways. Hence, with increasing d, the spider team entering the diffusive period is closer to the boundary, and is thereby more likely to reenter a boundary period quickly.

(iv) In Sec. III D we have shown that with increasing leash length d the number of pathways in state space to reenter a boundary period also increases. Pictorially, this can be inferred from the mapping of the spider team's motion to a random walker in a staircase environment: The longer the leash length
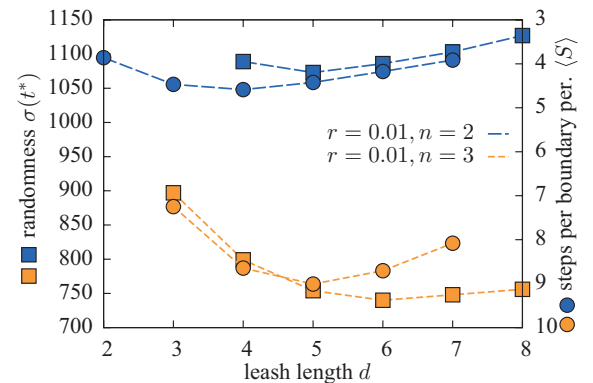
FIG. 11. (Color online) Standard deviation σ of the spider teams' movement and the mean number of steps $\langle S \rangle$ as a function of the leash length d. Both σ and $\langle S \rangle$ show extrema. To emphasize the correspondence between the minimum of σ and the maximum of $\langle S \rangle$ (cf. Fig. 5), the $\langle S \rangle$ axis is drawn in reverse (see right scale). σ is measured at the time t^* when the mean displacement $\langle x \rangle$ equals 1000. This choice is arbitrary; for smaller values the minima of σ persist, but are less pronounced [cf. Fig. 2(b)].

TABLE II. Optimal values of d for $n = 2$ and 3, and several values of r. Compared are the values of d which maximize the mean number of steps during a boundary period, and that which minimize the randomness (for a comparison see Fig. 11). Clearly, both values of d are closely correlated, where $d_{\langle S \rangle}^{\text{opt}}$ is only slightly smaller than d_{σ}^{opt}.

	$n = 2$		$n = 3$	
r	$d_{\langle S \rangle}^{\text{opt}}$	d_{σ}^{opt}	$d_{\langle S \rangle}^{\text{opt}}$	d_{σ}^{opt}
0.001	$\sim$10–11	$\sim$13		
0.01	4	5	5	6
0.02	3	4	3–4	4–5
0.05	2	3		
0.1	2	3	2	3
0.2	2	2	2	3

d the larger is the "angle" under which a random walker sees the boundary of the staircase. Thus, when the random walker takes an arbitrary direction the probability that it walks toward the boundary is increasing with d.

Since there is no unique trend in the various effects discussed above in (i)–(iv), it is difficult to conclude what would be the dominant effect of the diffusive period on the randomness. Therefore, we numerically determine the randomness of the spider team during diffusive periods [38]; this quantity is depicted in Fig. 10. We observe that the mean squared distance from the boundary is smaller for larger d at all times. This implies that—considering only diffusive periods—increasing d leads to a *reduction* of the randomness. From this we can infer that the effects (iii) and (iv), which decrease the randomness of the process with increasing d, overcompensate the effects (i) and (ii).

Altogether we can now conclude the influence of the diffusive periods as follows:

$$d \nearrow \Rightarrow \sigma \searrow .$$

Analogously we can decipher the influence of boundary periods. Going back to Fig. 5 we observe

$$d < d_{\langle S \rangle}^{\text{opt}} : d \nearrow \Rightarrow \langle S \rangle \nearrow \Rightarrow \sigma \searrow ,$$

$$d > d_{\langle S \rangle}^{\text{opt}} : d \nearrow \Rightarrow \langle S \rangle \searrow \Rightarrow \sigma \nearrow .$$

These considerations explain that *if* there is an optimal value d_{σ}^{opt} at which the randomness becomes minimal, it must be found beyond $d_{\langle S \rangle}^{\text{opt}}$. This is in agreement with our data: Figure 11 shows the existence of a minimum of the randomness, and its positioning with respect to $d_{\langle S \rangle}^{\text{opt}}$. Remarkably, the positions of both optima are strongly correlated (see Table II).

In conclusion, our analysis shows that the randomness of the spider team is mainly determined by the mean number of steps $\langle S \rangle$ during boundary periods. Diffusive periods have only a small effect on the randomness and change the optimal parameters only slightly.

V. CONCLUSIONS

Based on existing models for molecular spiders [11,12], we proposed a model for a spider team that explores the collective behavior of cooperating spiders: In our model, bipedal spiders are jointly attached to a (zero-mass) linking cargo. Each spider

walks on its own one-dimensional track. This leads to a spacial constraint which can be characterized by the maximal span d of the resulting spider team.

Depending on the cleavage rate of the substrate $r < 1$, the number of coupled spiders n, and the leash length d, we found that the coupling leads to a significant enhancement of many of the spider's motor properties: Spider teams show a significant increase of their mean displacement; their motion is a lot less random; the ensemble's velocity can be increased by more than an order of magnitude; and the superdiffusive behavior lasts longer for orders of magnitude in time. Unlike single spiders, cooperating spiders could therefore—at least in theory—be employed for executing well-defined tasks reliably.

Like their individual counterparts [16], spider teams' motion can be characterized as being in either a boundary or a diffusive period. We found that the characteristic quantity is the mean number of consecutive directed steps $\langle S \rangle$ which a spider team performs during a boundary period. In simplified language, $\langle S \rangle$ integrates the number of steps which the spider teams walk, as long as it stays in the vicinity of the comoving boundary between substrate and product sites. $\langle S \rangle$ is closely related to the bias p_+ of single spiders [12]. For small r, we succeeded in calculating $\langle S \rangle$ analytically through an equivalence class formalism which made use of the time scale separation of dwell times on products and substrates. This formalism is exact for $r \to 0$, regardless of the number of coupled spiders and the tightness of the coupling. We explicitly calculated values for various small spider teams, and find excellent agreement with simulation data. For small but finite cleavage rates r, the formalism still holds as an approximation for relatively tight coupling. We found that in this case there is an optimal value for the coupling tightness d which maximizes the mean number of steps.

Next, we provided a mapping of the stochastic motion of an n-spider team to a random walker in an n-dimensional environment. The motion is confined between parallel boundaries which have the shape of staircases. This mapping is exact and allows a complementary interpretation for the equivalence classes: Substrates can be drawn as boxes which are easy to enter for random walkers but impossible to leave without removing, which happens slowly on a time scale r^{-1}. It is then straightforward to see that an equivalence class corresponds to an intersection of boxes (cf. Fig. 7). The staircase picture also allows one to quantify the dynamics during the diffusive periods of spider teams: In that case, boxes can be ignored and spider teams correspond to ordinary diffusive random walkers on the confined lattice. We calculated the diffusion constants for two-spider teams and find good agreement with simulation data.

The analysis of the mean number of consecutive steps during a boundary period $\langle S \rangle$ (which shows a maximum for some value of the leash length d), taken together with the diffusion constants D (which grow with d) allow for a comprehensive explanation of our observations. We show that the optimal value of d that minimizes the randomness (which involves boundary and diffusive periods) differs only slightly from the leash length maximizing the mean number of steps during a boundary period (see Fig. 11).

The staircase picture also illustrates that despite the difference in complexity, a single spider and a spider team can

both be described by similar effective random walk models: The motion of a bipedal spider which has a nontrivial stepping gait can be fully described by its center of mass coordinate which performs simple one-dimensional random walks [12]. Likewise, the motion of an n-spider team which involves complicated interactions between the spiders can equivalently be described by another single coordinate which performs n-dimensional random walks that are, however, geometrically confined due to the leash constraint.

Our results show that the primary factor for improving the motor properties of molecular spiders is the accessibility of substrate sites for the spider legs: While single spiders only have access to one substrate at a time, an n-spider team can reach n substrates. This would imply that there is a significant difference between truly one-dimensional spiders [12] and quasi-one-dimensional spiders [10]. This is enforced by a very recent study of Olah *et al.* [19] who examined molecular spiders on a narrow two-dimensional lattice. As well, it is in full accordance with recent data by Samii *et al.* [18] who concentrated on hand-over-hand spiders: They showed that motor properties of this class of spiders which have access to more than one substrate site at a time are superior to inchworm spiders which can only reach one substrate at once [17,18].

The results presented here can be extended in multiple ways. In analogy to individual spiders, further studies could concentrate on varying design specifics like the number or the length of legs [18]. Likewise, the underlying chemical processes [9,10] could be modeled in greater molecular detail also for spider teams. Similarly, the team's spiders' stepping gait could be varied, potentially profiting from studies about the motion of individual hand-over-hand spiders with more than two legs [18] which seem to be difficult to realize in the experiment.

Unlike other studies (e.g., [16]) which have extensively investigated the role of the cleavage rate r, our focus was different and the variation of r was only a side aspect of this work. Nevertheless, our analysis hints towards a scaling behavior which maps the quantity $\langle S(r,d) \rangle$ to a universal form $\tilde{S}(\tilde{d})$ which is independent of r. In this spirit, it would also be interesting to study the connection of the optimal leash length and the cleavage rate r. It appears that this relation might be rather simple for a wide parameter range, although its mathematical formulation seems to be very complex. The difficulty is that the simplified formulation of the problem presented here, i.e., the equivalence classes, cannot be applied directly. One possibility to address this problem might lie in drawing analogies from related models such as the burnt-bridge model [39]. For example, it has been studied for dimeric motor molecules [40] and as an exclusion process [41].

Our results might also be relevant to study collective properties of molecular motor assemblies theoretically (cf. e.g. Ref. [42] or Ref. [43], and references therein). These models are relevant to understand the interplay between biological motor molecules such as kinesin, dynein, and myosin inside cells [44,45]. In contrast to spiders, biological motors are fueled by ATP hydrolysis; they can build up significant pulling forces due to strong mechanochemical coupling [46]. In particular, recent experiments addressed the complex interplay of multiple coupled kinesin motor proteins where the motors are coupled via a DNA leash of certain length. It is interesting

to note how in these experiments teams of two kinesin motors outperform a single motor in terms of run length and pulling forces [47–49]. Similarly, cooperative effects also improve the properties of two coupled burnt-bridge motors modeling collagenase transport [40].

In conclusion, we believe that our model of coupling molecular spiders provides insight on how cooperative behavior evolves on the molecular scale. We hope that our ideas about molecular spiders help advance a young and fast growing field in which much focus is put on the construction of novel, more efficient molecular designs [4]. We believe that our findings are not limited to the case of molecular spiders, but apply to molecular machines working together in general.

APPENDIX: DERIVATION OF EQ. (17)

We analyze the graph for a two-spider team with arbitrary d as depicted in Eq. (14). According to this graph, transitions $[i] \rightarrow [i \pm 1]$ are equally likely as long as $i < d$, whereas $[d] \rightarrow [d-1]$ happens at probability Π. During every transition, the spider team performs a fractional step $\frac{1}{n} = \frac{1}{2}$. Only during the transition $[d] \rightarrow [d-1]$, no step is integrated; in return, $[d-1] \rightarrow [d]$ leads to a whole step for the team. This is due to the very definition of the number of steps during a boundary period, which comprises all cleavages but for each spider's last cleavage before the team enters the diffusive period.

With these preparations, we can now establish the probabilities $p(j|[i])$ that a spider team, being in class $[i]$, performs exactly j steps before leaving into the diffusive period. These read

$$
\begin{aligned}
p(j|[0]) &= p(j - \tfrac{1}{2}|[1]), \\
p(j|[i]) &= \tfrac{1}{2}\big(p(j - \tfrac{1}{2}|[i-1]) + p(j - \tfrac{1}{2}|[i+1])\big), \\
p(j|[d-1]) &= \tfrac{1}{2}\big(p(j - \tfrac{1}{2}|[d-2]) + p(j|[d])\big), \\
p(j|[d]) &= \Pi p(j-1|[d-1]) \quad\quad\quad\quad\quad\quad\text{(A1)}
\end{aligned}
$$

where $0 < i < d-1$. The *mean* number of steps $\langle S(x) \rangle$ which a spider team walks from class $[x]$ until going to the diffusive period is then given by

$$
\langle S(x) \rangle = \sum_{j=0,\frac{1}{2},\dots}^{\infty} j\, p(j|[x]). \quad\quad\quad\text{(A2)}
$$

Inserting Eq. (A2) into Eq. (A1), and by renumbering indexes we obtain

$$
\begin{aligned}
\langle S(0) \rangle &= \tfrac{1}{2} + \langle S(1) \rangle, \\
\langle S(i) \rangle &= \tfrac{1}{2} + \tfrac{1}{2}\langle S(i-1) \rangle + \tfrac{1}{2}\langle S(i+1) \rangle, \\
\langle S(d-1) \rangle &= \tfrac{1}{4} + \tfrac{1}{2}\langle S(d-2) \rangle + \tfrac{1}{2}\langle S(d) \rangle, \\
\langle S(d) \rangle &= \Pi + \Pi\langle S(d-1) \rangle,
\end{aligned} \quad\text{(A3)}
$$

where again $0 < i < d - 1$. Solving this system of equations, we obtain the recursion relation

$$\langle S(k) \rangle = \langle S(k+1) \rangle + k + \tfrac{1}{2} \qquad (A4)$$

for $0 \leqslant k < d - 2$. Substituting this into the remaining equations leads to

$$\langle S(d) \rangle = \frac{\Pi d}{1 - \Pi}, \qquad (A5)$$

and finally

$$\langle S(d-1) \rangle = \frac{d}{1-\Pi} - 1 = (d-1)\frac{1}{1-\Pi} + \frac{\Pi}{1-\Pi}. \qquad (A6)$$

Since a spider always enters a boundary period in class $[d-1]$ in the limit $r \to 0$ [cf. Eq. (13)], the last equation is equivalent to $\langle S \rangle$, Eq. (17).

[1] J. Howard, *Mechanics of Motor Proteins and the Cytoskeleton* (Sinauer Associates, Sunderland, MA, 2001).

[2] J. Bath and A. J. Turberfield, Nat. Nanotech. **2**, 275 (2007).

[3] R. D. Astumian, Biophys. J. **98**, 2401 (2010).

[4] A. V. Pinheiro, D. Han, W. M. Shih, and H. Yan, Nat. Nanotech. **6**, 763 (2011).

[5] W. B. Sherman and N. C. Seeman, Nano Lett. **4**, 1203 (2004).

[6] J.-S. Shin and N. A. Pierce, J. Am. Chem. Soc. **126**, 10834 (2004).

[7] M. von Delius and D. A. Leigh, Chem. Soc. Rev. **40**, 3656 (2011).

[8] Y. Tian, Y. He, Y. Chen, P. Yin, and C. Mao, Angew. Chem., Int. Ed. Engl. **44**, 4355 (2005).

[9] R. Pei, S. K. Taylor, D. Stefanovic, S. Rudchenko, T. E. Mitchell, and M. N. Stojanovic, J. Am. Chem. Soc. **128**, 12693 (2006).

[10] K. Lund, A. J. Manzo, N. Dabby, N. Michelotti, A. Johnson-Buck, J. Nangreave, S. Taylor, R. Pei, M. N. Stojanovic, N. G. Walter, E. Winfree, and H. Yan, Nature (London) **465**, 206 (2010).

[11] T. Antal, P. L. Krapivsky, and K. Mallick, J. Stat. Mech.: Theory Exp. (2007) P08027.

[12] T. Antal and P. L. Krapivsky, Phys. Rev. E **76**, 021121 (2007).

[13] T. Chou, K. Mallick, and R. K. P. Zia, Rep. Prog. Phys. **74**, 116601 (2011).

[14] M. Mobilia, T. Reichenbach, H. Hinsch, T. Franosch, and E. Frey, Banach Cent. Publ. **80**, 101 (2008).

[15] B. Derrida, M. Evans, and K. Mallick, J. Stat. Phys. **79**, 833 (1995).

[16] O. Semenov, M. J. Olah, and D. Stefanovic, Phys. Rev. E **83**, 021117 (2011).

[17] L. Samii, H. Linke, M. J. Zuckermann, and N. R. Forde, Phys. Rev. E **81**, 021106 (2010).

[18] L. Samii, G. A. Blab, E. H. C. Bromley, H. Linke, P. M. G. Curmi, M. J. Zuckermann, and N. R. Forde, Phys. Rev. E **84**, 031111 (2011).

[19] M. J. Olah and D. Stefanovic, arXiv:1211.3482.

[20] T. Antal and P. L. Krapivsky, Phys. Rev. E **85**, 061927 (2012).

[21] C. Gallesco, S. Müller, and S. Popov, ESAIM: Probab. Stat. **15**, 390 (2011).

[22] I. Ben-Ari, K. Boushaba, A. Matzavinos, and A. Roitershtein, Bull. Math. Biol. **73**, 1932 (2011).

[23] C. Gallesco, S. Müller, S. Popov, and M. Vachkovskaia, ALEA, Lat. Am. J. Probab. Math. Stat. **8**, 129 (2011).

[24] R. Juhász, J. Stat. Mech.: Theory Exp. (2007) P11015.

[25] J. D. Watson and F. H. C. Crick, Nature (London) **171**, 737 (1953).

[26] This differs from the original model of Antal *et al.* [11] who allowed rebinding only to *different* sites.

[27] C. B. Korn, S. Klumpp, R. Lipowsky, and U. S. Schwarz, J. Chem. Phys. **131**, 245107 (2009).

[28] M. Brunnbauer, R. Dombi, T.-H. Ho, M. Schliwa, M. Rief, and Z. Ökten, Mol. Cell **46**, 147 (2012).

[29] S. Ray, E. Meyhöfer, R. Milligan, and J. Howard, J. Cell Biol. **121**, 1083 (1993).

[30] J.-P. Bouchaud and A. Georges, Phys. Rep. **195**, 127 (1990).

[31] Note that $r = 0$ is unphysical since it would not allow substrate cleavage. Therefore, the limit $r \to 0$ has to be understood as a time separation limit where substrate cleavage is much slower than stepping of legs from product sites, i.e., $r \ll 1$.

[32] C. Leduc, F. Ruhnow, J. Howard, and S. Diez, Proc. Natl. Acad. Sci. USA **104**, 10847 (2007).

[33] Following the definition of a step done by a spider team in Sec. III B, no step is counted along with the transition $[d-1] \to [d]$, since this is potentially the last cleavage event of the spider which caused this transition. To compensate this (if this spider makes another cleavage), the transition $[d] \to [d-1]$ is counted as two (half) steps.

[34] Note that global equilibrium is never reached in this system due to the open boundaries.

[35] Note that although the random walker is recurrent its recurrence time is infinite [50].

[36] N. G. van Kampen, *Stochastic Processes in Physics and Chemistry* (Elsevier, New York, 2007).

[37] S. Redner, *A Guide to First-Passage Processes* (Cambridge University Press, Cambridge, 2009).

[38] It is convenient to run the simulations in the staircase picture (cf. Fig. 7). We assume that each of the three points below ⑥-⑧ in this figure is an equally likely starting point, and set up an absorbing boundary at the lowermost substrate box.

[39] T. Antal and P. L. Krapivsky, Phys. Rev. E **72**, 046104 (2005).

[40] A. Y. Morozov and A. B. Kolomeisky, J. Stat. Mech. (2007) P12008.

[41] J. H. P. Schulz, A. B. Kolomeisky, and E. Frey, Europhys. Lett. **95**, 30004 (2011).

[42] F. Berger, C. Keller, S. Klumpp, and R. Lipowsky, Phys. Rev. Lett. **108**, 208101 (2012).

[43] T. Guérin, J. Prost, P. Martin, and J.-F. Joanny, Curr. Opin. Cell Biol. **22**, 14 (2010).

[44] S. P. Gross, M. Vershinin, and G. T. Shubeita, Curr. Biol. **17**, R478 (2007).

[45] E. L. F. Holzbaur and Y. E. Goldman, Curr. Opin. Cell Biol. **22**, 4 (2010).

[46] A. B. Kolomeisky and M. E. Fisher, Annu. Rev. Phys. Chem. **58**, 675 (2007).

[47] A. R. Rogers, J. W. Driver, P. E. Constantinou, D. Kenneth Jamison, and M. R. Diehl, Phys. Chem. Chem. Phys. **11**, 4882 (2009).

[48] J. W. Driver, D. K. Jamison, K. Uppulury, A. R. Rogers, A. B. Kolomeisky, and M. R. Diehl, Biophys. J. **101**, 386 (2011).

[49] D. K. Jamison, J. W. Driver, and M. R. Diehl, J. Biol. Chem. **287**, 3357 (2012).

[50] G. Polya, Math. Ann. **84**, 149 (1921).

Part II.

The impact of finite resources for microtubule length regulation by molecular motors

5. Motivation

Cell division is orchestrated by a complex machinery called the mitotic spindle which is composed of microtubules (MTs). One of its crucial tasks is to guide and maintain chromosomes in the cell center, before subsequently segregating them into the daughter cells (6, 7). Control of the size of the mitotic spindle and likewise MT length is essential for the proper function of a cell (188). A central questions is how length regulation is achieved inside cells. It is known that many proteins are involved in this process in a complex interplay.

Among these proteins, molecular motors of the kinesin-8 family play a special role: It has been found that spindle size increases when this protein is depleted (126), while its overexpression results in smaller spindles (127). This effect has been attributed to the ability of kinesin-8 to depolymerise MTs at their plus ends (20, 189, 190). Moreover, it has been observed that the kinesin-8 homolog Kip3 from *Saccharomyces cerevisiae* depolymerises MTs in a length-dependent fashion (20, 21). A simple explanation for this behaviour is the existence of a motor density gradient on the MT, which arises from the interplay of random attachment to, and directed motion on it. Effectively, this leads to a mechanism how MTs can "sense" and regulate their own length (21–23, 191).

At the same time, there is evidence that spindle formation significantly depletes the concentration of tubulin and other proteins. In particular, spindle size is modulated by cytoplasmic volume both *in vitro* and *in vivo* (24, 25). Because spindle size correlates with MT length (27), the availability of resources is also important for the length of individual filaments. A detailed study of how molecular motors like kinesin-8 are involved in the length regulations of MTs must therefore also take limited resources into account.

In the following we will present results on two related projects, where we consider the role of finite resources for a MT length regulation process by kinesin-8. In the first part, Chap. 6, our focus lies on direct applicability of our model to a set of *in vitro* experiments. This project results from a very fruitful collaboration with Aniruddha Mitra from the group of Stefan Diez (Dresden), that started at a conference in Berlin in December 2015. At the time of the original submission of this thesis, the findings of our study had been submitted for publication. In the meantime, they have been published in *Physical Review Letters, 120, 14 (2018)* under the title "Limited Resources Induce Bistability in Microtubule Length Regulation". In this thesis, we follow this journal's structure and present our main results in Chap. 6, while most mathematical derivations and additional experimental tests are presented in Appendix A.

The final Chap. 7 of this part considers a simpler model for MT length regulation in a finite volume. In fact, it was our first project to be conducted in the field of limited resources. Although it has less biological significance, all the phenomena present in the more complex model can be observed, and a more thorough analysis is possible due to its simplicity.

6. Limited resources induce bistability in microtubule length regulation

The absolute and relative abundance of particular sets of proteins is important for a wide range of processes in cells. For example, during *Xenopus laevis* embryogenesis, importin α becomes progressively localized to the cell membrane (192). As a consequence of importin's depletion from the cytoplasm, the protein kif2a escapes inactivation, and decreases the size of the mitotic spindle. Similarly, formation of the mitotic spindle reduces the concentration of free tubulin dimers, the building blocks of microtubules (MTs). Thus, up to 60% of all tubulin heterodimers (41, 42) may be incorporated into the spindle (25). In addition, it has been shown *in vivo* and *in vitro* that both spindle size (24, 25) and the lengths of its constituent MTs (27) scale with cytoplasmic volume.

Assembly and disassembly of MTs are regulated by a set of proteins that interact with the plus ends of protofilaments (5, 189). One of these factors, the molecular motor kinesin-8, acts as a depolymerase (20, 189). As a consequence, spindle size increases in its absence (126), and decreases upon overexpression of the protein (127). Moreover, the kinesin-8 homolog Kip3 from *Saccharomyces cerevisiae* has been shown to depolymerize MTs in a length-dependent fashion (20, 21). This is facilitated by a density gradient on the MT, caused by the interplay between the processive motion of Kip3 along the MT and its depolymerase activity at the plus end, which effectively enables the MT to "sense" its own length (21, 22). In combination with spontaneous MT polymerization, the Kip3 gradient leads to a length regulation mechanism (23, 191).

Here we explore the combined effect of limited resources and Kip3-induced depolymerization on the length regulation of MTs. As seen in theoretical studies on the collective motion of molecular motors, resource limitation affects the density profile on the MT: Regions of low and high motor density separate, as a localized domain wall emerges on the MT (154, 162–164). This is a direct result of resource limitation, and does not rely on the existence of a motor density gradient, as necessary for domain wall localization in the presence of unlimited resources (132, 133, 155, 156). So far, most work on the role of limited resources has focused on single components of the relevant system (161–164, 193–196). Only a few studies have considered simultaneous limitation of two resources (165). In particular, the role of resource limitation has not been explored when two processes with antagonistic actions are concurrently affected by the limited availability of protein.

In this Letter, we study the impact of limitations in the supply of both tubulin and the depolymerizing molecular motor Kip3 on the regulation of MT length. We build on a recently validated quantitative model of MT dynamics (23), and extend it to include the constraint of resource limitations. We find that Kip3 can tightly control MT length, irrespective of the specific parameter choice. Over a broad range of tubulin and kinesin concentrations, length regulation is bistable, i.e., the MT can assume one of two stationary states. We corroborate these findings by performing *in vitro* experiments, which show that the MT length distribution is indeed bimodal for certain concentrations of the components of interest, in accordance with the theoretical expectations.
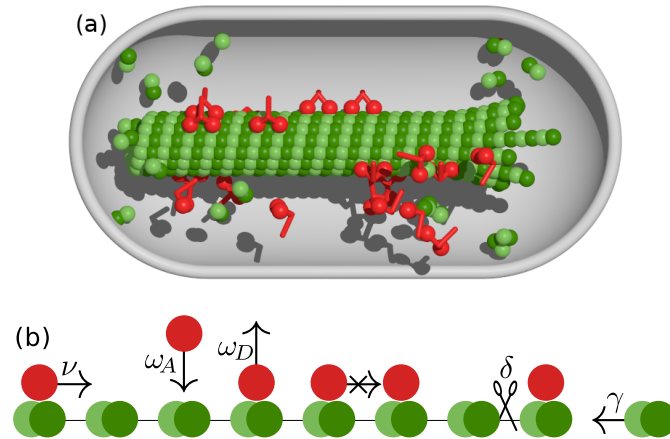
Figure II.1.: Sketch of the model. (a) A MT in a closed volume interacts with molecular motors. (b) Motors attach to the MT lattice at rate ω_A, and detach at rate ω_D. Motors proceed stepwise toward the plus end at rate v, provided the next site is unoccupied. At the tip, motor-induced lattice depolymerization (rate δ) competes with spontaneous polymerization (rate γ). ω_A and γ and depend on the concentrations of the proteins available in the closed volume, Eqs. (II.1).

To investigate the impact of limited resources on MT dynamics, we employ a driven diffusive lattice gas model (145, 149, 153) for spontaneous MT polymerization and kinesin-catalyzed MT depolymerization (23, 191), as illustrated in Fig. II.1. As kinesin-8 motors predominantly move along single protofilaments (106, 107), it suffices to consider a one-dimensional lattice of dynamic length $L(t)$. The state of each site, i, is described by its occupation number, n_i, where $n_i = 0$ and $n_i = 1$ signify an empty and occupied site, respectively. On the MT lattice the dynamics follow the totally asymmetric simple exclusion process with Langmuir kinetics (TASEP/LK) (154–156, 197): Motors can attach to any empty site on the MT lattice at rate ω_A, and detach at rate ω_D. Since binding of motors to the MT depletes the volume concentration of motors c_m, the attachment rate ω_A decreases as

$$\omega_A = \omega_A^0 (c_m - m/V) . \tag{II.1a}$$

Here m is the number of motors attached to a protofilament, and V is the effective volume available to the motors, see Sec. A.3 in Appendix A. We are specifically interested in the molecular motor Kip3 (20, 198), which is the kinesin-8 homolog in *S. cerevisiae*. Based on published *in vitro* single-molecule experiments, we estimate its detachment rate to be $\omega_D = 4.9 \cdot 10^{-3}$ s^{-1} and the attachment rate to any vacant site as $\omega_A^0 = 6.7 \cdot 10^{-4}$ nM^{-1} s^{-1} (21); see Sec. A.3. On a protofilament, motors move toward the plus end at rate $v = 6.35$ s^{-1} provided that the next site is empty (21). At the plus end, Kip3 catalyzes MT shrinkage (199). This is described as a stochastic process where a motor arriving at the last site removes it at rate $\delta = 2.3$ s^{-1} (21). At the same time, MTs polymerize spontaneously through attachment of single tubulin heterodimers to their plus ends. As tubulin resources are limited, this decreases the volume concentration of tubulin c_T and
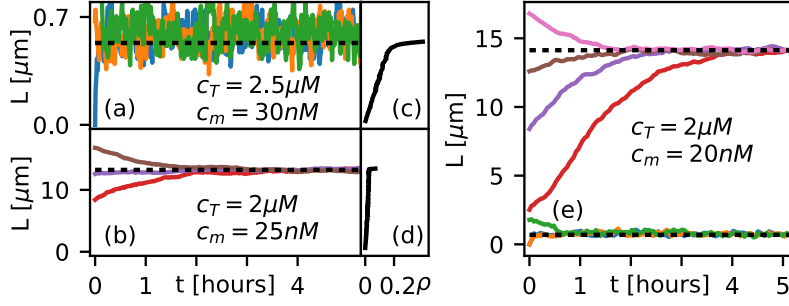
Figure II.2.: Basic phenomenology. Differently colored traces depict different simulation runs under the indicated starting conditions. (a)–(b) MTs evolve toward a stationary length, which depends on the concentrations of Kip3 and tubulin. (c)–(d) The corresponding motor density ρ on the MT is shown; see Fig. II.6e in Appendix A: ρ increases with distance from the minus end, and peaks at the plus end. (e) The MT length is bistable for a range of concentrations. Dotted lines: Results of the full mean-field theory.

the polymerization rate,

$$\gamma = \gamma^0 \left[c_T - L/(aV) \right],$$ (II.1b)

decreases with increasing MT length; here, a = 8.4 nm is the size of a tubulin dimer (51), the (net) polymerization rate per protofilament is γ_0 = 0.38 $\mu M^{-1} s^{-1}$ (49, 200), and the effective volume is $V \approx 1.66 \, \mu m^3$ (Sec. A.3 in Appendix A).

We performed extensive stochastic simulations (201), and explored how the MT dynamics depend on the volume concentration of the motor Kip3, c_m, and tubulin, c_T. Figure II.2a and II.2b show the dynamics of MT length for two representative concentrations of both components, and for various initial MT lengths. In all cases, the MT length reaches a stationary state, albeit at different values. Moreover, the corresponding motor density ρ also differs (Figs. II.2c–II.2d): While for a short stationary length, the overall motor density is relatively high, it remains low when the MT length is long. For both cases, the motor density peaks at the plus end (forming a "spike").

We observe that the stationary MT length depends on its initial value for a certain range of tubulin and kinesin concentrations. Here, depending on whether the MT starts from a single tubulin dimer or a fully polymerized filament with all tubulin resources depleted, the stationary length is short or long, respectively, i.e. the MT dynamics is bistable (Fig. II.2e). This is fundamentally different from MT length regulation with unlimited resources (23, 191), where only one stationary state of finite length is observed. A parameter scan of the tubulin and Kip3 concentrations (Figs. II.3a–II.3b) shows that bistable length regulation occurs over a broad parameter range.

What physical processes determine MT length and lead to bistability? To answer this question one needs to analyze the intricate interplay between the crowding of molecular motors in the lattice bulk (154, 156) and the (de)polymerization kinetics at the MT tip (22), as well as the exchange of resources between filament and solution. The rate of change of protofilament length is determined by the antagonism between spontaneous polymerization and Kip3-driven depoly-
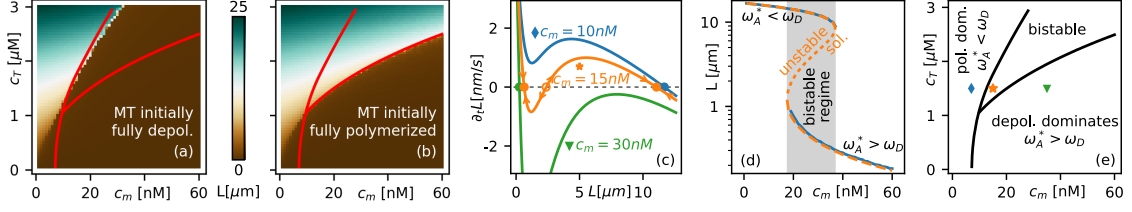
Figure II.3.: *Theoretical results. (a)–(b) In silico scans of the stationary length of MTs, shown in color, as a function of c_m and c_T. Simulations start from a fully depolymerized lattice (short) in panel (a), in (b) the MT is initially fully polymerized (i.e., long). In the region bounded by the red lines (obtained from the full MF theory, see Appendix A), the stationary length differs for these two cases: Here, MT dynamics is bistable. (c) Rate of change of the MT length, $\partial_t L$, as a function of L at $c_T = 1.5\,\mu M$ for three different motor concentrations, as obtained from the approximate MF theory. For low and high motor concentrations, MT length is monostable, while for intermediate concentrations, two stable stationary states are separated by an unstable state (bistability). (d) Comparison of the steady-state length obtained from simulations (blue) and the full MF theory (orange) at $c_T = 2\,\mu M$. (e) Stability diagram as obtained from the full MF theory.*

merization kinetics,

$$\partial_t L(t) = \big[\gamma(t) - \rho_+(t)\delta\big]a\,,\tag{II.2a}$$

where ρ_+ is the probability that the terminal site, i.e. the site directly at the MT tip, is occupied by a motor. The number of motors on the protofilament changes when a motor attaches to one of the empty lattice sites, or any of the motors on it detaches; the number also decreases when a motor falls off the plus end, taking the last tubulin heterodimer with it. Together, this yields

$$\partial_t m(t) = \omega_A(t)\big[L(t)/a - m(t)\big] - \omega_D m(t) - \rho_+(t)\delta.\tag{II.2b}$$

In Eqs. (II.2), the tip density ρ_+ drives the loss of tubulin dimers and motors due to depolymerization. This density, in turn, is determined by the flux of motors along the protofilament toward the MT tip. We assume that these bulk dynamics are fast in comparison to MT length changes due to polymerization and depolymerization. Given this time scale separation, the bulk density can be assumed to be stationary (Sec. A.2 in Appendix A), such that the tip density is determined by a balance between bulk current and depolymerization current. Neglecting correlations in the motor density, $\langle n_i n_j \rangle \approx \langle n_i \rangle \langle n_j \rangle$, and imposing a continuum limit, the mean-field (MF) bulk current is given by $j(x) = v\rho(x)[1 - \rho(x)]$, where $\rho(x)$ denotes the average motor density at position x. On length scales of the order of the size of a tubulin dimer a, this current is constant since $\omega_A, \omega_D \ll v$, such that the motor flux in the MT bulk equals the flux off the tip: $v\rho_{L-a}(1 - \rho_{L-a}) \approx \rho_+\delta$. Here, the subscript $L - a$ signifies that the density is evaluated very close to the MT plus end, just before the density spike begins (cf. Fig. II.2c–II.2d); note that in general $\rho_+ \neq \rho_{L-a}$.

In order to determine the bulk density ρ_{L-a}, one needs to consider the combined effects of steric exclusion and motor exchange between filament and cytosol along the complete MT. In

the stationary state, changes in motor density caused by transport are balanced by attachment-detachment kinetics, i.e.,

$$va(2\rho - 1)\partial_x\rho = -\omega_A(1 - \rho) + \omega_D\rho \ . \tag{II.3}$$

This differential equation has solutions in terms of Lambert W-functions (155, 156) which allow one to compute ρ_{L-a} without any further approximations (Sec. A.2 in Appendix A). However, much can already be learned from an approximate solution, where the density is approximated as a Taylor series, $\rho(x) \approx Ax + Bx^2$; note that $\rho(0) = 0$. Upon inserting this expression into Eq. (II.3), A and B can be read off by comparing the coefficients in the ensuing power series, and using $\rho_{L-a} \approx \rho(L)$. The motor current off the MT, $\rho_+\delta$, is now readily computed, and one obtains to second order in $\omega_{A,D}L/a$:

$$\rho_+\delta \approx \omega_A L/a - (\omega_A + \omega_D)(L/a)^2\omega_A/(2v) \ . \tag{II.4}$$

With Eqs. (II.2) and (II.4), we have arrived at a closed set of (nonlinear) equations for the dynamics of the MT length and the number of motors bound to a protofilament. It can be viewed as a dynamical system which, as a function of the control parameters c_m and c_T, may show bifurcations in the number and nature of its steady states.

The dynamics of nonlinear systems is best visualized by the flow field $(\partial_t m, \partial_t L)$ in phase space. Here, the MT state, described by L and m, evolves along the lines drawn in a stream plot (Figs. II.21). This analysis shows that the number of motors bound to the MT equilibrates almost instantaneously, much more rapidly than the MT length changes. Therefore, we can assume that the dynamics reduces to the subspace (nullcline) $\partial_t m = 0$. This adiabatic elimination of m yields an effective dynamics of the MT length $L(t)$, as shown in Fig. II.3c. Keeping the tubulin concentration fixed at a typical value of 1.5 μM, we find that if the motor concentration is either low ($c_m = 10$ nM) or high ($c_m = 30$ nM)), there is only a single state where the MT length becomes stationary. Hence, regardless of its initial length, a MT will always reach a uniquely defined stable steady length (monostability). By contrast, for intermediate motor concentrations ($c_m = 20$ nM), we observe bistability: Here, three stationary states exist, two stable states for long and short MT lengths, respectively, and one unstable state at intermediate MT length, see Fig. II.3c. This implies that, depending on its initial length, a MT may either grow long or remain short. The same behavior is observed for the full MF analysis, which includes an exact solution of Eq. (II.3); see Sec. A.2 in Appendix A.

Figure II.3d shows that the results obtained from the full MF theory compare very well with those of the stochastic simulations. In particular, we consistently observe a bistable regime, with two stable solutions separated by an unstable solution (separatrix). The stability diagram shown in Fig. II.3e summarizes the different regimes of length regulation as a function of protein concentrations. In the regimes dominated by depolymerization or polymerization, the stationary MT length will be short or long, respectively. At intermediate protein concentrations, the MT length may be short or long depending on the initial length (bistable regime).

While these results have been obtained for a single MT, they are not limited to this case. We find that when many MTs globally access proteins in a well-mixed pool, length regulation is still accurate, see Sec. A.5 in Appendix A. Moreover, the total length of MTs is bistable in a concentra-
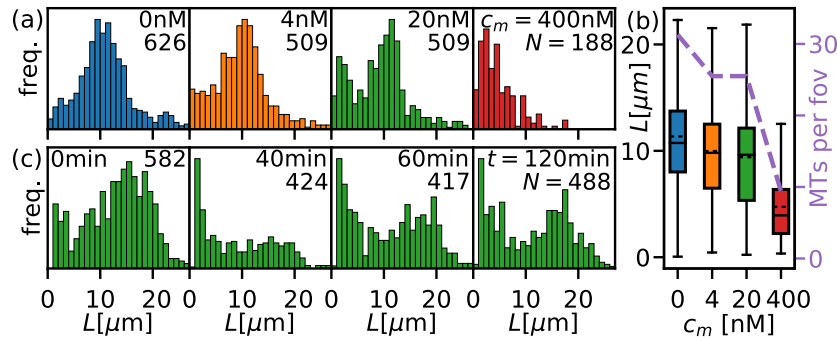
Figure II.4.: Experimental results. (a) Length distribution of MTs grown for 3 hours and subsequently incubated with various concentrations of Kip3 for one hour. The distribution is unimodal for 0 nM, 4 nM, and 400 nM Kip3; it is bimodal for 20 nM Kip3, indicating that length regulation is bistable. (b) Box plots for the MT length show that the median MT length decreases as the Kip3 concentration is increased (left axis). The dashed line (right axis) indicates the average number of MTs per field of view (fov). (c) Length distributions of MTs initially grown for 3 hours and subsequently incubated with 20 nM Kip3 for various amounts of time. Within an hour, a bistable distribution is established, and its shape is conserved as the incubation time is increased.

tion regime similar to the single-MT case, Fig. II.12. Here, all MTs jointly become short or long, and their average initial length determines which of these states is reached.

Because diffusion in a real system is fast only on short length scales, and large systems are not well-mixed, we decided to test the actual behavior directly by performing a set of *in vitro* experiments. We grew GMP-CPP stabilized MTs from a MT polymerization solution based on 2 μM tubulin at 27 °C (see Sec. A.6 in Appendix A for details). The resulting MTs had a length distribution similar to a Schulz distribution (202), and their median length could be influenced by varying the incubation time (1.5 or 3 hours). Subsequent to initial MT polymerization, different Kip3 concentrations were added to samples of the same polymerization solution and, as a control, no Kip3 was added to the final aliquot; all parts were incubated for another hour, so that MT polymerization from the remaining free tubulin and Kip3-induced depolymerization could occur simultaneously. The resultant MT length distributions in the samples were imaged as described in Sec. A.6 in Appendix A.

In the first experiment, MTs grown for 3 hours were incubated with 0, 4, 20, and 400 nM Kip3 for another hour. In the absence of Kip3 (0 nM), the length distribution of MTs peaked around 11 μm (Fig. II.4a and Fig. II.24). The presence of Kip3 reduced the median MT length (Fig. II.4b, box plots/left axis), and also decreased the number of MTs per field of view (Fig. II.4b, dashed line/right axis). The latter indicates that a number of MTs were completely depolymerized or shrank below the detection limit of our setup. Notably, at low and high Kip3 concentrations of 4 nM and 400 nM, the length distributions were unimodal with peaks around 11 μm and 2.5 μm (Fig. II.4a), respectively. This corresponds to the monostable regimes at low and high motor concentrations derived above, where polymerization and depolymerization, respectively, dominate and the final length is independent of the initial length.

In contrast, at a Kip3 concentration of 20 nM, the MT length distribution was qualitatively different: Here, two distinct populations of MTs (peaks around 2.5 μm and 11 μm) were observed,

resulting in a bimodal length distribution (Fig. II.4a). We could exclude that the short MTs observed in this experiment were additionally nucleated after the addition of Kip3, Fig. II.23. Furthermore, the two peaks are not transient. In contrast, a bimodal distribution is fully established within an hour, and the qualitative distribution remained intact until the end of our experiment, Fig. II.4c. The bimodal length distribution must therefore result from bistable length regulation: According to Fig. II.11 in Appendix A, MTs in a well-mixed many-filament system will jointly become short or long in the bistable regime, and their local average initial length distinguishes between these cases. However, diffusion of protein is fast only on short length scales, and slow in large systems, such as our experimental setup. In addition, the association of motors with MTs, on which they may remain for minutes or longer, significantly slows down diffusion in crowded environments, e.g., inside cells. The resulting separation of length scales of the small well-mixed range and the large system size may hence allow different regions of a system to develop independently. Given a broad initial distribution of MT lengths, the local average length of MTs in some regions is therefore in the domain of attraction of the steady state with long length, while in other regions MTs are attracted towards the short length. Hence, MTs in distant spatial regions evolve towards the different fixed points and domains with long and short filaments are formed, which coexist at stationarity. This interpretation is supported by the length distribution of MTs resulting from a solution of Kip3 and tubulin which is incubated for 1 hour in a shaker at the same conditions otherwise, Fig. II.22. Because constant mixing leads to a global well-mixed reservoir, the resulting length distribution is unimodal, confirming our expectations.

We then sought to obtain further information about the domains of attraction of the respective stationary states and the corresponding separatrix marking the boundary between these domains (Fig. II.21b). If the MT length distribution at which the length regulation process starts is short, MTs in all regions will be in the domain of attraction of the short stationary length. To test this prediction, we stopped MT growth after 1.5 hours and subsequently added the same amounts of Kip3 to the polymerization solution as before. The median MT length in the absence of Kip3 was significantly shorter (Fig. II.19b) than the corresponding value for MTs grown for 3 hours. We observed that the length distribution remained unimodal when Kip3 was added, irrespective of its concentration, Fig. II.19a. This indicates that, after 1.5 hours of initial MT polymerization, filament lengths still lie below the separatrix in Fig. II.19b. Taken together, our experimental findings qualitatively confirm our theoretical predictions, including the existence of a regime where MT length regulation by Kip3 gives rise to two populations of filaments with clearly distinct lengths.

Taking a broader perspective, we believe that – similar to the case considered here – effects of resource limitation are of relevance to other aspects of mitotic spindle formation and disassembly, and other processes in which protein availability in the cytosol constrains dynamic interactions.

A. Appendix: Calculations and additional experimental data

A.1. Brief review of TASEP/LK

The totally asymmetric simple exclusion process with Langmuir kinetics (TASEP/LK), on which our model presented in the main text is based, is schematically depicted in Fig. II.5. In the lattice bulk, the stochastic processes in TASEP/LK are identical to those of our model, cf. Fig. II.1b in the main text. In TASEP/LK, using the notation of Refs. (155, 156), the attachment rate ω_A is constant, i.e. one assumes that the motor reservoir is unlimited. The detachment rate in the lattice bulk is given by ω_D. Particles move to the next site a distance a apart at rate v. At the left end, which corresponds to the minus end of the MT, Fig. II.1b in the main text, particles enter the lattice at rate α if the first site is not occupied; at the right end (the plus end), particles leave the lattice at rate β. Note that unlike for the stochastic model in the main text, in TASEP/LK, particle detachment at the plus end preserves the lattice integrity, i.e., its length L remains constant.

For TASEP/LK, the density profile of particles on the lattice is well known. Depending on the parameters $K = \omega_A/\omega_D$, $\Omega_D = \omega_D L$, and the rates α and β, the profile can look very different. While we refer the reader to Ref. (156) for full details of the mathematical analysis, here we summarize the main aspects of TASEP/LK model which are of relevance for our study.

Identical to the main text, Eq. (II.3), the motor density in the lattice bulk in the stationary state follows from

$$\begin{aligned}
\partial_t \rho_i = v\left[\rho_{i-a}(1 - \rho_i) - \rho_i(1 - \rho_{i+a})\right] \\
+ \omega_A(1 - \rho_i) - \omega_D \rho_i = 0 \,,
\end{aligned} \tag{II.5}$$

where we have employed the mean field approximation $\langle n_i n_j \rangle \approx \langle n_i \rangle \langle n_j \rangle = \rho_i \rho_j$, and ρ_i is the average motor density at the site located at $i \in \{0, a, 2a, \dots, L\}$. The boundary conditions are
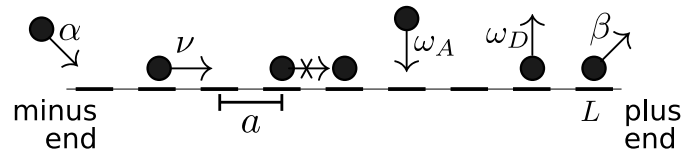
Figure II.5.: *The totally asymmetric simple exclusion process with Langmuir kinetics (TASEP/LK). Particles jump to the right at rate v, provided the next site is empty. They attach to the lattice at ω_A; in addition, particles may enter at the left end of the lattice end at α if the first site is unoccupied. Particles leave the lattice by exiting at the right end at rate β, or by detaching from any other site at ω_D.*

given by

$$0 = \partial_t \rho_0 = \alpha(1 - \rho_0) - \nu\rho_0(1 - \rho_a), \tag{II.6a}$$

at the minus end of the lattice, and

$$0 = \partial_t \rho_L = \nu\rho_{L-a}(1 - \rho_L) - \rho_L\beta \tag{II.6b}$$

at the plus end. Like in the main text, we perform the continuum limit for Eqs. (II.5) and (II.6) (156), and obtain [1]

$$a\nu\left[\partial_x\sigma(x) + \partial_x\ln|\sigma(x)|\right] = \omega_{\mathrm{D}}\frac{(K+1)^2}{K-1}, \tag{II.7}$$

where the density ρ and the "reduced density" σ are related as

$$\sigma = \frac{K+1}{K-1}(2\rho - 1) - 1 \ . \tag{II.8}$$

In the continuous description, the boundary conditions following from Eq. (II.6) are $\rho(0) = \alpha/\nu$, and $\rho(L) = 1 - \beta/\nu$.

Provided $K = \omega_{\mathrm{A}}/\omega_{\mathrm{D}} > 1$, the solutions of Eq. (II.7) can be obtained in terms of the different branches of the Lambert W function (156), which is defined as the inverse function of $f(x) = xe^x$. For the opposite case, $K < 1$, a solution can be obtained by exploiting the particle-hole symmetry of the TASEP/LK model: The model maps onto itself by changing the spatial coordinate $x \leftrightarrow L-x$ and the density $\rho \leftrightarrow 1 - \rho$, and simultaneously interchanging α and β, and ω_{A} and ω_{D} (156).

In terms of the two branches of the Lambert W function, W_0 and W_{-1}, the reduced density profile in case $K > 1$ can be written as (156)

$$\sigma_\alpha(x) = W_{-1}(-Y_\alpha(x)) \tag{II.9a}$$

and

$$\sigma_\beta = \begin{cases} W_0(Y_\beta(x)) \ , & \text{if } 0 \le \frac{\beta}{\nu} < 1 - \frac{\omega_{\mathrm{A}}}{\omega_{\mathrm{A}}+\omega_{\mathrm{D}}} \\ 0 \ , & \text{if } \frac{\beta}{\nu} = 1 - \frac{\omega_{\mathrm{A}}}{\omega_{\mathrm{A}}+\omega_{\mathrm{D}}} \\ W_0(-Y_\beta(x)) \ , & \text{if } 1 - \frac{\omega_{\mathrm{A}}}{\omega_{\mathrm{A}}+\omega_{\mathrm{D}}} < \frac{\beta}{\nu} < \frac{1}{2} \end{cases} \tag{II.9b}$$

with the function $Y(x)$ defined as

$$Y(x) = |\sigma(x_0)| \exp\left[\frac{\omega_{\mathrm{D}}}{\nu}\frac{(K+1)^2}{K-1}\frac{(x-x_0)}{a} + \sigma(x_0)\right] \ , \tag{II.10}$$

and Y_α and Y_β are the solutions in which the reduced density $\sigma(x_0)$ is evaluated at $x_0 = 0$, or $x_0 = L$, respectively.

---

[1]Note that here, unlike in Ref. (156), x runs from 0 to L.

In Ref. (156) it was shown that among others [2] there are three possible solutions for the actual density profile:

(i) The density profile $\rho(x)$ is given by $\rho_\alpha(x)$ along the whole lattice, and has a discontinuity at the plus end; this is called the low density (LD) phase, see Fig. II.8a.

(ii) The density profile $\rho(x)$ is given by $\rho_\beta(x)$ along the whole lattice, and has a discontinuity at the minus end; this is called the high density (HD) phase.

(iii) The density profile $\rho(x)$ is given by $\rho_\alpha(x)$ in the vicinity of the minus end, and $\rho_\beta(x)$ near the plus end. At position x_w, the density $\rho(x)$ increases discontinuously from $\rho_\alpha(x_w)$ to $\rho_\beta(x_w)$, and $\rho_\alpha(x_w) = 1 - \rho_\beta(x_w)$. x_w is called the domain wall (DW) position, and the resulting phase is termed the low density/high density (LD/HD) phase or shock phase (SP), see Fig. II.8b.

To find out which of the qualitatively different density profiles (i)–(iii) describes the physical behavior of TASEP/LK with specified parameters, a domain wall analysis has to be performed (23, 152, 203). This essentially amounts to consider a (virtual) DW merging the density functions ρ_α and ρ_β. The velocity of the DW can be calculated and depending on whether it is (i) positive, (ii) negative, or (iii) vanishes at a position in the lattice bulk, the density profile is given by (i)–(iii) described above.

Here we are interested in the case $\alpha = 0$, cf. Fig. II.1b in the main text. As discussed in detail in Refs. (156, 204), only two phases are possible in case $K > 1$: The LD, and the LD/HD phase. In order to distinguish between these profiles, the DW analysis discussed above suggests a simple test: If there is a location x_w on the lattice where $\rho_\alpha(x_w) + \rho_\beta(x_w) = 1$, a domain wall forms at x_w and the full density profile is given in terms of the LD/HD phase. If no such position x_w exists, the LD phase is established.

A.2. Full mean-field solution based on TASEP/LK

A.2.1. Reduction to a lattice of constant length

As discussed in the main text, Eqs. (II.2), the rate of change of MT length and the number of motors on it are given by

$$\partial_t L = (\gamma - \rho_+ \delta)a \,, \tag{II.11a}$$

$$\partial_t m = \omega_A (L/a - m) - \omega_D m - \rho_+ \delta \,, \tag{II.11b}$$

and ω_A and γ are given by Eqs. (II.1) in the main text. This set of equations was complemented by a third equation in the main text, Eq. (II.4), approximating the flux off the MT, $\rho_+ \delta$. In this Section, we will present a more refined theory which invokes an exact solution of Eq. (II.3) in the main text, and justifies the assumptions made in the main text in more detail.

---

[2] Here we leave out the Meissner phase found in Ref. (156) where the bulk behavior is independent of the rates at the boundaries, because we do not observe this phase at our conditions.

A. Appendix: Calculations and additional experimental data

In Eqs. (II.11), the dynamic quantities are L, m, and ρ_+, and ω_A and γ follow from these equations with Eqs. (II.1) in the main text. At stationarity, the fluctuations around L^* and m^* are small, i.e., $\Delta L/L^* \ll 1$, and $\Delta m/m^* \ll 1$. Moreover, the processes changing the length of the MT, or the number of motors on it, are slow compared to the hopping of a single motor. For instance, at a tubulin concentration of $c_T = 2\mu$M, even when all tubulin resources are available, the polymerization rate is $\gamma = 0.76\,s^{-1} \ll v = 6.35\,\mathrm{s}^{-1}$. Hence, although L and $\omega_A(m)$ are dynamic quantities, their values are *effectively constant*.

This suggests to reduce our model to an effective model with (exactly) constant attachment rate and (exactly) constant lattice length. Clearly, this is the TASEP/LK, discussed in Sec. A.1, see also Fig. II.5. Here, particles attach to the lattice at constant rate ω_A, independent of the availability of particles, and also the lattice length L is constant. This reduction promises to be a great simplification because TASEP/LK has been studied extensively. In particular, the density profile of particles in this effective model is well known (156), see Sec. A.1.

To ensure that the dynamic and the effective model lead to the same physical observables, we require that

- the TASEP/LK lattice length L equals the (*a priori* unknown) steady state MT length L^*, which is determined from the interplay of polymerization and motor-induced depolymerization dynamics,

- the TASEP/LK attachment rate ω_A equals the (*a priori* unkown) steady state attachment rate $\omega_A^* = \omega_A^0 (c_m - m^*/V)$ in the MT model,

- the TASEP/LK detachment rate at the plus end β equals the detachment rate from the MT at this site, δ.

Note that because the length of the lattice of TASEP/LK is constant, particle detachment at the plus end (at rate β) does not change L; in addition, no lattice elongation is possible, i.e. $\gamma_0 = 0$ for TASEP/LK.

We can verify the validity of this reduction by comparing the density profiles of motors on the MT with the corresponding profile of particles in TASEP/LK, as they are obtained from simulations. This is shown in Fig. II.6. The procedure of calculating the motor density $\rho(x)$ on a lattice of dynamic length is illustrated in Fig. II.6e: In order to obtain the density profile in the vicinity of the minus (plus) end of a MT, an ensemble of MTs is aligned along their minus (plus) ends before taking the average; the full density profile is then obtained by merging the two density profiles in the bulk such that the total length of the profile equals the average MT length. As Figs. II.6(a)–(d) show for two different sets of parameters, the density profile for the dynamic lattice obtained in this way is in excellent agreement with the corresponding density profiles of the effective TASEP/LK model on a lattice of constant length $L = L^*$ and attachment rate $\omega_A = \omega_A^*$.

A.2.2. Strategy to obtain the stationary state

With the reduction of the MT model to TASEP/LK, we can now proceed along the following lines:

(i) In the previous section, Sec. A.2.1, we have found that the MT model with dynamic lattice length and resource-limited attachment rate can be reduced to an effective model with constant length and constant attachment rate; the effective model is the TASEP/LK (156).
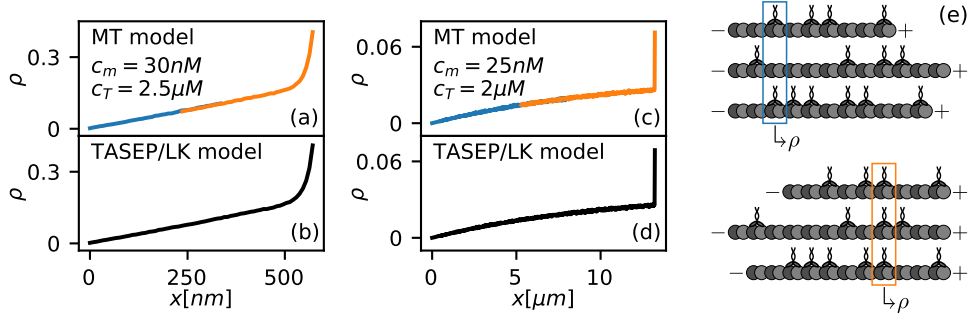
Figure II.6.: (a)–(d) Comparison of the occupation density on the MT lattice (top) with the corresponding density of TASEP/LK (bottom). For parts (a) and (c), the concentrations are chosen as in Figs. II.2a–II.2b in the main text, for parts (b) and (d), parameters derive as explained in Sec. A.2.1. (e) An ensemble of MTs with a varying length can either be aligned at their minus (top panel), or their plus (bottom panel) ends. The motor occupation density is then obtained by taking the ensemble average, and the full density profile results by merging both averages in the lattice bulk, such that the total length of the profile equals the average lattice length.

(ii) For TASEP/LK we know, cf. Sec. A.1 and Ref. (155, 156), that there are different phases which have their characteristic particle density profiles. *Assuming* that the system is in one of these phases, we obtain the motor density close to the plus end. Subsequently, mass conservation can be used to obtain an expression for the density ρ_+. With the ensuing equation and Eqs. (II.11), the steady state quantities L^*, m^*, and ρ_+^* can be computed.

(iii) Having explicit numerical values for these quantities, it is possible to determine the phase of TASEP/LK with $L = L^*$ and $\omega_A = \omega_A(m^*)$. This phase should be the same as the phase which we originally assumed (without specifying parameters) in step (ii). Hence, comparing the *assumed* and the *actual* phase provides a self-consistency check. Given this test is passed, L^* and m^* describe the stationary state.

A.2.3. Case $K > 1$

We will first concentrate on the case $K > 1$, i.e. the case where the motor attachment rate at stationarity exceeds the rate of motor detachment, $\omega_A^* > \omega_D$. Because $\alpha = 0$, we know from TASEP/LK (156, 204) that two phases are in principle possible in principle: 1. The LD/HD phase (shock phase), in which the motor densities at the minus and plus end are low and high, respectively, and a domain wall (DW) connects these densities in the MT bulk, and 2. the LD phase, where the density is small along the complete lattice, except for a peak ("spike") at the plus end.

A.2.3.1. Low density/high density (LD/HD) phase

The simplest case is the LD/HD phase, where the MT becomes stationary at length $L^*_{\text{LD/HD}}$ with $m^*_{\text{LD/HD}}$ motors on it. Assuming such a steady state does not imply its existence. Hence, as discussed above, after having found a stationary state, it has to be checked for self-consistency.
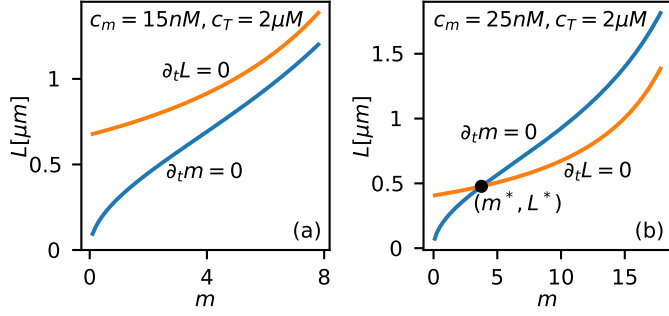
Figure II.7.: Nullclines of the vector field $(\partial_t m, \partial_t L)$ for the case $K^* > 1$. As opposed to Fig. II.21, here the full mean-field solution for the motor flux off the MT, Eq. (II.17), was used. Along the nullclines, L and m become stationary separately. (a) For small motor concentration, $c_m = 15$nM, we find that L and m do not become stationary simultaneously. Hence, no LD solution with $K^* > 1$ exists for this concentration. (b) For higher motor concentrations, here $c_m = 25$nM, both nullclines intersect, i.e. the vector field has a fixed point at (m^*, L^*).

In the LD/HD phase of TASEP/LK, the motor density approaches its value at the plus end continuously, see Fig. II.8b. Therefore, because ρ varies only slowly with x, the density at the penultimate site (almost) equals the density at the plus end, $\rho_{L-a} \approx \rho_+$. Because of the conservation of the number of motors (mass conservation), the motor current to the tip equals the flux off the MT. We obtain

$$v\rho_{L-a}(1 - \rho_+) \approx \rho_+\beta \,, \qquad (\text{II.12})$$

and hence

$$\rho_{+,\text{LD/HD}} \approx 1 - \beta/v \,. \qquad (\text{II.13})$$

Invoking the correspondence between TASEP/LK and the MT at stationarity, cf. Sec. A.2.1, this equation can be used together with Eqs. (II.11a) to obtain

$$L^*_{\text{HD}} = aV\left[c_T - \frac{\delta(1 - \delta/v)}{\gamma_0}\right] \,. \qquad (\text{II.14})$$

In order to be a valid description, L^*_{HD} obtained in this way should be positive. However, with the model parameters derived in Sec. A.3, we find that $L^*_{\text{HD}} > 0$ only for very large tubulin concentrations, $c_T > 4$ μM, well above the concentration chosen in our *in vitro* experiments. We conclude that the LD/HD phase plays no role for MT length regulation by kinesin motors at our conditions.

A.2.3.2. Low density (LD) phase

The other phase which is possible for $K > 1$ and $\alpha = 0$ is the low density phase. Here, the motor density remains small along the complete lattice, except for the immediate vicinity of the plus end, where it peaks ("spike"), see Fig. II.8a.

In the LD phase, the particle density $\rho(x)$ of TASEP/LK is given by Eqs. (II.9a) and (II.8).

Because the discontinuity at the plus end extends only over very few lattice sites, the density at the foot of the spike (which we denote ρ_{L-a}, like in the main text) can be approximated by evaluating the density at position L. We therefore obtain

$$
\begin{aligned}
\rho_{L-a} &\approx \rho_\alpha(L) \\
&= \frac{1}{2}\left\{\frac{K-1}{K+1}\big[W_{-1}(-Y_\alpha(L)) + 1\big] + 1\right\}.
\end{aligned}
\tag{II.15}
$$

As described in the previous paragraph, the motor current is a slowly varying function of x; this is because attachment and detachment are slow compared to the hopping of motors, $\omega_A, \omega_D \ll v$. Thus, even though the density is discontinuous at the plus end, the motor current is continuous, and hence the current to the tip equals the current off the tip, which implies

$$
v\rho_{L-2a}[1 - \rho_{L-a}] \approx v\rho_{L-a}[1 - \rho_{L-a}] \approx \rho_+\beta.
\tag{II.16}
$$

Once again invoking the correspondence between TASEP/LK and the MT at stationarity, this results in the expression

$$
\rho_+^*\delta \approx v\rho_\alpha(L)\big[1 - \rho_\alpha(L)\big]\Big|_{L=L^*,\omega_A=\omega_A^*}.
\tag{II.17}
$$

Equation (II.17), together with Eqs. (II.11) now fully determine all dynamic quantities at stationarity, L^*, m^*, and ρ_+^*. In particular, they define the vector field $(\partial_t m, \partial_t L)$ which we also introduced in the main text, employing a Taylor series solution of $\rho_+\delta$.

Nonlinear systems of this kind are best analyzed by flow profiles (vector fields) in the phase plane (m, L). The solution of the dynamic equations for m and L can directly be read of as trajectories following stream lines (205). An example is shown in Fig. II.21 for the approximate mean-field solution derived in the main text. For the refined solution of the motor flux off the MT, Eq. (II.17), we have depicted the nullclines of the vector field $(\partial_t m, \partial_t L)$ in Fig. II.7. Along the nullclines, the components of the vector field vanish separately, $\partial_t L = 0$ and $\partial_t m = 0$, such that the stationary state, i.e. the fixed point of the vector field, is given by the intersection point of the nullclines. For an exemplary motor concentration $c_m = 15\text{nM}$ at $c_T = 2\mu\text{M}$, which is depicted in Fig. II.7a, no such fixed point exists. This implies that the MT does not have a stationary state in the LD phase for these concentrations. By contrast, for an increased motor concentration $c_m = 25\text{nM}$, Fig. II.7b, both nullclines intersect at (m^*, L^*). Hence, a MT with those concentrations may *possibly* become stationary at m^* and L^* in the LD phase.

However, in order to find out whether the MT dynamics will *actually* become stationary at this point, we have to check whether it has been obtained in a self-consistent way. In particular, this implies that two conditions have to be met:

(i) In the derivation of Eq. (II.17) we have assumed $K > 1$. Hence, the stationary state described by L^* and m^* should also guarantee $K^* > 1$.

(ii) Furthermore, we have assumed that the TASEP/LK with the (unknown) parameters L and ω_A is in the LD phase. Having obtained numerical values, $L = L^*$ and $\omega_A = \omega_A(m^*)$, we can now verify whether TASEP/LK with these parameters is actually in the LD phase.

A. Appendix: Calculations and additional experimental data

Condition (i) imposes a constraint on the concentration of free, i.e. unbound, motors at stationarity, $c_f^* = c_m - m^*/V$:

$$K^* \overset{!}{>} 1 \Leftrightarrow c_f^* \overset{!}{>} \frac{\omega_D}{\omega_A^0} \approx 7\text{nM}. \tag{II.18}$$

Hence, any steady state which yields a number of motors on the MT, m^*, which is so large that the free motor concentration falls below 7nM, fails to be self-consistent, and must therefore be rejected.

In order to verify the self-consistency condition (ii), we have to analyze in which phase the TASEP/LK with $L = L^*$ and $\omega_A = \omega_A(m^*)$ actually is. It is important to understand that the *assumption* of being in the LD phase which lead to Eq. (II.17) does not guarantee that the *actual dynamics* of the TASEP/LK is given in terms of this phase! In principle, the phase diagram of TASEP/LK is by now a text book result (156), and thus, given specific motor and tubulin concentrations, and hence specific quantities L^* and ω_A^*, we could look up the behavior in the phase diagram. However, here we are interested in a general solution. This implies, in analogy with the analysis for TASEP/LK, Sec. A.1, that we have to closely look at the density functions matching the boundary conditions at the minus and plus end, $\rho_\alpha(x)$, and $\rho_\beta(x)$, respectively. We have pointed out in Sec. A.1 that if these functions add to 1 at some position x_w on the lattice, a domain wall establishes at this point; the resulting density profile would then indicate a LD/HD phase. Hence, we have to ensure that there is *no such position x_w* on the lattice where the densities $\rho_\alpha(x_w)$ and $\rho_\beta(x_w)$ would add to 1. The procedure of determining whether or whether not a domain wall establishes is illustrated in Fig. II.8 for a lattice of (hypothetical) length $L = 100a$. The function $\rho_\alpha(x)$ is a monotonously increasing function. Likewise, provided that the Langmuir density $K/(K + 1)$ is smaller than the tip density $1 - \beta/\nu$ which is implied by our simulation results as long as the tubulin concentration $c_T \lesssim 3\mu\text{M}$, the density $\rho_\beta(x)$ is also increasing; this implies that $1 - \rho_\beta(x)$ decreases monotonically with x. As $0 = \rho_\alpha(0) < 1 - \rho_\beta(0)$, a condition for the existence of a domain wall at $0 < x_w < L$ is hence $\rho_\alpha(L) > 1 - \rho_\beta(L) = \beta/\nu$. Because the condition for the LD phase is that *no* domain wall exists, a necessary and sufficient condition for the LD phase is therefore that

$$\rho_\alpha(L) \overset{!}{<} \beta/\nu. \tag{II.19}$$

Provided this condition is met we have arrived at a self-consistent stationary state.

With the numerical solutions for L^* and ω_A^* obtained from Eqs. (II.11) and (II.17), a numerical test of Eqs. (II.18) and (II.19) can be performed. In this way, the concentration regime in which the LD phase for $K^* > 1$ yields a physically reasonably, and self-consistent solution, can be constrained, see Fig. II.3e in the main text.

A.2.4. Case $K < 1$

In the previous section, Sec. A.2.3, we have considered the case of strong motor attachment. Here, we will analyze the opposite case where the motor concentration is either so small or so strongly depleted in the cytosol that at stationarity $\omega_A^* < \omega_D$. In the effective model, the TASEP/LK, to which we have reduced the length regulation model of a MT, see Sec. A.2.1, this corresponds to the case $K < 1$. For this case, the density profiles of particles on the lattice are most easily obtained by using the particle-hole symmetry of TASEP/LK: Here, instead of considering the motion of motor
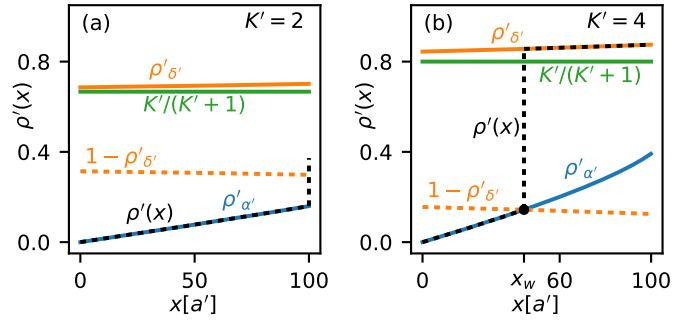
Figure II.8.: *Construction of the full density profile of TASEP/LK, and distinction between the LD, and LD/HD phase. Shown are the density functions $\rho_\alpha(x)$ and $\rho_\beta(x)$ for a (hypothetical) lattice length $L = 100a$, for two different values of K. In both cases, the β branch of the density profile lies above the Langmuir density $K/(K + 1)$, which implies that the density function $\rho_\beta(x)$ increases monotonically (156). In part (a), which shows an exemplary profile of the LD phase, at no position along the lattice the density functions ρ_α and ρ_β add to 1, i.e., ρ_α and $1 - \rho_\beta$ do not intersect. This implies that no domain wall forms at these conditions. The full density profile $\rho(x)$ for this case is therefore identical to the branch $\rho_\alpha(x)$, and the density shows a discontinuity at the plus end, such that $\rho_\alpha(L)(1 - \rho_\alpha(L)) = \rho_+\beta$. For the conditions shown in part (b), exemplary for the LD/HD phase, the behavior is different: Here, a DW is localized at position x_w, where $\rho_\alpha(x_w) + \rho_\beta(x_w) = 1$. Therefore the full density profile is given by $\rho_\alpha(x)$ for $x < x_w$ and $\rho_\beta(x)$ for $x > x_w$, as indicated by the black dotted line.*
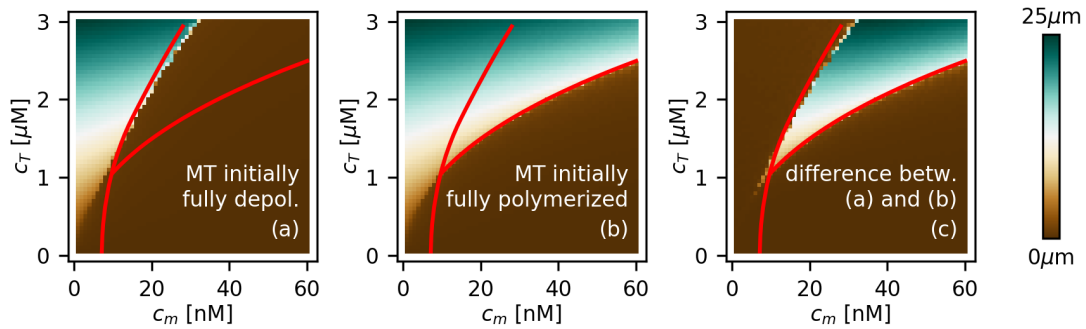
Figure II.9.: *Parameter scan of the motor and tubulin concentrations for a lattice which is initially short, part (a), or long (b). The color code indicates the stationary MT length, cf. also Fig. II.3a–II.3b in the main text. Red lines show the phase transition lines obtained from the full mean-field theory, Sec. A.2. Part (c) shows the difference of the first two panels, and reveals that the theoretical phase transition lines indeed constrain the bistable regime, see also Fig. II.3e in the main text.*

particles to the right, we may look at the motion of holes, i.e. lattice sites with *no* motors on them, moving to the left (156). In this picture, particle attachment corresponds to hole detachment and motor detachment to hole attachment. As a consequence, the concentration-limited process is *detachment* of holes. Having arrived at the left lattice end, holes exit the lattice at the same rate as particles enter at this site; likewise hole injection at the plus end corresponds to motor detachment from this site.

In conclusion, denoting the hole parameters and coordinates with a bar, we therefore employ the following correspondence of TASEP/LK and the dynamic MT at $K < 1$:

$$\begin{aligned}
\overline{L} &= L = L^*, \quad \overline{x} = \overline{L} - x, \quad \overline{\rho} = 1 - \rho, \\
\overline{v} &= v, \quad \overline{\alpha} = \beta = \delta, \quad \overline{\delta} = \alpha = 0, \\
\overline{\omega_A} &= \omega_D, \quad \overline{\omega_D} = \omega_A = \omega_A^* = \omega_A^0 (c_m - m^*/V) \,.
\end{aligned} \tag{II.20}$$

With this symmetry mapping, we can now proceed along the same lines as before. In Sec. A.2.3 we concluded that in the specific case $\alpha = 0$ at $K > 1$ two phases, the LD and LD/HD phase are possible. Similarly, for $K < 1$ where $\alpha = 0$ implies $\overline{\delta} = 0$ in the hole picture, we find that only two phases are possible which we will call low hole density/high hole density (LhD/HhD) phase, and low hole density (LhD) phase in the following. For the former, the hole density is small around the injection site of holes (i.e., at the MT plus end), and a DW in the lattice bulk connects this density to the high hole density at the opposite end (the minus end). In terms of the particle density, this implies a very similar density profile as for the LD/HD phase, Sec. A.2.3.1.

For the other phase which is possible in this case, the high hole density (HhD) phase, the hole density is high (i.e., the motor density is small) along the complete MT, except for a small boundary layer at the hole injection (i.e., the motor exit) site.

A.2.4.1. Low hole density/high hole density (LhD/HhD) phase

In the first case, where the hole density profile on the lattice is low at the injection site and high at the other end, and a DW separates these regions on the lattice, we can directly use the results of Sec. A.2.3.1: Here, we made use of the fact that if a domain wall forms in the lattice bulk, the density is continuous at both ends, which lead to an equation for the motor density at the plus end, Eq. (II.13). Since the same is true for the LhD/HhD phase, we find that the stationary state length is also given by Eq. (II.14). However, since we concluded earlier that the tubulin concentration would have to exceed 4μM such that this steady state length would be positive, we find that also in the case of weak motor attachment, $K^* < 1$, no stationary state showing a domain wall will be observed for conditions of our *in vitro* experiments.

A.2.4.2. High hole density (HhD) phase

The only remaining phase is characterized by a high hole density (i.e., low motor density) along the complete MT. Similar to the LD phase, Sec. A.2.3.2, the hole density is discontinuous at the plus end of the lattice, where holes are injected, i.e., at $\overline{x} = 0$.

In full analogy with the case $K > 1$, from the notion that the flux of holes (and thus also the flux of motors) is constant on short length scales, we now conclude that the motor flux off the MT

equals the hole flux onto the lattice, which equals the hole current a small distance away from the tip. In accordance with Eq. (II.17), this yields

$$\rho_+^* \delta = \overline{\nu} \overline{\rho}_{\overline{\delta}}(0)\left[1 - \overline{\rho}_{\overline{\delta}}(0)\right]\Big|_{\overline{L}=L^*, \overline{\omega}_{\mathrm{D}}=\omega_{\mathrm{A}}^*, \overline{\delta}=\alpha=0, \overline{\nu}=\nu} . \tag{II.21}$$

In the same way as discussed in Sec. A.2.3.2, Eq. (II.21) together with Eqs. (II.11) defines a vector field $(\partial_t m, \partial_t L)$, whose fixed points define the stationary quantities L^* and m^*.

These fixed points have to be checked for self-consistency. In analogy with Sec. A.2.3.2, this amounts to ensure that no position $\overline{x_w}$ exists where the two density solutions matching the respective boundary conditions, $\overline{\rho}_{\overline{\alpha}}(x)$ and $\overline{\rho}_{\overline{\delta}}(x)$, would add to 1, i.e. $\overline{\rho}_{\overline{\alpha}}(\overline{x_w}) = 1 - \overline{\rho}_{\overline{\delta}}(\overline{x_w})$. Because we know that $1 - \overline{\rho}_{\overline{\delta}}(\overline{L}) = \rho_\alpha(0) = 0 < \overline{\rho}_{\overline{\alpha}}(\overline{L})$, it is sufficient to compare the hole density at the site where they are injected, i.e. at the MT's plus end: If $1 - \overline{\rho}_{\overline{\delta}}(0) < \overline{\rho}_{\overline{\alpha}}(\overline{L}) = 1 - [1 - \rho_\beta(L)] = \beta/\nu$, no domain wall can localize on the lattice. In this case, the solutions obtained from Eqs. (II.21) and (II.11) are self-consistent.

A.2.5. Comparison with simulations, and the phase diagram/stability diagram

Having completed the mean-field analysis, we are now in a position to compare these analytical results with simulation data. Fig. II.3d in the main text shows the MT length as a function of the motor concentration c_m at $c_T = 2\mu$M. Mean-field theory and simulations show excellent agreement. Starting at low motor density, the stationary length is long (i.e., polymerization dominates), and $K^* < 1$. At high motor densities, the steady state length is short (depolymerization dominates) with $K^* > 1$. In the bistable regime for intermediate concentrations, a third solution exists which connects the two branches. We have discussed in the main text that this solution is unstable, and we can obtain its numerical value from the full mean-field theory as a solution of the HhD phase in case $K^* < 1$, Sec. A.2.4.2.

We can use the self-consistency conditions together with the steady state solutions obtained in the previous sections to summarize the domains in which $K^* > 1$ and $K^* < 1$, respectively, see Fig. II.3e in the main text. As expected from simulations, the two regimes overlap; in the overlapping part, length regulation is bistable. with simulation data, Figs. II.3a and II.3b in the main text, reveals that the steady state MT length obtained in simulations starting from a short and long length, respectively, changes discontinuously at the respective transition lines; this is because the phase transition lines describe the onset (and offset) of bistability. This is also illustrated in Fig. II.9c which shows the difference of L^* obtained in simulations starting from long, and short length, respectively.

In conclusion, the mean-field theory developed in this Section is in excellent agreement with simulation data.

A.3. Estimation of the parameters

We are interested in a theoretical description of the motion of the molecular motor Kip3 on MTs. For many of the motility parameters, accurate measurements exist which allow us to assign nu-

quantity	symbol	value	reference
hopping rate	v	6.35 s^{-1}	(21)
MT lattice spacing	a	8.4nm	(51)
detachment rate	ω_D	$4.9 \cdot 10^{-3} \text{s}^{-1}$	(21)
attachment rate per site	ω_A^0	$6.7 \cdot 10^{-4} \text{nM}^{-1}\text{s}^{-1}$	(21)
polymerization rate	γ_0	$0.38 \mu\text{M}^{-1}\text{s}^{-1}$	(49, 200)
depolymerization rate	δ	2.3s^{-1}	(21)
volume avail. per protofil.	V	$1.66\mu\text{m}^3$	estimated

Table II.1.: Overview of the model parameters, as obtained in Sec. A.3

merical values to most parameters. We have summarized all parameters in Table. II.1 and will show how to obtain their values in this Section.

Kip3 motors move at $3.2\mu\text{m}/$ min (21). In units of the distance between two tubulin dimers $a = 8.4\text{nm}$ (51), this gives rise to the hopping rate to the neighboring lattice site, $v = 6.35$ sites/s.

Kip3 runs on the MT for $11\mu\text{m}$ (21) at this speed, i.e., their dwell time is 206 s. Taking the inverse, this yields the detachment rate $\omega_D = 4.9 \cdot 10^{-3} \text{ s}^{-1}$. The run length might be an underestimate, but the specific value of ω_D is relatively unimportant, as long as it is small.

In order to obtain the spontaneous polymerization rate of MTs, we consider the polymerization speed of stabilized MTs (these are MTs in which the GTP analogue GMP-CPP is used to grow MTs in order to avoid dynamic instability) which we have used in our *in vitro* experiments (49, 200). Hyman et al. (49) measured the speed of MT growth, and find the value $0.19\mu\text{m min}^{-1} \mu\text{M}^{-1}$, corresponding to a dimer polymerization rate of $\gamma_0 = 0.38\mu\text{M}^{-1}s^{-1}$ on each protofilament. The same value was obtained by Brouhard et al. (200). Here, we neglect (slow) spontaneous MT depolymerization (which was measured to be as low as $0.23\mu\text{m}/h$ (49), which corresponds to a spontaneous tubulin loss rate of $7.6 \cdot 10^{-3} \text{ s}^{-1}$ on each protofilament; another study (200) indicates a slightly higher tubulin loss rate per protofilament of $3.8 \cdot 10^{-2} \text{ s}^{-1}$, which is still small). A recent study has indicated that the tubulin exchange rate at the MT tip is indeed much faster than reported previously (70). However, the net spontaneous polymerization in this study, i.e. the difference of spontaneous polymerization and depolymerization is comparable to the values reported by Hyman et al. (49) and Brouhard et al. (200). Since we are only interested in the net values, the estimates of these studies therefore remain valid for our purposes.

The attachment rate of Kip3 motors to a binding site on a MT can be obtained from the motor landing rate measured per concentration, per time, and per length, for which Varga et al. obtained the value $24\text{nM}^{-1}\text{min}^{-1}\mu\text{m}^{-1}$ (21). The interpretation of this value is not straightforward for two reasons: Firstly, the landing rate critically depends on the number of motors which are already attached to the MT, and even at smalls motor concentration it may be significantly depleted due to a reduced availability of binding sites (30). Secondly, it is not clear how to convert a per-μm attachment rate to a per-site attachment rate: The measurement of Varga et al. (21) was done in a TIRF setup, where motors can probably bind to and walk on roughly 5 protofilaments (the "upper half") (109). We decided to use the resulting $5 \cdot 1000/8.4$ binding sites as the conversion factor between the per-μm and the per-site attachment rate. This results in the per-site attachment rate $\omega_A^0 = 6.7 \cdot 10^{-4}\text{nM}^{-1}\text{s}^{-1}$.

For the depolymerization process, we note that the mechanism of Kip3 induced MT depolymerization is not fully understood. However, we can obtain a lower bound for δ from the MT depolymerization speed at high kinesin concentration, which is ~ 1800 dimers/min (counting all protofilaments) (21). Therefore, the lower bound for the dimer depolymerization rate per protofilament is $\delta \approx 2.3$ s^{-1}.

The volume V from which protein can bind to the MT, i.e. the "basin" of a MT, is difficult to measure directly. We find in experiments that for MTs grown for 1.5 or 3 hours, between 35% and 40% of all tubulin is incorporated into the MTs, see Fig. II.20. At these times of incubations, MTs were on average 4.8μm and 10.8μm long, respectively, Fig. II.24. This implies that between $1,600$ and $3,200$ tubulin dimers are available for each protofilament [3]. Here, we are mostly interested in a rough estimate of the effective volume. Therefore we chose V in a way convenient for our simulations, such that a tubulin concentration of 2μM, typical for experiments, corresponds to 2,000 tubulin heterodimers available per protofilament. The resulting effective volume per protofilament is $V = 1.66\mu$m^3. We also verified that the particular choice of V plays no essential role for the phenomena, see Sec. A.4 and Figs. II.13–II.18.

A.4. Robustness of the parameters δ and V

Here we test our model for robustness against variations of its parameters. In particular, the values of the depolymerization rate δ and the volume available to each protofilament, V, have quite significant uncertainties. We have varied these parameters in Figs. II.13–II.18. These Figures show a parameter scan of the motor and tubulin concentrations, starting from a short, or long length, see also Figs. II.3a–II.3b in the main text. In particular, parts (c) of these Figures shows the difference of the simulation results obtained in panels (a) and (b), and hence indicate the concentration regimes in which length regulation is bistable.

We find that the precise value of δ, of which 2.3 s^{-1} is a lower bound, has no effect on the resulting stability diagram (phase diagram), when its value is increased threefold. In contrast, the volume per protofilament V, has a mild effect: When it is increased, the region in which MT length regulation is bistable, i.e. where the MT length may assume one of two stationary states, becomes larger. However, the general qualitative behavior remains unaltered.

The observation that the concentration regime for bistable length regulation becomes smaller for smaller basin volume V suggests an additional and alternative interpretation why the MT length distribution is unimodal for MTs grown for 1.5 hours only, and bimodal for MTs grown for 3 hours, see the main text and Figs. II.19a and II.4a. If, for any reason, the MT density in solution was larger for the shorter set of experiments, i.e., the volume available for each MT was smaller, the expected concentration regime in which MT length is bistable would also have been smaller. Then, it is in principle possible, that the relatively coarse sampling of length distributions at motor concentrations 0 nM, 4 nM, 20 nM, and 400 nM, has completely misses the bistable domain. In fact, the number of MTs counted per channel was larger for the set of experiments where MTs had been grown for 1.5 hours before addition of Kip3, Fig. II.19b, than for the 3 hours experiments, Fig. II.4b. This could indicate a higher MT density in solution, but could also be

---

[3]The large deviation of these numbers reflects that the length distributions of pre-grown MTs can be very different, even if they are grown for the same time.
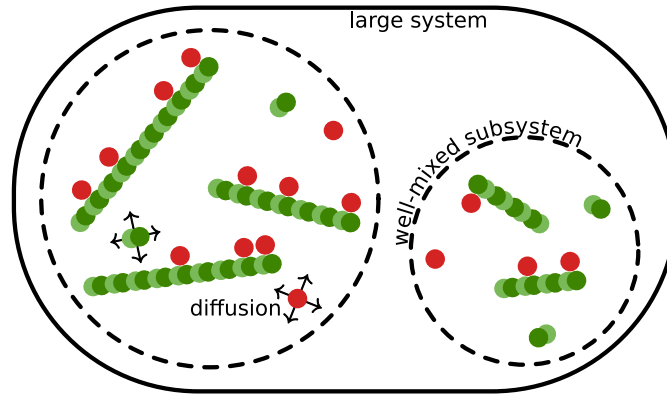
Figure II.10.: A large system with many MTs which share common pools of resources. Tubulin and molecular motors can be exchanged between the MTs via diffusion. Here, the spatial arrangement of MTs becomes important: Diffusion can lead to quick exchange of resources on a local scale while it is slow on long length scales. Hence, we may decompose the large system into smaller parts: Within these subsystems, resources are well-mixed, whereas two subsystem behave independently.

the result of fluctuations of the antibody density in the channels. At present, we are unable to distinguish between these two interpretations. Both of them are possible within our theoretical analysis. Future studies will help to distinguish between them, and will enable us to more closely investigate the role of the volume available to each MT.

A.5. Many MTs with shared reservoirs

So far, we have considered a model with only a single MT which has exclusive access to a reservoir of protein. However, inside a cell, as well as in our *in vitro* experiments, many MTs compete for a pool of tubulin dimers and molecular motors which is shared between all MTs. Fig. II.10 shows such a system schematically, and it illustrates the additional complexity which arises in such a system: While the motion of motors along MTs happens in a directed fashion, protein exchange between the filaments is only possible via diffusion. Already for a single MT, the consideration of diffusion significantly complicates a theoretical treatment (174). With many MTs in a system, diffusion furthermore leads to an additional spatial component, which eventually demands that the three-dimensional arrangement of the MTs in the system is specified. A model like this is highly interesting and can lead to emergent phenomena (26, 206), but it is far beyond the scope of this work.

Instead, here we want to focus on a simplified model, making use of a separation of length scales. On short length scales, diffusion is fast, so that on these scales, the system can be assumed to be well-mixed: There, all components are shared infinitely fast. In contrast, on longer length scales, diffusion is slow, so that distant MTs develop independent of another. This suggests to decompose our large system into smaller independent, well-mixed subsystems, see Fig. II.10: Inside a subsystem, diffusion is assumed to be infinitely fast, whereas no resource exchange takes place between subsystems. We will later argue the implications of this kind of separation, and indicate how our results can be connected to an *in vitro* or *in vivo* system.
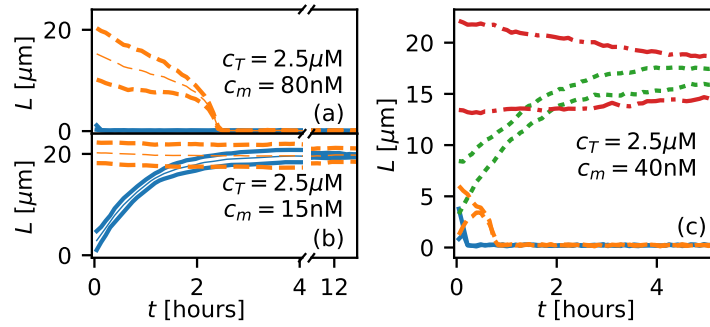
Figure II.11.: Simulation runs of a system of two MTs sharing a common pool of resources. Different colors represent different simulation runs, whereas a common color is used for the two MTs of a specific run. In parts (a)–(b), concentrations are chosen such that the dynamics are in the monostable regime. Even if the individual length (thick lines) of the two lattices is very different initially, they approach the same value at the stationary state. Hereby, equilibration is faster for the average length (thin lines) than for the length of individual filaments. Because the dynamics are monostable, the MTs in all simulation runs evolve towards a single stationary length which may be (a) short, or (b) long. Panel (c) shows trajectories for concentrations in the bistable regime. Here, both MTs of each simulation run approach the same steady state; the joint stationary length may be either short or long. Therefore, also a two-MT system shows bistability. Which of these stationary states is reached depends on the initial average length of the MTs.

A.5.1. Shared reservoirs with infinitely fast diffusion

Let us first focus on the case of several MTs in a small subsystem which is assumed to be well-mixed. This is the opposite limit compared to the model of a single, isolated MT, considered in the main text. More specifically, we consider the case of two MTs which share a common pool of resources which are exchanged between filaments infinitely fast. To compare with the original model, Fig. II.1b in the main text, we have chosen all parameters of the many-MT model equal to those of the single-MT model, and the volume of the system is doubled, such that the effective volume available per MT remains the same. Figure II.11 shows trajectories of the length of the two filaments at different conditions. For two sets of concentrations, Figs. II.11a–II.11b reveal that the length of both MTs assumes a common value relatively quickly. At these conditions, the stationary state is reached independent of the initial MT lengths. For the concentrations shown in these Figures, the dynamics are therefore monostable.

In contrast, for the concentrations used in Fig. II.11c, length regulation is bistable. Here, we find that the length of both MTs of a single simulation run still approach the same value. However, depending on the initial conditions, this length may be either short, or long. In particular, our simulation results indicate that when the average initial length of the two MTs is relatively short, it is likely that both MTs will evolve towards the fixed point with short length. By contrast, for initially (on average) long MTs, the long length will be reached. We conclude that bistability is found also when two (or more) MTs share a common pool of resources infinitely fast, but that all MTs in a well-mixed system of this kind approach the same stationary length.

Let us provide a theoretical argument why, even in the case of bistability, all MTs in the system
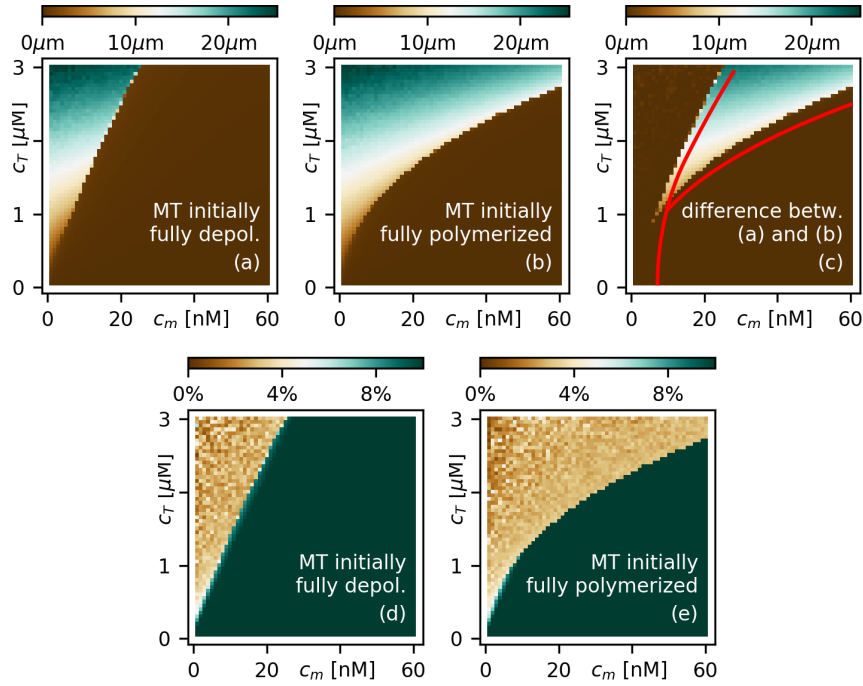
Figure II.12.: *Scan through motor and tubulin concentrations for a system of two MTs sharing a common pool of resources. Simulation results show the MT length starting from an initially (a) short and (b) long lattice. Part (c) shows the difference of the steady state length obtained in this way, and compares the resulting bistable regime with the results obtained theoretically for the single-MT model (red line). (d)–(e) show the relative standard deviation of the length of the two MTs, averaged over time, see Eq. (II.24). In the regime where MT are not completely depolymerized at stationarity (i.e., in the North West part of the Figure), the relative deviation remains small. In the South East region, MTs are very short; although the relative deviation is large here, the absolute standard deviation of both MT lengths is therefore small. This proves that the length of both MTs is very similar.*

share the same length. The balance equations, describing the rate of change of MT length and the number of motors on it, Eqs. (II.2) in the main text, can be straightforwardly generalized to many MTs:

$$\partial_t L^i = (\gamma^i - \rho_+^i \delta)a \, , \tag{II.22a}$$

$$\partial_t m^i = -\omega_D m^i + \omega_A^i (L^i/a - m^i) - \rho_+^i \delta \, , \tag{II.22b}$$

where the superscript i indicates that these equations apply to all of the N MTs in the system. Assuming that components in the cytosol are instantaneously available for any MT, the polymerization rate γ^i, as well as the attachment rate of motors to the MT, ω_A^i, depend only on the *global* availability of protein:

$$\gamma^i = \gamma = \gamma^0 \Big[c_T - \sum_i L^i/(aV) \Big] \, , \tag{II.23a}$$

$$\omega_A^i = \omega_A = \omega_A^0 \Big(c_m - \sum_i m^i/V \Big) \, . \tag{II.23b}$$

These equations imply that when, e.g., a tubulin dimer attaches to any of the N MTs and therefore elongates it, this will have the same immediate effect on the polymerization rate of all MTs. To explore the consequences of infinitely fast resource sharing, let us consider the rate of change of the length of a MT, Eq. (II.22a). With Eqs. (II.23), we find that γ^i is equal for all MTs, such that in the stationary state, when $\partial_t L^i = 0$, also the plus end density must be the same for all lattices, $\rho_+^i = \rho_+$. ρ_+ is determined from the balance of currents: The bulk current to the tip equals the motor flux from the tip. We concluded in Sec. A.2 that for relatively small motor concentrations, as considered in this work, the motor density remains small along the complete MT. From Ref. (156) we know that for this case both the motor density and their current increase with distance from the minus end. The lattice therefore acts as an antenna, and the longer it is the more motors it can attract. As a consequence, the density of motors at the tip is monotonously increasing with MT length. With Eq. (II.22a) we therefore obtain that the MT length is equal for all MT in the system, $L^i = L$.

In order to examine how the concentration regime in which the system behaves bistable is modulated in a two-MT system compared to a single MT, we have performed a scan through motor and tubulin concentrations analogous to the single-MT model (Fig. II.3a–II.3b in the main text). The resulting diagrams are shown in Fig. II.12. In Fig. II.12a, the average length of the two MTs is shown when simulations start from a short length, in Fig. II.12b simulations begin at a long MT length. Fig. II.12c shows the difference of these states' stationary length. We find that this difference is large in an extended parameter region; here, two distinct stationary states exist: MT length regulation is bistable is the domain. Fig. II.12c also compares the extension of the bistable regime for a system of two well-mixed MTs (color code) with the result obtained for a single MT (red line), cf. Fig. II.3e in the main text.

Furthermore, with the help of simulations, it is possible to systematically explore how accurate length regulation of the individual MTs functions. To this end, we have computed the deviation of the MTs' length from their average. We denote with $\overline{L}_t$ the momentary average length of the two MTs at time t. A good measure for the accuracy of length regulation is the average relative

standard deviation of MT length,

$$\left\langle \frac{\sqrt{\sum_i (L_i - \overline{L}_t)^2}}{\overline{L}_t} \right\rangle_t . \tag{II.24}$$

Here, $\langle \cdot \rangle_t$ signifies that the average is taken over time. This quantity is depicted in Figs. II.12d–II.12e. We observe that for small motor concentrations and large tubulin concentrations (the North West part of these diagrams), the relative deviation of the MTs' length from their average value is small. For large motor, or small tubulin concentrations (the South East part), the relative deviation is large. However, we find that the concentration regime confined in this way is identical to the domain in which the MTs completely depolymerize, Figs. II.12a–II.12b. Therefore, absolute fluctuations are small in this domain. In conclusion, length regulation functions accurately for all concentrations.

Taken together, when resources are shared infinitely fast between two or more MTs, we recover the findings obtained for a single MT. The length regulatory mechanism is accurate, and bistability also persists in these larger systems.

A.5.2. Shared reservoirs with finite diffusion

Having discussed the case of many MTs in a well-mixed system, let us now examine the implications of these findings for an *in vitro* or *in vivo* experimental system.

First, let us estimate when the assumption of a well-mixed system breaks down. With Fick's law, typical diffusion constants of several $10^{-8} \mathrm{cm}^2\mathrm{s}^{-1}$ (207) for tubulin imply that within the time it takes for MTs to reach their stationary length, say, an hour (Fig. II.11), the length scale which is explored by free diffusion is of the order of several 100μm. This is significantly below the length scales of our experimental setup. Therefore, in the *in vitro* experiments performed in this study, it is likely that the global system does not behave well-mixed but rather that different parts of the solution may develop independently.

We found in the previous Section that MTs in a well-mixed system can either become short, or long, but all of these MTs approach the same length. In spatially separated regions, MTs can therefore evolve differently: If the local average initial length in a part of system is short, the MTs in this region is likely to evolve collectively towards the short length; if in another part the initial local average length is long, these MTs will get long. Therefore, patches of long and short MTs will emerge which are spatially separated. In conclusion, when the length distribution of the resulting population of MTs is measured under a microscope, we expect two "classes" of MTs: One class of short, another with long length. This is what we find in our *in vitro* experiments: In a certain concentration regime, MTs with two characteristic length scales coexist, Fig. II.4a. Further evidence for the existence of spatial patches comes from an experiment, where Kip3 was added to MTs at a concentration of 20nM, and one part of the solution was incubated at rest, whereas the other part was mixed constantly. In the latter case, we expect that the complete system may be considered well-mixed. Therefore, it is unlikely that spatial patches of different tubulin length exist. In fact, in the case of constant mixing, the length distribution of MTs is unimodal, as opposed to the bimodal distributions for MTs at rest, Fig. II.22. We conclude that

bistability in the sense of our theoretical treatment imply bimodal length distributions in our *in vitro* experiments.

Whether bistable length regulation, and the associated two classes of MTs, as described in this work becomes important in cells, we may not say with certainty. On one hand, length scales, e.g. in the mitotic spindle (24, 25) are shorter than the extension of our experiment. As a consequence, one might think that in a system like a cell, protein is well-mixed. On the other hand, protein cannot diffuse freely within a cell due to the presence of intracellular structures such as cytoskeletal filaments. It is likely that under these crowded conditions, diffusion is significantly slowed down. In addition, both kinesin and tubulin can associate with MTs. If, for example, a kinesin-8 motor attaches to a MT, it may remain there for minutes and longer, because the detachment rate from the MT is very small (21), and the motor typically has to walk until the end of the MT until it may detach (132). In conclusion, we hypothesize that the separation of length scales, such as described here, is also relevant in cells. Hence, also here, we expect that bistability and the associated two distinct classes of MTs are important.

A.6. Experimental Methods

Protein expression and purification.   Porcine tubulin was purified from porcine brain (Vorwerk Podemus, Dresden, Germany) using established protocols as described previously (208). Histidine-eGFP tagged *Saccharomyces cerevisiae* kinesin-8, Kip3-eGFP, was expressed and purified using established protocols as described previously (20).

MT polymerization.   To produce GMP-CCP grown rhodamine labeled MTs, a MT polymerization (MTP) solution was incubated on ice for 5 minutes and then for 1-3 hours (duration determines the MT length distribution) at 27 °C to polymerize MTs. The MTP solution consisted of 100 μl of BRB80 (80 mM Pipes [Sigma], pH 6.9, with KOH [VWR], 1 mM EGTA [Sigma], 1 mM MgCl2 [VWR]) supplemented with 2μM porcine tubulin (1:3 mixture of rhodamine-labeled and unlabeled), 1 mM GMP-CPP (Jena Bioscience, Jena, Germany) and 1 mM MgCl2.

Simultaneous polymerization and depolymerization of MTs.   After the respective incubation period, the MTP solution was divided into parts of 25 μl and each part was supplemented with, (1) a dilution of Kip3-eGFP ranging from $0 - 400$nM, (2) 10 mM ATP (Roche), (3) 0.2 mg/ml casein (Sigma) and 0.1% Tween20 (Merck) for 1 hour at 27 °C. ATP enabled active motility of Kip3-eGFP to the MT plus ends and the casein as well as Tween20 prevented clustering and denaturing of the Kip3 motors. After 1 hour the Kip3-MT interaction in the 25 μl parts was terminated by addition of 300 mM KCl. After 1 minute incubation time, 1 μl of the solution was added to the imaging solution (BRB80 with 0.2 mg/ml DTT [Sigma], 40 mM glucose [Sigma], 110 mg/ml glucose oxidase [Serva] and 22 mg/ml catalase[Sigma]).

Sample preparation for imaging MT length distribution.   To image the MTs, microfluidic flow channels were constructed, as described in Korten et al. (209), using dichlorodimethylsilane (DDS) coated 18 mm $\times$ 18 mm glass coverslips (Menzel, Braunschweig, Germany; #1.5) on DDS coated 22 mm $\times$ 22 mm coverslips separated by parafilm. Typically, each coverslip contained four

flow channels with dimensions of 18 mm × 2 mm × 100 μm. The channels were flushed with a sequence of: (i) antibody solution consisting of 3 mg/ml anti-beta tubulin antibody (SAP.4G5, Sigma) in PBS in order to unspecifically bind antibodies to the surface (incubation time 5 minutes), (ii) Pluronic F127 (Sigma, 1% in PBS) in order to block the surface from unspecific protein adsorption (incubation time > 60 minutes), (iii) 4 times BRB80 buffer to remove excess F127 in solution and exchange buffers, (iv) imaging solution, with 1 μl of the different 25 μl parts (MT polymerization mixture + varying concentrations of Kip3-eGFP) incubated for 2 minutes to allow MTs and free tubulin to attach to the surface, and (v) imaging solution to remove the MTs and free tubulin still in solution.

Image acquisition.   Optical imaging was performed using an inverted fluorescence microscope (Zeiss, Axio Observer Z3, Carl Zeiss, Göttingen, Germany) with a 63x oil immersion 1.46 NA objective (Zeiss) in combination with an electron-multiplied charge-coupled device camera (Andor iXon Plus, Andor Technology, Belfast, UK) controlled by Metamorph (Molecular Devices Corporation, Sunnyvale, CA, USA). A Lumen 200 metal arc lamp (Prior Scientific Instruments Ltd., Cambridge, UK) was used for epifluorescence excitation. Rhodamine-labeled MTs immobilized on the surface were imaged using a TRITC filterset (Ex 534/30x, DC BC R561, EM BL593/40, all Chroma Technology Corp., Rockingham, VT) with an exposure time of 200 ms per frame. 20 images were acquired at different regions to scan the entire channel.

Image Analysis.   Image analysis was performed using FIESTA tracking software (210) to track individual MTs in every imaged frame and obtain their length with nanometer precision. MTs smaller than 500nm were ignored (visually not very different from potential tubulin clusters) from the image analysis leading to undersampling at lower microtubule lengths (< 500nm). Statistics performed on the MT lengths are discussed in the experimental results.

Measurement of tubulin concentration incorporated in MTs.   To measure the concentration of free tubulin in the MTP solution after incubation times of 1.5 hours and 3 hours, the solutions were centrifuged using a Beckman airfuge (Beckman, Brea, CA) at 100,000g for 10 minutes. SDS-PAGE gel analysis was performed on the supernatant (free tubulin in MTP solution), the pellet (resuspended in 100 μl BRB80) and stock tubulin (diluted in 100 μl BRB80). The intensities of the gel bands were measured using ImageJ to obtain estimates of the percentages of tubulin incorporated in the polymerized MTs (see Fig. II.20).

A.7. Variability in experimental data

Number of MTs in per field of view.   This is a qualitative indicator of the density of MTs growing in the MTP solution under different conditions. The number of MTs attaching on the channel surface depends on the density of anti-beta tubulin antibodies adsorbed on the channel surface which in turn depends on (i) the hydrophobicity of the glass coverslips, (ii) the volume in the channel (built manually) and (ii) the time of incubation of antibodies in the channel. Variations

in these factors could be minimized in a single experimental set allowing us to still infer the relative difference in MT density induced by different concentrations of Kip3. However, it is difficult to compare different sets of experiments.

Initial MT length distribution in Control experiments. MT growth is extremely sensitive to the time of polymerization, concentration of tubulin, temperature, ionic strength and pH of the growth solution. While efforts were made to keep the conditions similar between different experimental sets, the initial MT length distribution before addition of Kip3 still varied significantly, as can be seen in Fig. II.24.

Microtubule length distribution. While separating the MTP solution, mixing reagents (ATP, Kip3 solution, casein, Tween20, KCl, etc.), diluting the solution and flushing the solution into the channels, few MTs would break due to the shear forces generated. Therefore, it is possible that the number of short MTs is slightly overestimated in the length histograms.

Amount of active Kip3 motors. The Kip3 concentration indicated in the experiments is the amount of protein added to the solution and not the concentration of active Kip3 motors. Unfortunately, it is impossible to prevent the inactivation of a percentage of motors during the purification, snap-freezing and thawing process. Further, one would expect some motor clustering as well. The motor is soluble in a high ionic strength buffer but in the BRB80 solution used in the MTP solution, motors tend to cluster. To minimize the clustering of motors casein, Tween20 and a high concentration (10 mM) of ATP was added in the MTP solution. Due to the above reasons, it is not possible to quantitatively compare the theoretical and experimental values for Kip3 concentration.

A.8. Additional Figures
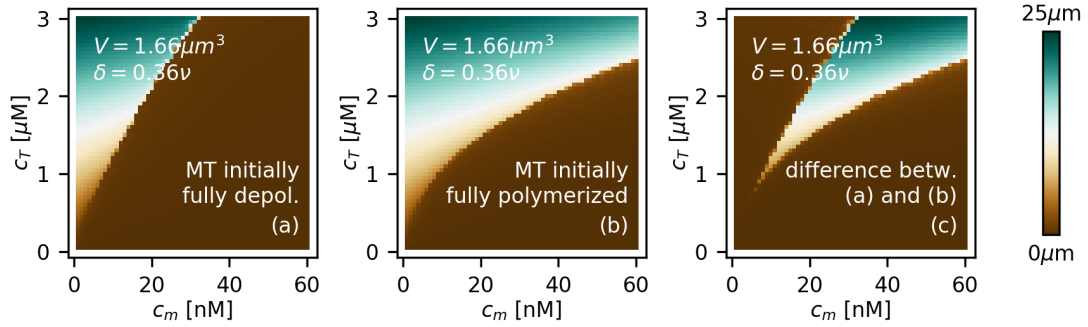
Figure II.13.: Scan of the MT length (color code) with the motor and tubulin concentrations as control parameters, see also Figs. II.3a–II.3b in the main text. In panel (a), MTs are initially short, in panel (b), MTs start fully polymerized. Part (c) shows the difference between the values obtained in the first two parts, and therefore indicates the parameter regime in which MT length is bistable. Because the estimates for the volume V and the depolymerization rate δ have significant uncertainties, we explore in which way the dynamics change when these parameters are varied. Here, $\delta = 2.4\text{ s}^{-1} = 0.36\nu$, $V = 1.66\mu m^3$ (such that $1\ \mu M \hat{=} 1000$ dimers per protofilament).
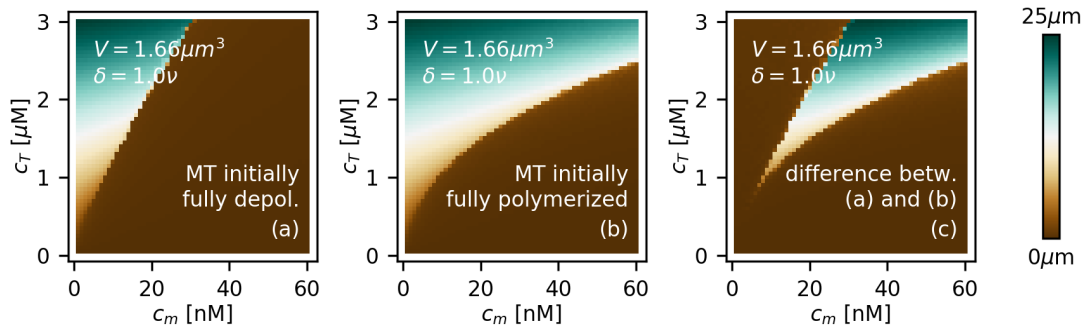
Figure II.14.: As in Fig. II.13, but with $\delta = 6.35\text{ s}^{-1} = \nu$, $V = 1.66\mu m^3$ (such that $1\ \mu M \hat{=} 1000$ dimers per protofilament).
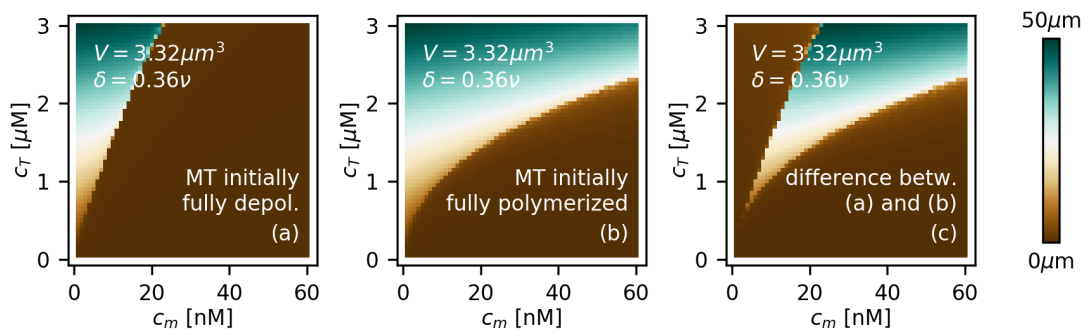
Figure II.15.: As in Fig. II.13, but with $\delta = 2.4\text{ s}^{-1} = 0.36\nu$, $V = 3.32\mu m^3$ (such that $1\ \mu M \hat{=} 2000$ dimers per protofilament).
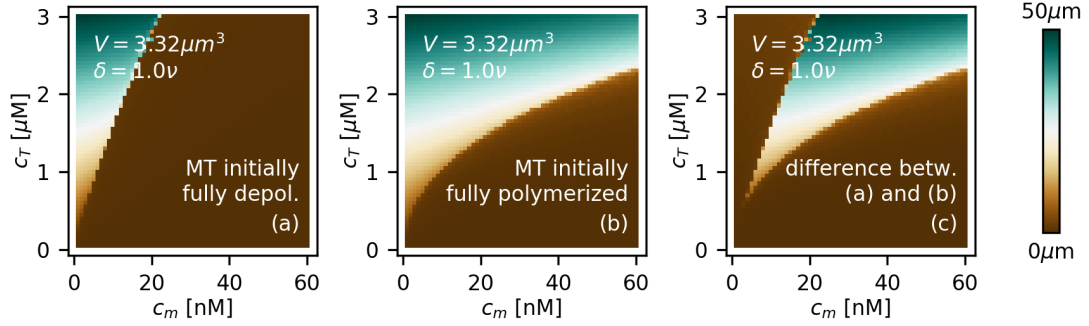
Figure II.16.: As in Fig. II.13, but with δ = 6.35 s⁻¹ = ν, V = 3.32μm³ (such that 1 μM≙2000 dimers per protofilament).
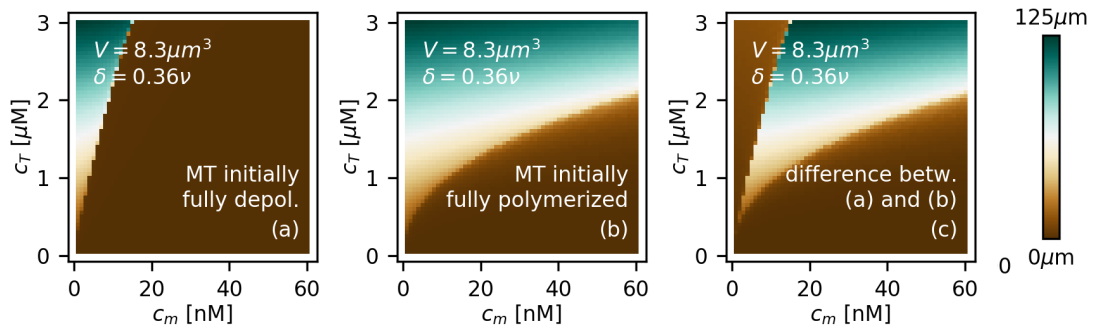
Figure II.17.: As in Fig. II.13, but with δ = 2.4 s⁻¹ = 0.36ν, V = 8.3μm³ (such that 1 μM≙5000 dimers per protofilament).
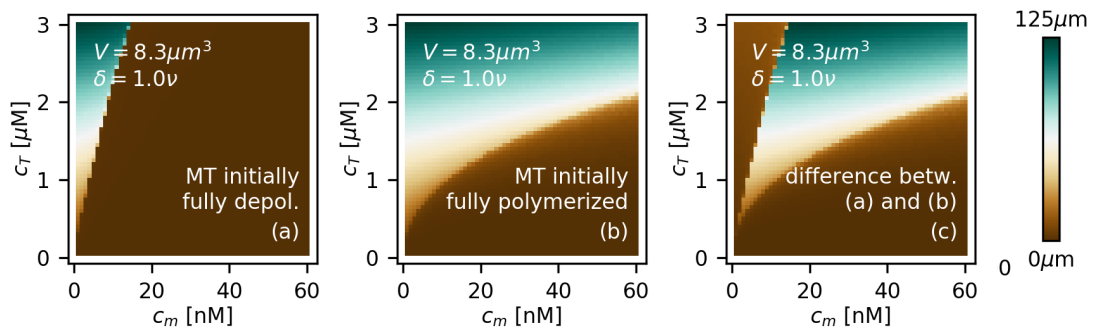
Figure II.18.: As in Fig. II.13, but with δ = 6.35 s⁻¹ = ν, V = 8.3μm³ (such that 1 μM≙5000 dimers per protofilament).
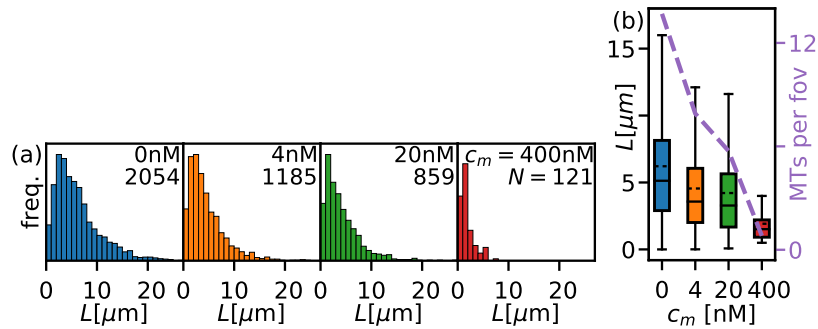
Figure II.19.: Length distribution of MTs grown for 1.5 hours followed by addition of 0nM, 4nM, 20nM and 400nM Kip3 for 1 hour. (a) MTs have a median length of 5μm (iqr=5μm) when no Kip3 is added. Histograms of MT lengths (bin size = 1μm) at different Kip3 concentrations indicate that MTs remain in the short length regime with the median MT length going down on increasing the Kip3 concentration, as seen in the box plots (b). As seen from the dashed line (right scale) of panel (b), the average number of MTs per imaged frame decreases with the concentration of Kip3.
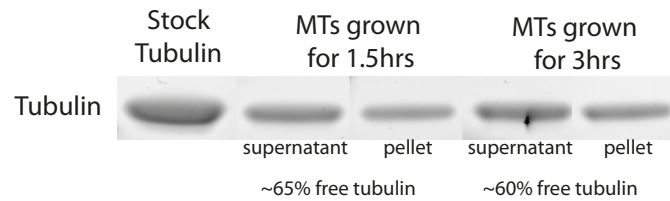
Figure II.20.: Percentage of free tubulin in solution. MTs were grown for 1.5 hours and 3 hours and centrifuged to separate the free tubulin (supernatant) from the tubulin incorporated in MTs (pellet) and an SDS gel was performed. The intensities of the supernatant and the pellet indicate that MTs grown for 1.5 hours have ~65% free tubulin while MTs grown for 3 hours have ~60% free tubulin. The intensities of the supernatant and the pellet approximately add up to the intensity for the stock tubulin.
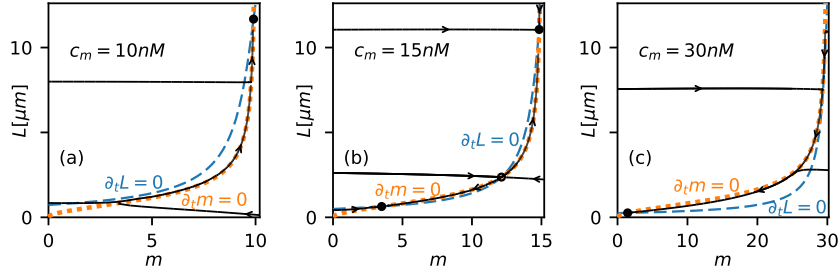
Figure II.21.: Plots of representative stream lines of the vector field $(\partial_t m, \partial_t L)$ as from Eqs. (II.2) in the main text, for the three different motor concentrations of Fig. II.3c in the main text at tubulin concentration $c_T = 1.5\mu$M. Here, the approximate mean-field theory result for the flux off the MT, Eq. (II.4) in the main text, was used. The null clines $\partial_t m = 0$ and $\partial_t L = 0$ are also shown, cf. Fig. II.7. For all three concentrations, the stream lines are almost horizontal until they approach the cline $\partial_t m = 0$. This implies that the dynamics of m are much faster than those of L. This is due to the fact that motor binding and unbinding is possible at every binding site along the whole lattice, whereas MT elongation and shrinkage occur at the plus end only. Once the number of motors on the MT is quasi-stationary, the MT slowly adapts its length until its state reaches a fixed point. Because this effectively restricts the MT-motor dynamics to the nullcline $\partial_t m = 0$, a reduction to this subspace is possible, which was used in Fig. II.3c in the main text. In parts (a) and (c), only a single fixed point exists, and a MT at these motor concentrations will always approach the uniquely defined stationary state. By contrast, for the intermediate motor concentration displayed in part (b), two fixed points at the north east, and south west of the diagram are present. In the middle, the separatrix and the corresponding saddle point divide phase space into regions attracted by the respective fixed points.
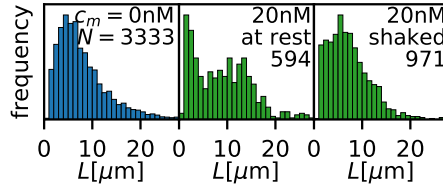
Figure II.22.: Constant mixing of the MT-Kip3 solution changes the length distribution. 20 nM Kip3 were added to a solution of MTs which were pre-grown for 3 hours. One part of the resulting solution was left at rest for another hour, a second part was constantly mixed in a shaker for the same time. The resulting length distributions are strikingly different: While a bimodal distribution is observed for the part at rest, we find a unimodal distribution for the solution mixed in a shaker. This supports our interpretation of bistability: MTs jointly evolve to either the long or the short stationary length, as long as the system is so small that all resources are well-mixed. MTs at two different lengths can therefore only coexist in a solution when spatially separated domains exist in a large system. When a system is constantly mixed, we can assume that it behaves well-mixed on all length scales. As a consequence, only a single characteristic length is observed in the system.
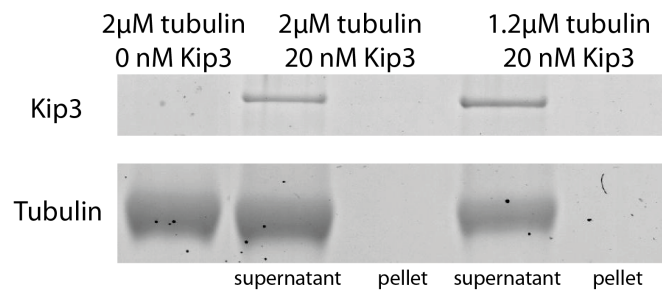
Figure II.23.: MTs do not nucleate in the presence of Kip3. 20 nM Kip3 were added to solutions of 2 μM and 1.2 μM of tubulin. Here, the latter concentration approximately corresponds to the amount of free tubulin remaining in solution after MTs have formed in the absence of Kip3, cf. Fig. II.20. Each solution was centrifuged after incubation of 1 hour, the supernatant and pellet were separated and an SDS gel was performed. We find that the intensity of the supernatant greatly exceeds the intensity of the pellet, both for Kip3 and tubulin. This indicates that (almost) all tubulin and Kip3 is free at these conditions. MTs therefore do not nucleate in the presence of 20 nM Kip3.
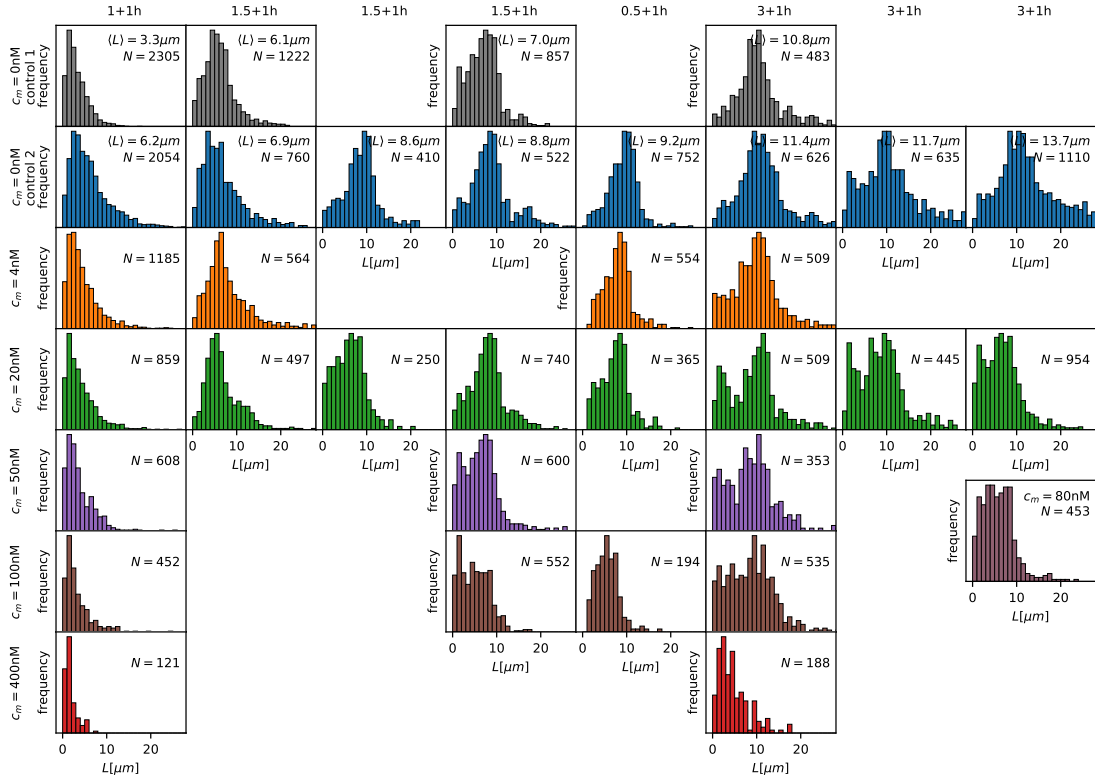
Figure II.24.: Overview of the experimental measurements. Shown are MT length distributions recorded in various experiments at different conditions. For each column, the same initial solution was used, and varying amounts of Kip3 were added to a solution of MTs pre-grown for a specific amount of time (indicated in the column head). Varying the polymerization time of MTs in the absence impacts on the length distribution (control 1; MTs imaged directly at the time point when Kip3 is added to the other parts), although precise control of the average length is not possible in this way, see Sec. A.7 for details. Subsequent to initial growth, MTs were incubated without (control 2), or with Kip3 for another hour. The columns are ordered by the MTs' average length, when no Kip3 was added (control 2). We find that for short initial lengths, all length distributions are unimodal. In contrast, for longer initial MT lengths, distributions at certain motor concentrations become bimodal. The most prominent qualitatively difference is found for $c_m = 20$ nM and 50 nM.

7. A minimal lattice gas model for bistable length regulation

7.1. Introduction

In Chapter 6, we studied a model motivated by the depolymerising molecular motor kinesin-8, which is known to influence and regulate MT length (23). A central goal of this study was to connect the simple lattice gas model with *in vitro* experiments conducted in the group of Stefan Diez. Consequently, relatively many biological and microscopic details were included in the model. In particular, in the original model of Chapter 6, motors were able to attach to and detach from any site on the MT. This combination of processes obeying (attachment/detachment) and breaking (directed transport) detailed balance does not only lead to the emergence of interesting phenomena (155, 156), but also significantly raises the complexity of the theoretical treatment. As a result, the mean-field theory developed in Chap. 6 relied on an approximate approach. We succeeded in deriving a more refined mean-field theory, shown in Appendix A, but the Equations involved were so complicated that key results, such as the phase transition lines leading to the stability diagram, could only be obtained numerically.

While the significance of the model presented in the previous chapters in a biological and physiological context is indisputable, there is hence need for a simplified model in a doctoral thesis conducted in the field of theoretical physics. In the following, we will therefore report on results of a similar but conceptually simpler model where attachment and detachment of motors are only possible at the first and last site of the lattice, respectively. We will show that, while the key phenomena observed in the original model of Chap. 6 are conserved, the simplification of the model leads to a reduction of the complexity of the equations, and by that allows for a closed mean-field theory. With a full theoretical understanding at hand, we are also able to find heuristic arguments for, e.g., the emergence of bistability.

7.2. Model description

We are interested in a theoretical description of the motion of depolymerizing molecular motors along MTs and their interactions with the MT. We concentrate on molecular motors of the kinesin-8 family such as Kip3 from *S. cerevisiae*, which are known to catalyze depolymerization, and move in a directed fashion toward the MT plus end. Hereby, they predominantly walk along a single protofilament, i.e. parallel to the axis of the MT (106, 107), and bind to distinct binding sites on each tubulin heterodimer (211), subunit of the MT (41, 42). This implies that the motor dynamics can effectively be described in terms of the stochastic motion of particles along a one-dimensional lattice of dynamic length $L(t)$.
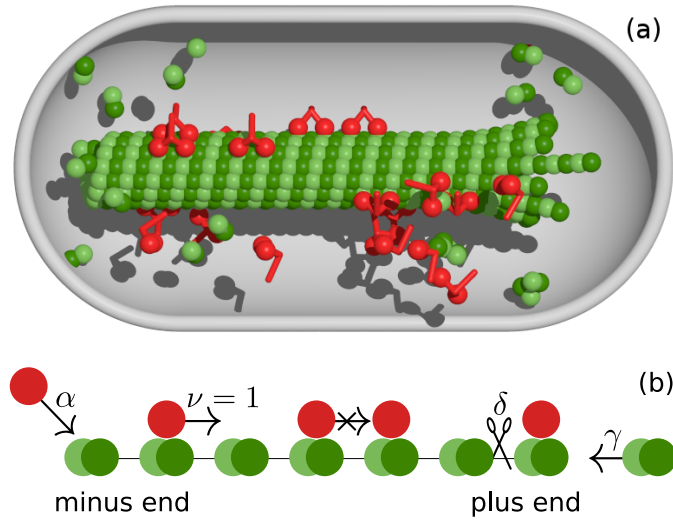
Figure II.25.: *The model. (a) Molecular motors interact with a MT in a closed compartment. (b) Motors enter the lattice at the minus end of the lattice with rate α, provided the first site is empty. They then proceed stepwise at the hopping rate ν, obeying exclusion. Having arrived at the right end, a motor leaves the lattice at rate δ, taking the last site with it. MT depolymerization competes with spontaneous lattice polymerization at rate γ. Because motor attachment and MT polymerization are concentration dependent, their speeds depend on the availability of motors and tubulin dimers in the reservoir, respectively, Eqs. (II.25).*

We employ a driven diffusive lattice gas model (145, 149, 153) for spontaneous MT polymerization and kinesin-catalyzed MT depolymerization (2, 22, 23, 191), as illustrated in Fig. II.25. The dynamics of motors on the lattice are described by a variant of the totally asymmetric simple exclusion process (TASEP) (146, 147). Here, motors enter the lattice at its left end, corresponding to the MT minus end, at rate α. From there, they proceed stepwise towards the right, i.e., into the direction of the MT plus end, at rate ν. Hereby, they obey the exclusion principle, indicating that no more than a single motor can occupy a binding site. Having arrived at the plus end, motors catalyze the removal of the terminal site at rate δ; on depolymerization the motor also detaches from the MT. This competes with spontaneous lattice polymerization at γ. We describe the state of each site, i, in terms of its occupation number, $n_i \in \{0, 1\}$, where $n_i = 0$ and $n_i = 1$ signify an empty and occupied site, respectively.

We consider a MT in a closed compartment with volume V. In this volume, the absolute number of the tubulin dimers and motors in the system is limited. Because polymerization of the MT through binding of tubulin, as well as the binding of motors to the lattice, depletes the concentrations of these proteins, the MT polymerization rate and the motor attachment rate decay with the MT length L and the number of motors on it, m, respectively, as $\gamma = \gamma_0(c_T - L/V)$, and $\alpha = \alpha_0(c_m - m/V)$; here, L is measured in units of the length of a tubulin dimer, $a = 8.4$nm (51), and γ_0 and α_0 are normalized rates per volume concentration of the respective protein. Introducing the rescaled rates $\hat{\alpha} = M\alpha_0/V$, and $\hat{\gamma} = T\gamma_0/V$, which denote the motor injection and MT polymerization rate, respectively, at undepleted conditions, the resource dependence can be

expressed as

$$\alpha = \hat{\alpha}\frac{M-m}{M} \,, \tag{II.25a}$$

and

$$\gamma = \hat{\gamma}\frac{T-L}{T} \,. \tag{II.25b}$$

Here, $T = c_T V$ and $M = c_m V$ are the total number of tubulin dimers, and kinesin motors, respectively, which are available in the volume V. The rescaling to the parameters $\hat{\alpha}$ and $\hat{\gamma}$ is convenient because these rates are directly comparable to the hopping rate v. In addition, it allows for a reduction of the five parameters α_0, γ_0, c_m, c_T, and V to only four: $\hat{\alpha}$, $\hat{\gamma}$, M, and T.

Throughout this work, we will use the hopping rate as the basic time scale, $v = 1$, and the lattice spacing between two tubulin dimers as the unit of space, $a = 1$.

In Chapter 6, we have studied a model similar to the one presented here. The major difference is that in the former model particles can attach to any lattice site, and may prematurely detach before having arrived at the plus end. While the focus of that model was to describe an experimental situation as detailed as possible, the model presented in this Chapter has two advantages: (i) It is conceptually simpler and has less parameters than the original model. As a result, a full analytical description is possible, while most results presented in Chapter 6 relied on numerical calculations. (ii) The consideration of attachment and detachment kinetics along the MT, which was included in the model of Chapter 6, can lead to motor gradients and domain walls on the lattice (155, 156), phenomena similar to the behavior of lattice gas models which take limited resources into account (162). As a consequence, when limited resources as well as attachment at detachment of particles along the lattice are considered at the same time, the physical principles causing the observed phenomena cannot be determined uniquely. The advantage of considering a model which disregards binding and unbinding of motors in the MT bulk is therefore that the role of limited resources can be studied in an isolated environment.

7.3. Simulation results

We performed extensive stochastic simulations, using Gillespie's algorithm (201), and explored how the MT dynamics depend on the model parameters. Regardless of the specific parameter choice, we observe that the lattice evolves to a state in which its length shows only relatively small fluctuations about a stationary value L^*. Likewise, the number of motors on the MT, m^*, is on average constant. Figs. II.26a–II.26d show four representative kymographs of the MT lattice for model parameters as indicated. Here, simulations start from an initially fully depolymerized lattice (shown in green). These kymographs represent four distinct phases, in which the motors (shown in red) form qualitatively different density profiles on the lattice: In Fig. II.26a, the motor density quickly assumes a high value (high density phase: HD); in contrast, in part (b) the motor density remains low along the whole MT (low density phase: LD); for other parameters, part (c), the lattice is half occupied with motors — at this occupation, the motor current is maximal (maximal current phase: MC); finally, for the case shown in part (d), the density profile shows
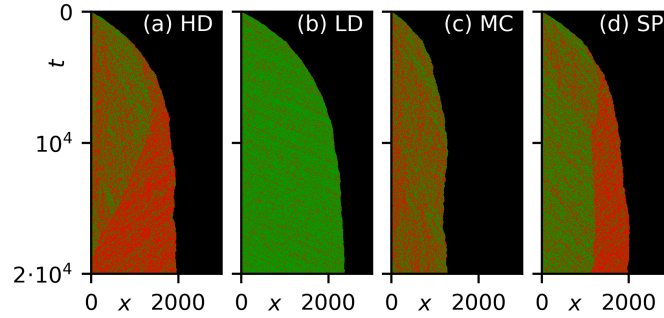
Figure II.26.: Kymographs of the dynamics obtained from simulation runs of the model. Simulations start from a fully depolymerized MT. Motors are shown in red, empty lattice sites in green. For all cases, the steady state in which MT length and the occupation of the lattice sites by motors become stationary is reached quickly. We observe four qualitatively different phases, in which we find that (a) the motor density is high (HD), (b) their density is low (LD), or (c) the density equals 1/2; here, the motor current becomes maximal (MC). In the fourth case, the shock phase (SP) shown in part (d), a localized domain wall (DW) separates coexisting regions of low and high motor density. Parameters: (a) $\hat{\alpha}$ = 0.7, $\hat{\gamma}$ = 0.6, δ = 0.3, M = 3500, T = 3000; (b) $\hat{\alpha}$ = 0.2, $\hat{\gamma}$ = 0.6, δ = 0.3, M = 1000, T = 3000; (c) $\hat{\alpha}$ = 0.8, $\hat{\gamma}$ = 0.5, δ = 0.7, M = 4000, T = 2500; (d) $\hat{\alpha}$ = 0.5, $\hat{\gamma}$ = 0.6, δ = 0.3, M = 2500, T = 3000.

coexistence of a region with low motor density at the left, and high motor density at the right end — both density regions are separated by a domain wall (DW), also called shock (shock phase: SP). Remarkably, not only the MT length becomes stationary in the SP but also the position of the DW on the lattice.

The long-term evolution of the lattice may or may not depend on initial conditions, depending on model parameters. Fig. II.27 shows kymographs of a lattice when simulations are started from a short and long length, respectively; the parameters are equal for part II.27a and II.27b, as well as for II.27c and II.27d. We observe two different scenarios: For the parameters shown in Figs.II.27a–II.27b, the initially short, and the initially long lattice approach a common stationary state. By contrast, for the parameters of Figs. II.27c–II.27d, the lattice which was originally relatively short shrinks, while the initially relatively long lattice grows. Despite equal sets of parameters, the MTs shown in these simulation runs evolve towards different stationary states: The system behaves bistable. Our numerical simulations reveal that there is a critical length which separates simulation runs evolving towards the longer from those approaching the shorter stationary length. We also find that while the evolution towards two distinct stable stationary states is the dominant behavior in particular for large reservoir sizes, occasional switches between both lengths can be observed, predominantly for MTs in small volumes (data not shown).

The existence of qualitatively different phases, as well as the presence of monostable and bistable parameter regimes, have both also been observed for the similar model studied in Chap. 6 whose results have been published in Ref. (2). This model allowed for motor attachment and detachment kinetics also in the bulk of the MT lattice, and is consequently more complex to analyze. Its theoretical predictions, including the existence of the bistable regime, were confirmed by an accompanying *in vitro* experiment. The agreement of the key emergent effects of the original
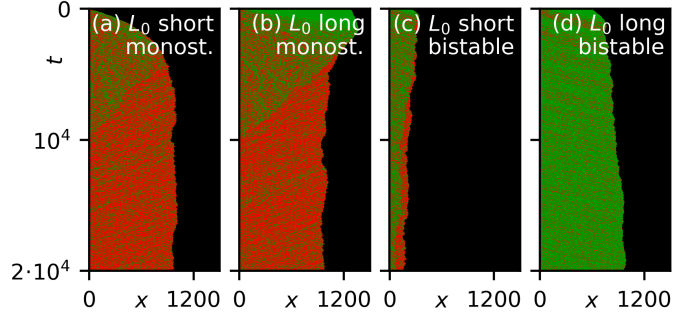
Figure II.27.: Kymographs of the dynamics for two different parameters sets. In panel (a)–(b) the model parameters are chosen as $\hat{\alpha} = 0.7$, $\hat{\gamma} = 0.6$, $\delta = 0.3$, $M = 1750$, $T = 1500$, in (c)–(d) they assume the values $\hat{\alpha} = 0.7$, $\hat{\gamma} = 0.23$, $\delta = 0.3$, $M = 175$, $T = 2300$. The color code is the same as in Fig. II.26. For the first parameter set, both (a) a lattice starting from an initially short length, as well as (b) an originally long (and empty) lattice approach a common stationary state. In contrast, for the parameters of parts (c)–(d), MTs which are initially (c) short approach a short, (d) originally long MTs a long length: The system behaves bistable.

model presented in Chap. 6 with the simplified model of this study is encouraging, as it justifies the model reduction conducted here. We conclude that a simple model is sufficient to describe biologically and physiologically relevant phenomena such as bistable length regulation of MTs.

7.4. Theoretical analysis

In order to understand the length-regulation mechanism as well as the emergence of bistability in detail, a full theoretical description of our model is indispensable. This includes the analysis of the intricate interplay of the crowding phenomena in the lattice bulk, and the polymerization-depolymerization dynamics at the tip. We can express the rate of change of the MT length resulting from the antagonism of spontaneous lattice polymerization, and motor-induced depolymerization as

$$\partial_t L = \gamma - \rho_+ \delta , \qquad (\text{II.26a})$$

where time and space are measured in units of the hopping rate and the lattice spacing between two tubulin dimers, respectively. Here, $\rho_+ = \langle n_+ \rangle$ is the probability that the binding site directly at the MT tip is occupied by a motor. Likewise, the number of motors on each protofilament changes when a particle enters the lattice at the left, or leaves it at the right end:

$$\partial_t m = \alpha(1 - \rho_-) - \rho_+ \delta , \qquad (\text{II.26b})$$

where $\rho_- = \langle n_0 \rangle$ is the motor occupation density at the minus end. These equations are incomplete without a specification of the tip densities, or an additional expression relating L and m. A way to obtain the missing relation is to consider an effective description of the MT model which utilizes the finding that the lattice length as well as the motor injection rate are (almost) constant

at the stationary state. We will show in the following that with this strategy, Eqs. (II.26) can be completed, which eventually leads to a solution for the stationary state length L^* and the number of motors on the MT, m^*.

It is important to note that our simulation results imply that the relative fluctuations of the lattice length are small, $\Delta L/L^* \ll 1$ at stationarity, cf. Fig. II.26. Similarly, the relative fluctuations of the motor occupation number is small, $\Delta m/m^* \ll 1$, from which we conclude that also the injection rate α shows only mild variations at stationarity. In addition, we find that the processes leading to a change of the lattice length are typically slow compared to motor hopping, $\gamma^* = \gamma(L^*) = \rho_+^* \delta \ll 1 = \nu$. This separation of time scales implies that in the vicinity of the plus end, where changes to the lattice occur, the motors quickly reestablish their local stationary density whenever the lattice shrinks or grows by one site. Because at the stationary state the dynamic MT model has thus a dynamic but effectively constant lattice length L^*, as well as a dynamic but effectively constant injection rate $\alpha^* = \alpha(m^*)$, we may rephrase our model in terms of an effective model. Here, both the lattice length and the injection rate are (exactly) constant, and therefore this effective model is identical to the TASEP on which our model was originally based. To ensure that both models show the same behavior, we require that (i) the TASEP lattice length equals the average MT lattice length at stationarity L^*; (ii) the TASEP injection rate α equals the average MT injection rate at stationarity α^*; (iii) the TASEP rate β, at which particles leave the lattice (without changing the lattice length, see Fig. II.28) equals the rate δ in our model, at which motors cut off the last lattice site and dissociate from there at the same time.

With this correspondence, the density profile of motors on the MT lattice can be compared with the particle density profile of the TASEP, see Fig. II.28. In order to compute the average motor density on the MT lattice with varying length, shown in the left part of this Figure, snapshots of a MT at different times or from different simulation runs are aligned at their minus (blue), or plus ends (yellow), respectively, before taking the mean; the total density profile is then obtained by merging the two half profiles in the middle. The density profiles of the left part of Fig. II.28 obtained in this way correspond to the kymographs of Fig. II.26. For parts II.28a–II.28c, left panels, the density profile is flat, except for a discontinuity at II.28a the plus end, II.28b the minus end, or II.28c at both ends. For these three cases, the MT density profiles agree excellently with the corresponding TASEP density profiles (II.28a–II.28c, right panels). By contrast, in the SP the density profile of the MT model looks different from the corresponding TASEP density profile, Fig. II.28d. The reason is that in the TASEP, a DW is only present on the lattice for fine-tuned parameters $\alpha = \beta$. Moreover, the TASEP DW is not localized, i.e., its position diffuses across the lattice. In effect, while a snapshot of the density profile at a *specific point in time* is similar to the left density profile of Fig. II.28d, the *average* profile shown in the right panel comprises a straight line. However, the density profiles of the TASEP and the MT model agree in a property which will be of central importance later: The tip densities are approached continuously from the lattice bulk for both the plus and the minus end, and the values at the tips agree for the MT and the TASEP model.

We have thus uncovered an important aspect of resource limitation: They lead to a localization of the DW (162). The mechanism is as follows: If the DW is located left of its stationary position, the number of particles on the lattice is greater than at the stationary state, and consequently only relatively few particles remain in solution, wich implies that the injection rate is relatively
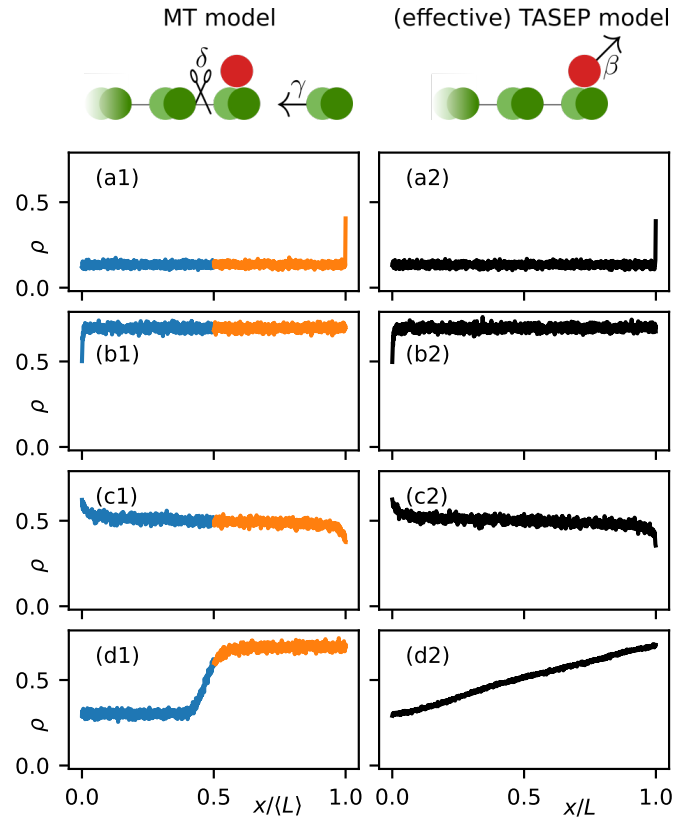
Figure II.28.: *Density profiles of the dynamic MT model (left), compared with the corresponding profile of its effective description in terms of the TASEP (right). For the dynamic lattice, the density profile is averaged by aligning MTs at their left (right) ends, so that the density near the minus (plus) end is obtained; the final profile is then merged in the middle. The parameters of the left panels are the same as for Fig. II.26a–II.26d; the parameters of the TASEP model in the right part of this Figure derive as explained in the main text. Panels (a) show the density profiles obtained for the LD phase, (b) the HD phase, in (c) the MC phase is shown. For these phases the density profile of the MT with varying length and injection rate agrees well with the average profile of the TASEP with constant length and injection rate. In contrast, the profile of the SP, panel (d), is different for both cases: While for the MT model, the profile shows a domain wall (DW), the profile is flat for TASEP. The reason is that the DW found in TASEP diffuses across the lattice, i.e., it is not localized. On taking the average, a sharp density increase is therefore no longer observed, resulting in the continuous (average) density profile.*

small. In effect, relatively few particles enter the lattice while many particles can exit the lattice. Consequently, the DW is shifted towards the right. By contrast, if the DW is located right of its stationary position, many particles are left in the reservoir, and the injection rate is high. Therefore, many particles entering the lattice per unit time, and the DW is displaced to the left. These two mechanisms balance exactly at the stationary state, and thus the DW is localized.

Having found an effective description of the dynamic MT model in terms of the well-studied TASEP, we can now employ the theoretical framework of TASEP. While we refer the reader to some of the numerous extensive reviews, such as, e.g., Ref. (145, 149) for full details, we only summarize the most essential results about the different phases of TASEP here. In TASEP, four different phases have to be distinguished, see Fig. II.28: For the low density (LD) phase, Fig. II.28a, the bulk density ρ_b is determined by the particle injection rate, such that $\rho_b = \alpha$; this behavior is found provided $\alpha < \beta$ and $\alpha < 1/2$. For the high density (HD) phase, Fig. II.28b, present if $\beta < \alpha$ and $\beta < 1/2$, the bulk density assumes the value $\rho_b = 1 - \beta$. In case $\alpha, \beta > 1/2$, the bulk density $\rho_b = 1/2$, irrespective of the particular values of α and β, cf. Fig. II.28c; in this case, the particle current becomes maximal, suggesting the name maximal current (MC) phase. Finally, in case $\alpha = \beta < 1/2$, a DW separates regions of low motor density $\rho_l = \alpha$ at the left lattice end and high density $\rho_r = 1 - \alpha = 1 - \beta$ near the right end; as we noted earlier, the DW diffuses across the whole lattice, and therefore the average density profile, Fig. II.28d, right panel, is a straight line.

7.4.1. Strategy to obtain the stationary state

In order to find the stationary state properties of a MT with given parameters, we will now employ the following strategy:

- We will first *assume* that the MT settles into one of the four phases described above. For these phases, the density of particles on the lattice is known, and the number of particles on the lattice is directly related to its length. With this knowledge, the balance equations, Eq. (II.26) are complete and give rise to the steady state values L^* and m^*, from which we also find $\alpha^* = \alpha(m^*)$ with Eq. (II.25a).

- Having obtained numerical values for α^* and δ, which correspond to the rates α and β in the TASEP, it is now essential to *verify* that the dynamic behavior of the TASEP with these parameters is in fact given by the phase assumed in the first step. E.g., if we have assumed a HD phase originally, the obtained parameters should in fact yield $\delta = \beta < \alpha = \alpha^*$, as well as $\delta = \beta < 1/2$.

7.4.2. High density phase

For a start, let us consider the simplest case of the collective dynamics which we have found to be the HD phase. In this phase, the motor density is high along the complete lattice, and the density in the lattice bulk equals the plus end density, $\rho_+ = \rho_b$. Because the number of motors on the lattice changes only when a motor enters or leaves the lattice at one of the ends, at the stationary state the particle current onto the lattice equals the current off the lattice, and it is furthermore equal to the bulk current:

$$\alpha(1 - \rho_-) = \rho_b(1 - \rho_b) = \rho_+\delta . \tag{II.27}$$

Here, we have utilized the mean-field approximation $\langle n_i n_j \rangle \approx \langle n_i \rangle \langle n_j \rangle = \rho_i \rho_j$ which assumes that any correlations between the occupation of sites i and j can be neglected. From Eq. (II.27), the density at the plus end follows right away: $\rho^*_{+,HD} = 1 - \delta$. With Eq. (II.26a) and the resource dependence of γ, Eq. (II.25b), we obtain the steady state length:

$$L^*_{HD} = T(\delta^2 - \delta + \hat{\gamma})/\hat{\gamma} \,. \tag{II.28}$$

From these results, all other important steady state properties follow directly: The number of motors on the lattice is proportional to the lattice length: $m^*_{HD} = L^*_{HD}(1 - \delta)$. Therefore,

$$\alpha^*_{HD} = \hat{\alpha}(1 - m^*_{HD}/M) \tag{II.29}$$

is the stationary value of the injection rate of motors. With Eq. (II.27), we also find the motor density at the minus end as

$$\rho^*_{-,HD} = 1 - \delta(1 - \delta)/\alpha^*_{HD} \,. \tag{II.30}$$

7.4.3. Maximal current phase

Also for the case of fast motor injection at the left, and ejection from the right end, leading to collective dynamics in the maximal current (MC) phase, expressions for the relevant physical quantities can be obtained in a relatively straightforward manner. For the MC phase it is known that the bulk density is independent of the specific boundary rates α and δ. On average, one in two lattice sites is occupied, $\rho_b = 1/2$, maximizing the current: $j_b = \rho_b(1 - \rho_b) = 1/4$. As before, this current equals both the motor flux onto, and off the MT, which implies that $\rho^*_{+,MC}\delta = 1/4$. Consequently, the stationary state length is given by

$$L^*_{MC} = T\left(1 - \frac{1}{4\hat{\gamma}}\right) \,. \tag{II.31}$$

The injection rate α^*_{MC} follows from $m^*_{MC} = L^*_{MC}/2$ in the same way as Eq. (II.30).

7.4.4. Shock phase

As displayed in Fig. II.28d, the motor density profile is continuous at both tips for certain parameters, and it shows a discontinuity in the bulk, which is called the domain wall (DW). We demonstrated in Fig. II.26d that this DW is localized at a well-defined position on the lattice. In the SP, the motor density is constant at the minus end, $\rho_l = \rho_-$, as well as in the vicinity of the plus end, $\rho_r = \rho_+$. Both these densities extend into the lattice bulk. Hence, because of current conservation, we find similar to the considerations of the HD phase, Sec. 7.4.2 that the tip density in the SP is given by $\rho^*_{+,SP} = \rho^*_{+,HD} = 1 - \delta$. Therefore, also the steady state length of the SP is identical to the same quantity obtained for the HD phase: $L^*_{SP} = L^*_{HD}$.

A quantity of particular interest is the position of the DW of the lattice, x^*_w. It may be obtained by requiring that the motor current is constant along the lattice. The motor current left of the domain wall, $j_0 = \rho_l(1 - \rho_l)$ must in consequence equal the current right of it, $j_r = \rho_r(1 - \rho_r)$. Therefore, in agreement with the condition $\alpha = \beta$ from TASEP, we find $\rho_l = \alpha^*_{SP} = 1 - \rho_r =$

$1 - \rho^*_{+,SP} = \delta$, from which $\alpha^*_{SP} = \delta$ follows. On the other hand, we obtain the value of α^*_{SP} from its dependence on the number of motors on the lattice, Eq. II.25a. Furthermore, m^*_{SP} can be computed by integrating the motor density over the complete lattice: $m^*_{SP} = \delta x^*_w + (1 - \delta)(L^*_{SP} - x^*_w)$. From the two equations for α^*_{SP}, we obtain a condition for the position of the DW, which simplifies to

$$x^*_w = \frac{(\hat{\alpha} - \delta)\hat{\gamma}M + \hat{\alpha}(\delta - 1)[(\delta - 1)\delta + \hat{\gamma}]T}{\hat{\alpha}(2\delta - 1)\hat{\gamma}} \ . \tag{II.32}$$

7.4.5. Low density phase

Arguably the most difficult treatment has to be employed for the LD phase. The reason is that, for this phase, the bulk density $\rho_b = \alpha$ carries a direct resource dependence. This can be seen as follows: Because $\alpha = \alpha(m)$ as of Eq. (II.25a), the number of motors on the lattice feeds back on the injection rate which in turn determines the number of motors on the lattice. This implies that $m = \alpha(m)L$, which solves as

$$\alpha^*_{LD} = \frac{\hat{\alpha}M}{\hat{\alpha}L^*_{LD} + M} \tag{II.33}$$

in the stationary state. Conservation of the motor current together with Eq. (II.26a) implies $\alpha^*_{LD}(1 - \alpha^*_{LD}) = \gamma^*_{LD}$, which leads to a polynomial of third order:

$$0 = \hat{\alpha}^3 T(m^*_{LD})^3 + \hat{\alpha}^2 MT(1 - 3\hat{\alpha})(m^*_{LD})^2$$
$$+ \hat{\alpha}M^2 T\left(\frac{\hat{\gamma}M}{\hat{\alpha}T} - 2\hat{\alpha} + 3\hat{\alpha}^2 + \hat{\gamma}\right)m^*_{LD} + \hat{\alpha}M^3 T(\hat{\alpha} - \hat{\alpha}^2 - \hat{\gamma}) \ . \tag{II.34}$$

This Equation yields solutions for m^*_{LD}; L^*_{LD} then follows as $L^*_{LD} = m^*_{LD}/\alpha^*_{LD}$. A third order polynomial such as Eq. (II.34) has at least one real root, but it may have three real roots; we can distinguish between these cases by computing the sign of the discriminant. In this way we find that if $\gamma_0/\alpha_0 \geq 1/3$, there is only a single solution m^*_{LD}. In contrast, for $\gamma_0/\alpha_0 < 1/3$, which will be discussed in detail later, this Equation yields three different stationary states. We will discuss both cases separately, see Secs. 7.5.4 and 7.5.7.

7.5. Construction of the phase diagram

With the steady state properties of the MT characterized for all phases, we are now in a position to find the parameters for which these phases are physically possible. The goal of these considerations will be to obtain the phase diagrams, which is shown in Figs. II.29 and II.30. Hereby, we will follow the strategy explained in Sec. 7.4.1.

A convenient way of constraining the respective phases is in the space of the parameters $\hat{\alpha}$ and $\hat{\gamma}$. This is because once the injection rate of motors per motor concentration α_0, and the MT elongation rate per tubulin concentration γ_0 is specified, moving along the axes of the phase diagram corresponds to changing these concentrations, which are natural control parameters in an experimental setup such as the one presented in Chap. 6.

7.5.1. High density phase

We know from the TASEP that the collective dynamics of particles fall into the HD phase if $\beta < \alpha$ and $\beta < 1/2$. It was concluded in Sec. 7.4 that the MT model can effectively be described by a TASEP if a corresponding choice of parameters is made, and in particular $\beta = \delta$, as well as $\alpha = \alpha^*$. For the HD phase, we have computed the motor injection rate at the stationary state α^*_{HD} in Eq. (II.29). As a result, following the strategy described in Sec. 7.4.1, it must be ensured that $\delta < \alpha^*_{\mathrm{HD}}$, as well as $\delta < 1/2$.

The first condition $\delta < \alpha^*_{\mathrm{HD}}$ reduces to

$$\hat{\gamma} < \delta(1 - \delta) - \frac{\delta - \hat{\alpha}}{1 - \delta}\frac{\gamma_0}{\alpha_0} \ . \tag{II.35}$$

Remarkably, this inequation depends only on the ratio of the elongation and injection rate per concentration. Because $\beta = \delta$, the second condition reduces to $\delta < 1/2$.

7.5.2. Maximal current phase

With the above equations and the correspondence of the MT model and the TASEP, we have to ensure the necessary condition for the MC phase $\alpha^*_{\mathrm{MC}} > 1/2$, which reduces to

$$\hat{\gamma} < \frac{1}{4} + (2\hat{\alpha} - 1)\frac{\gamma_0}{\alpha_0} \ . \tag{II.36}$$

Also Eq. (II.36) depends only on the ratio of the two concentration dependent rates γ_0 and α_0 and not on them separately.

The second condition for the presence of the MC phase is that $\beta = \delta > 1/2$. Note that this condition is complementary to the constraint for the HD phase. As a result, MC and HD phase are disjoint, and drawn in the space of the injection and elongation rates $\hat{\alpha}$ and $\hat{\gamma}$, no phase diagram can contain both phases.

7.5.3. Shock phase

For the SP, the TASEP condition $\alpha = \beta$, corresponding to $\alpha^*_{\mathrm{SP}} = \delta$ is met by construction, because it is condition for the derivation of the position of the DW, x^*_w, see Sec. 7.4.4. An essential constraint is however imposed by requiring that $0 < x^*_w < L^*_{\mathrm{SP}}$, i.e., that the DW is actually located in the lattice bulk and not at (or beyond) one of its boundaries. What happens in the limits $x^*_w = 0$ or $x^*_w = L^*_{\mathrm{SP}}$, i.e., when the DW reaches one of the tips? Assuming $x^*_w = 0$, this would imply that the high motor density emanating from the plus end spreads over the complete lattice; this is exactly the behavior of the HD phase. In fact, the condition $0 \leq x^*_w$ reduces the opposite of Eq. (II.35), such that a condition for the SP is that $\hat{\gamma}$ must exceed the value obtained from the right hand side in this equation; as a result, the SP and HD phase bear a common transition line.

Also the second limit, where we require $x^*_w \geq L^*_{\mathrm{SP}}$, can be utilized to find a phase transition: Here, the low density extends over the complete MT. In the same way as for the transition line between the HD phase and the SP, this limit seems to give rise to the transition where the SP

ceases to exist and turns into the LD phase instead. While we will discuss the subtleties of this interpretations in Sec. 7.5.7, the reduction of the condition $x_w^* < L_{SP}^*$ can be done right away, and it yields a second constraint for the SP:

$$\hat{\gamma} < \delta - \delta^2 - \frac{\gamma_0}{\alpha_0}\left(1 + \frac{\hat{\alpha}}{\delta}\right) =: f_\delta(\hat{\alpha}) \,. \tag{II.37}$$

In the same way as demonstrated for the HD phase in Sec. 7.5.1, a second condition for the SP is given by $\beta = \delta < 1/2$.

7.5.4. Low density phase, case $\gamma_0/\alpha_0 \geq 1/3$

We now turn to the restriction of the parameter regime in which the dynamics of motors on a MT fall into the LD phase. Similar to the consideration of the other phases in the previous Sections, this amounts to verifying the conditions $\alpha_{LD}^* < \delta$ and $\alpha_{LD}^* < 1/2$. In contrast to the simple equations obtained for all other phases, the stationary state properties for the LD phase rely on finding roots of a third order polynomial, Eq. (II.34), and their form is therefore complex. In fact, even with the help of powerful symbolic computational programs such as *Mathematica*, a direct reduction of the conditions is impossible, such that a comparison of α_{LD}^* and δ is only possible numerically.

In order to analytically constrain the LD phase, we therefore employ an argument based on a result obtained earlier: Here, we found that the SP ceases to exist and turns into the HD phase as the DW is found at the left lattice end. In the opposite limit, leading to Eq. (II.37), the low density extends over the whole lattice. This suggests that along the transition line $f_\delta(\hat{\alpha})$, defined in this Equation, the SP turns into a LD phase.

In fact, we find by direct comparison of the regime constrained in this way with the numerically reduced conditions for the LD phase that both methods lead to the same domains in which the LD phase is possible, as long as $\gamma_0/\alpha_0 \geq 1/3$. Hence, $\hat{\gamma} > f_\delta(\hat{\alpha})$ is a necessary condition for the LD phase in this limit.

For the opposite case, when $\gamma_0/\alpha_0 < 1/3$, we will show later that subtle care has to be taken, cf. Sec. 7.5.7 and Fig. II.32.

7.5.5. "$L = 0$" phase

As different phases are considered, it is advisable to critically ask what the physical concept behind a "phase" is. Essentially, we hereby group parameters for which the model shows similar collective dynamics. However, this also implies that the distinction between phases becomes meaningless as the lattice shrinks and its length eventually vanishes completely: In what phase is a MT with length zero? The only answer can be to explicitly restrict the parameter domain in which the MT length vanishes, which can be done with the steady state quantities obtained in Sec. 7.4 [4]. For the HD phase, the domain of vanishing MT length is bounded by $\hat{\gamma} < \delta(1 - \delta)$, cf. Eq. (II.28); the

---

[4]Of course it has to be critically verified whether a field-theoretical treatment of a lattice gas model remains a good approximation for very short lattices. For the present purpose to constrain the region in which the MT shrinks to zero length, our numerical simulations reveal good agreement with the transition lines obtained theoretically. This hence provides an a posteriori justification of the mean field assumptions.

corresponding constraint for the MC phase is given by $\hat{\gamma} < 1/4$, see Eq. (II.31). For the case of the LD phase, the parameters along which the stationary length vanishes can be found by setting $m^*_{\mathrm{LD}} \to 0$ in Eq. (II.34), which implies that $L^*_{\mathrm{LD}} = 0$ as $\hat{\gamma} = \hat{\alpha}(1 - \hat{\alpha})$. For a polymerization rate smaller than this, the MT at the stationary state is completely depolymerized.

7.5.6. The phase diagram for $\gamma_0/\alpha_0 \geq 1/3$

Having found constraints for the extension of all different phases, we may now summarize our findings in a phase diagram. Interestingly, we find that all transition lines computed in the previous Sections depend on the ratio γ_0/α_0 only and not on these parameters separately. As a consequence, only two parameters, the depolymerization rate δ and the ratio γ_0/α_0 have to be specified in order to depict the the phase diagram. We will first concentrate on the case $\gamma_0/\alpha_0 \geq 1/3$ to which our previous discussion of the LD phase was limited.

For an exemplary ratio $\gamma_0/\alpha_0 = 1$ and two different values of δ, the resulting phase diagram is shown in Figs. II.29–II.30 along with the phases' most characteristic quantities. Here, the theoretically predicted transition lines as they were derived in Secs. 7.5.1–7.5.5 are shown in red. In Fig. II.29, the value of the depolymerization rate is $\delta = 0.3$, in Fig. II.30, this parameter is chosen as $\delta = 0.7$. Fig. II.29a shows the difference of the injection and ejection rate at stationarity, $\alpha^* - \delta$, as obtained from simulations. In the North West part, we observe $\alpha^* < \delta$ as expected for the LD phase predicted for this regime; in the North East part the opposite is true: here, $\delta < \alpha^*$, in agreement with the behavior of the HD phase. By contrast, in between these domains (SP), both rates are equal, $\alpha^* = \delta$, implying that a domain wall separates the coexisting regions of low and high motor density in this case. Fig. II.29b shows the stationary state length for the same parameters: In the bottom part ($L = 0$), the MT is completely depolymerized. Fig. II.29c summarizes these four phases. The phase transition lines agree excellently with the transitions apparent from the characteristic quantities in Figure parts II.29a and II.29b. Fig. II.29d shows cuts through the diagrams II.29a–II.29b for the respective quantities, at the parameters indicated with symbols. Here, blue lines show results obtained from theoretical calculations, whereas dots indicate measurements from simulations. Once more, this Figure stresses the good agreement of simulation data and theoretical results.

Fig. II.30a shows the average motor density on the MT for a larger value of $\delta = 0.7$ at the same ratio of the concentration-dependent rates as before. While the average density is small in the LD phase in the left part of the Figure, its value equals $1/2$ in the MC phase irrespective of the precise value of $\hat{\alpha}$ and $\hat{\gamma}$, as expected. Also the description of the MC phase is accurate, which is emphasized in Fig. II.30b.

We conclude that for a relatively large ratio of the concentration-dependent rates $\gamma_0/\alpha_0 > 1/3$, we find five different phases which occupy distinct domains in the space of the parameters α and γ: The LD and HD phase where the motor density is constantly low or high, respectively, the SP where low and high motor density coexist, the MC phase, where the motor density equals $1/2$, and the "$L = 0$" phase where the MT completely depolymerizes.
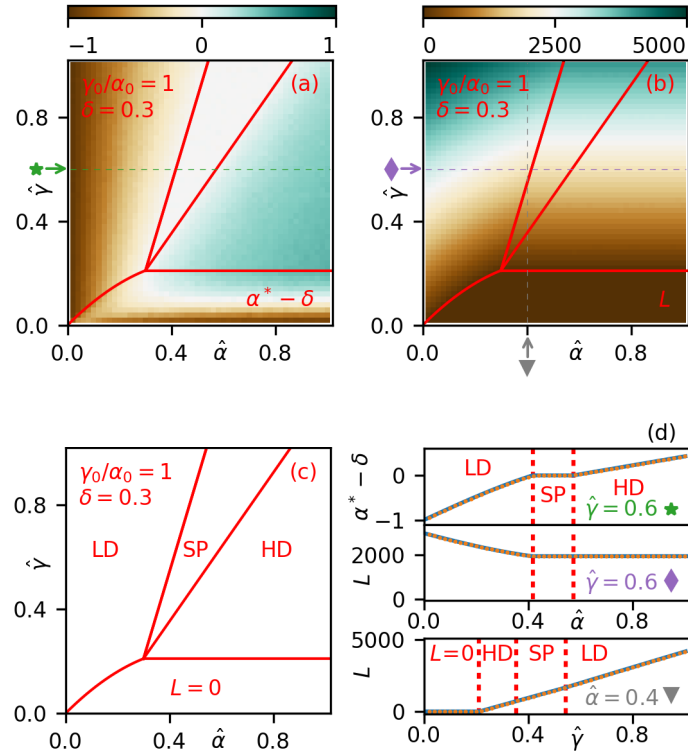
Figure II.29.: *Phase diagram and comparison of simulation data with theoretical calculations for $\gamma_0/\alpha_0 = 1$ and $\delta = 0.3$. For the simulation data in part (a)–(b), $\hat{\gamma}$ is normalized in a way such that $\hat{\gamma} = 1$ corresponds to 5000 available tubulin dimers in the system. Part (a) shows the difference of the injection rate at stationarity, α^*, and the ejection rate δ in the color code, as obtained from simulations. In the top left part, $\alpha^* < \delta$, in the center $\alpha^* = \delta$, and on the right side $\alpha^* > \delta$. These three cases are characteristic for the LD phase, SP, and HD phase, respectively, see part (c). The phase transition lines, obtained from the theoretical mean-field calculations, which are shown in red lines, confine the domains obtained in this way to good accuracy. Panel (b) shows the stationary state length L^* which is obtained from simulations. In the bottom part, the length vanishes, i.e., the MT is completely depolymerized. Part (c) summarizes these findings in a phase diagram. Part (d) in detail compares the theoretical predictions (lines) of the difference of injection and ejection rate, as well as the MT length, with simulation data (points) for all phases.*
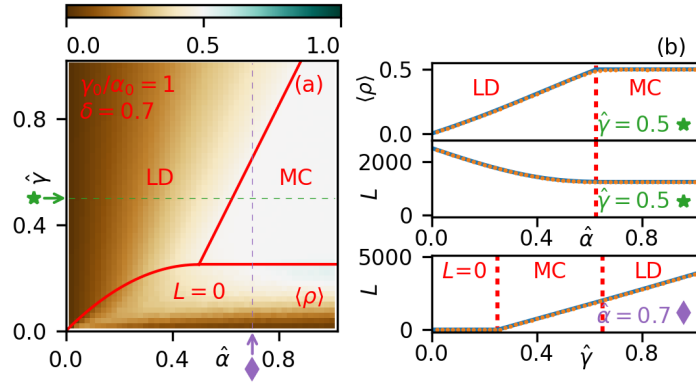
Figure II.30.: Phase diagram for $\gamma_0/\alpha_0 = 1$ and $\delta = 0.7$. (a) The average density is shown which is small in the LD phase, and equals $1/2$ in the MC phase. In the bottom part, the MT length vanishes, cf. Fig. II.29b. Part (d) reveals that simulation results (dots) agree well with theoretical calculations (lines) for the average density and the steady state length at the parameters as indicated by symbols.
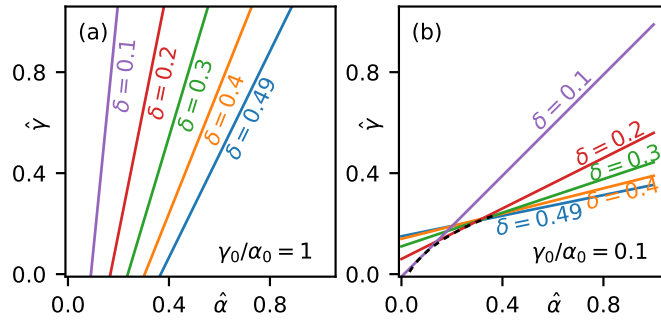
Figure II.31.: The SP-LD transition line $f_\delta(\hat{\alpha})$, as obtained in the limit $x_w^* = L_{SP}^*$ for two different ratios γ_0/α_0, and several values of δ. For a relatively large ratio γ_0/α_0, as shown in part (a), decreasing δ shrinks the domain above the respective transition line. By contrast, part (b), for a small ratio, decreasing δ leads to an additional space above the transition line in the left bottom of the diagram. For more detailed discussions, see the main text.

7.5.7. Low density phase, case $\gamma_0/\alpha_0 < 1/3$

When we derived the extension of the LD phase in parameter space in Sec. 7.5.4, we invoked the limit $x_w^* = L_{SP}^*$ of the SP which led to the transition line $f_\delta(\hat{\alpha})$. It was argued that in this limit the low motor density extends over the complete MT lattice; assuming a continuous transition between the LD phase and the SP, the end of the SP would therefore mark the beginning of the LD phase. This argument is valid in the limit considered so far, as a comparison with the direct numerical reduction of the conditions for the LD phase, as well as with simulation data reveals. However, a subtlety was concealed previously which becomes important as $\gamma_0/\alpha_0 < 1/3$. Let us assume that the motors on a MT with ejection rate δ' are in the LD phase. As a consequence, given this parameter, the condition $\alpha_{LD}^* < \delta'$ is met. On increasing δ beyond δ', α_{LD}^* does not change, cf. Eq. (II.33), such that $\alpha_{LD}^* < \delta$ is also true for all $\delta > \delta'$. In conclusion, if a system is in the LD phase for δ', it is also in the LD phase for all $\delta > \delta'$. The extension of the LD phase for a given value of δ can therefore be obtained as the union of all regions above the transition lines $f_{\delta'}(\hat{\alpha})$ for all $\delta' < \delta$, i.e.

$$\hat{\gamma} > \bigcup_{\delta' < \delta} \{\hat{\gamma} > f_{\delta'}(\hat{\alpha})\} . \tag{II.38}$$

In order to make this more explicit we revisit the case $\gamma_0/\alpha_0 \geq 1/3$, for which we concluded in Sec. 7.5.4 that the phase boundary of the LD phase is identical to that of the SP. Fig. II.31a shows the function $f_\delta(\hat{\alpha})$ which was found to be the transition line for this case for different values of δ and $\gamma_0/\alpha_0 = 1$. As the Figure shows, any decrease of δ also decreases the extension of the region confined left/above this line. In other words this implies that there are no points which are above this transition line for small δ, but below a transition line for larger δ, or stated mathematically, $\cup_{\delta < \delta'} \{\hat{\gamma} > f_\delta(\hat{\alpha})\} = \{\hat{\gamma} > f_{\delta'}(\hat{\alpha})\}$. For this reason, the extension of the LD phase was — in the limit of large ratios γ_0/α_0 — correctly constrained as the domain complementing the SP, see Sec. 7.5.4.

The situation is different when the ratio $\gamma_0/\alpha_0 < 1/3$. Incidentally this is the parameter regime where the polynomial Eq. (II.34), from which the steady state properties of the LD phase follow, has up to three (real) roots. Fig. II.31b shows the transition lines $f_\delta(\hat{\alpha})$ for different values of δ and $\gamma_0/\alpha_0 = 0.1$. For the displayed case, decreasing δ changes the transition line $f_\delta(\hat{\alpha})$ in a way such that there are now some points in parameter space which are below the transition line for large δ, but above the line $f_\delta(\hat{\alpha})$ for a smaller value of δ. E.g., the transition line $f_{0.4}(\hat{\alpha})$ for $\delta = 0.4$ omits the points in the bottom left of the diagram, which are well above $f_{0.1}(\hat{\alpha})$. For these parameters, the condition for the LD phase $\alpha_{LD}^* < \delta = 0.1$ is met, which is obviously still true for $\delta = 0.4$ and hence implies that these points must also be in the LD phase for $\delta = 0.4$. As a consequence, in order to find the LD region for, e.g., $\delta = 0.4$, we have to calculate the union of all regions defined in the described way for $\delta = 0.4$.

How can this union be obtained? Given specific parameters $\hat{\alpha}$ and δ', we have to find the value $\delta < \delta'$ which minimizes the transition function $f_\delta(\hat{\alpha})$, and subsequently evaluate f_δ at this point. This is done by taking the derivative with respect to δ, and finding the roots of the resulting equation. As $\hat{\alpha} > 1/27\alpha_0/\gamma_0$, only a single extremum exists (which is a maximum) that is at $\delta < 0$ and can therefore be ignored in our discussion. Conversely, if $\hat{\alpha} \leq 1/27\alpha_0/\gamma_0$, two different δ extremize $f_\delta(\hat{\alpha})$, of which the minimum is located between 0 and $1/3$. Subsequent evaluation of

$f_\delta(\hat{\alpha})$ at the minimum yields the envelope function enclosing all transition lines $f_\delta(\hat{\alpha})$, which is shown as the black dashed line in Fig. II.31b. We have thus found an analytic way how the LD phase can be constrained.

7.5.8. The phase diagram for $\gamma_0/\alpha_0 < 1/3$

Having found the domain of the LD phase for the case when the MT elongation rate per concentration is significantly smaller than the motor injection rate per concentration, $\gamma_0/\alpha_0 < 1/3$, we are now in a position to draw the phase diagram also for this case. To this end, let us recall that in the limit under consideration, the polynomial Eq. (II.34), giving rise to the LD steady state properties, yields up to three (real) solutions. We have described how to constrain one of them as the envelope of the transition function $f_\delta(\hat{\alpha})$ in the previous section. Furthermore, we have constrained the parameter region where the MT length vanishes in Sec. 7.5.5, which eliminates a second solution for the LD phase. Therefore, we are left with the consideration of the third LD phase obtained from Eq. (II.34).

To this end, let us examine the rate of change of MT length, $\partial_t L$, in the case where the length becomes stationary at three different values. Here, we assume that — even out of the stationary state — the motor density is constant along the lattice and its value is determined by the injection rate α. This is true as long as the MT length changes slowly compared to the motor dynamics. Fig. II.32a shows $\partial_t L$ in this limit, as obtained from Eq. (II.26a). We find that the slope of $\partial_t L$ is positive for the intermediate zero, which implies that small fluctuations about this steady state are amplified: This state is unstable. Furthermore, we observe that of the extreme zeroes, which are the stable fixed points, one is at long length, while the other is at negative length (which signifies a completely depolymerized MT). We now have to distinguish between two different cases: If the intermediate (unstable) stationary state is at small but positive length (blue line in Fig. II.32a, corresponding to the parameters marked by an asterisk in Fig. II.32b), MTs which are shorter than this length are attracted towards the lower fixed point (i.e., the completely depolymerized MT), while all MTs longer than the unstable fixed point are likely to end at long length. In contrast, if the intermediate, unstable, length is at negative (or zero) length, see the yellow line marked by a diamond in Fig. II.32a–II.32b, even very short MTs are in the basin of attraction of the long length.

From Eq. (II.34), we have concluded in Sec. 7.5.5 that $L_{\mathrm{LD}}^* = 0$ along the line $\hat{\gamma} = \hat{\alpha}(1 - \hat{\alpha})$, see the dashed line in Fig. II.32b. Fig. II.32a reveals that for parameters inside (blue asterisk) and outside (yellow diamond) of this domain, shown in Fig. 8(a), it is the intermediate, unstable, LD steady state length which switches sign. More specifically, the unstable LD state features a positive length only if $\hat{\gamma} < \hat{\alpha}(1 - \hat{\alpha})$. As a consequence, in this domain two stable stationary states can be reached; in the opposite case, the MT will always end in the long LD state.

Concluding these considerations for the limit of small ratios γ_0/α_0, we summarize our findings in a phase diagram, Fig. II.32c. For $\delta = 0.3$ and $\gamma_0/\alpha_0 = 1/40$ in this Figure, we recover the well-known phases which we had obtained earlier for a larger ratio, Sec. 7.5.6. Furthermore, we find that the LD phase overlaps with the "$L = 0$" domain, the HD phase, and the SP. In the overlapping region, the system behaves bistable. This means that depending on the initial lattice length, the system will become stationary at one of the two stable steady states. Fig. II.32d shows a parameter scan of the steady state length, where $\hat{\alpha}$ and $\hat{\gamma}$ are chosen as control parameters in the same way as before. Here, MTs are initially short (top panel), or long (bottom panel). In fact, the MT length
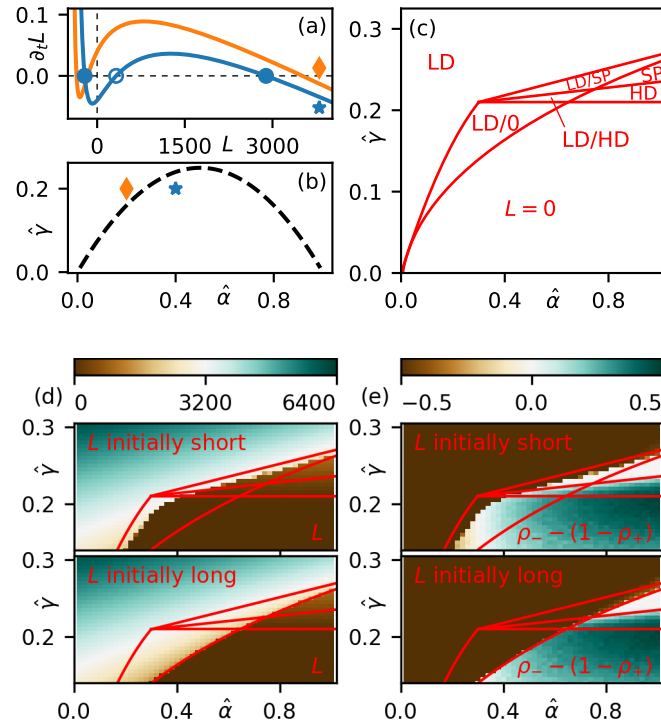
Figure II.32.: The phase diagram for small γ_0/α_0, here $\gamma_0/\alpha_0 = 1/40$ and $\delta = 0.3$. (a) For two different parameters, the rate of change of the lattice length, $\partial_t L$ is shown. The length becomes stationary at three values. Due to the positive slope of $\partial_t L$ at the intermediate length, this state is unstable. Depending on the location outside (diamond) and inside (asterisk) the domain $\hat{\gamma} < \hat{\alpha}(1 - \hat{\alpha})$, marked in dashed lines in part (b), the intermediate length is negative, or positive. As an effect, the stable fixed point at negative (i.e., completely depolymerized) length cannot, or can be reached; see the main text for a detailed discussion. (c) The resulting phase diagram. (d)–(e) For initially long or short MTs, both the steady state length (d), and the difference of steady state injection and ejection rate (e) are different in the bistable regime. In (d)–(e), the absolute value of γ_0 is chosen such that an undepleted elongation rate of $\hat{\gamma} = 0.25$ corresponds to 5000 available tubulin dimers.
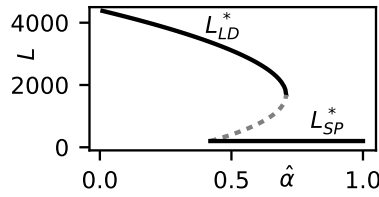
Figure II.33.: The MT length shows hysteresis. The Figure shows the steady state length L as a function of the injection rate $\hat{\alpha}$ for the parameters of Fig. II.32d, where $\hat{\gamma} = 0.22$. In the middle, two stationary states are possible, one of them in SP, the other in LD phase. Both curves are linked by an unstable solution of the LD phase (dashed line) which functions as a separatrix between the stable lengths.

at stationarity is different for these cases in the bistable domain. Fig. II.32e depicts the difference of the injection and ejection rate at the respective stationary state: For simulation runs starting from a long length (bottom panel), $\alpha^* < \delta$ throughout the bistable regime; this implies that the dynamics is in LD phase. In contrast, when L is initially short (top panel), for the two domains where the length assumes a finite stationary value we observe $\alpha^* > \delta$, and $\alpha^* = \delta$, in the domains termed LD/HD, and LD/SP, respectively. Hence, in this case, motors on an initially short MT are in a different phase as motors on an initially long lattice.

We note that the transition lines, in particular the line separating the LD phase from the LD/o phase deviates slightly from the transition which can be guessed by looking at the simulation data. The reason is that in the LD/o domain around the transition line, the unstable steady state is at very short length. Any fluctuations above this length will bring the MT into the basin of attraction of the long length, implying that although the fixed point with vanishing length is mathematically stable, its bassin can easily be left. In fact we find that simulation results and theoretical predictions agree even better for larger reservoir sizes, when the relative fluctuations become smaller.

Depending on the exact parameters γ_0/α_0 and δ, the extension of the bistable regime varies. In particular, for ratios γ_0/α_0 smaller than in Fig. II.32c, the size of the bistable phase grows, while the composition is modulated and the LD/o phase becomes increasingly popular. For $\delta > 1/2$, we also observe the existence of a LD/MC bistable phase (not shown).

We conclude that both our theoretical calculations and simulation results confirm the existence of a bistable domain. One stationary state in this domain is in the LD phase, the other steady state may be in the HD, SP, MC, or $L = 0$ phase.

7.6. Discussion

7.6.1. Bistability leads to hysteresis and makes phase transitions discontinuous

We now turn to a discussion how the MT length changes when a phase transition line is crossed. Fig. II.29b shows the steady state length L^*, scanned over the parameters $\hat{\alpha}$ and $\hat{\gamma}$, in the case $\gamma_0/\alpha_0 = 1$, which we argued is the regime where the dynamics are monostable. We find that the steady state length changes smoothly, i.e., continuously, along the complete diagram. In particular, this applies also when transition lines are crossed, see also Fig. II.29d. The situation is different

for $\gamma_0/\alpha_0 < 1/3$ which is the parameter range where the phase diagram includes bistable phases. As Fig. II.32d reveals, the steady state length may change discontinuously on crossing a transition line. This is stressed also in Fig. II.33 which cuts through the diagram Fig. II.32c at $\hat{\gamma} = 0.22$. The steady state length for small and large values of $\hat{\alpha}$ is given by L^*_{LD} and $L^*_{\text{SP}} = L^*_{\text{HD}}$, respectively; in the middle, for intermediate $\hat{\alpha}$, both these branches coexist (i.e., the length is bistable here). However, L^*_{SP} and L^*_{LD} do match continuously. In contrast, a third solution, drawn as a dashed gray line, links L^*_{LD} and L^*_{SP}. This branch is the unstable LD steady state discussed in Fig. II.32a, which follows from Eq. (II.34). As a consequence, if an originally small $\hat{\alpha}$ is increased to $\hat{\alpha} \sim 0.7$ in Fig. II.33, e.g., due to the increase of the motor concentration, an initially long MT will be forced to shrink to a much shorter length L^*_{SP}. When, subsequently, the injection rate $\hat{\alpha}$ drops, the MT will remain at this short length until $\hat{\alpha} \sim 0.42$ before the short stationary length vanishes and the MT is bound to become long again. This does not only define a hysteresis cycle but also stresses a crucial difference between the monostable and bistable phase diagrams: Bistability makes phase transitions discontinuous (205).

This raises the question whether the restriction of the domain in which the dynamics are in the LD phase, Sec. 7.5.4 and 7.5.7, was done in a correct way: Here, the implicit assumption was that wherever the SP ceases, obtained from the limit $x^*_w = L^*_{\text{SP}}$ where the low density emanating from the minus end spreads over the complete lattice, it should *continuously* become a LD phase. Now that we found that L^* changes discontinuously between the SP and the LD phase in the case of bistability, this argument seems to break down. However, the unstable LD steady state solution obtained from Eq. (II.34), which is shown linking the different branches of L in Fig. II.33 rescues our argument: This branch approaches both L^*_{SP} and L^*_{LD} continuously. Even though this stationary state is unstable, this implies that as $x^*_w = L^*_{\text{SP}}$, an (unstable) LD phase is defined. This unstable length, equal to the (stable) SP length, functions as a separatrix between the stable lengths, and thus MTs at the transition point which are, due to stochastic fluctuations, slightly longer than L^*_{SP} will be driven towards the long length L^*_{LD}. We conclude that, the argument used for constraining the LD phase is true even for the bistable regime where phase transitions may be discontinuous.

7.6.2. The limit in which we observe bistability is biologically relevant

Before concluding this work, we would like to make another, more heuristic, argument how bistability can be understood: We find that a bistable regime exists for $\gamma_0/\alpha_0 \ll 1$, and typically in a region where $\hat{\gamma}$ and $\hat{\alpha}$ are comparable. Because $M/T = \gamma_0/\alpha_0\, \hat{\alpha}/\hat{\gamma}$, we have $M \ll T$ in the bistable regime, i.e. much less motors than tubulin dimers are available in the reservoir. In this limit, consider on one hand a MT which is so short that it can carry only a very small number of motors compared to the total number of motors in the reservoir, $m \approx L \ll M$. Then, since nearly all motors are left in the reservoir, the resulting injection rate of motors is relatively high ($\alpha \approx \hat{\alpha}$), allowing for a relatively high motor density on the MT which also leads to a high number of motors at the tip which can catalyze MT shrinkage. Thus, the (originally short) MT will rather shrink, such that it will likely remain at a short length. On the other hand, consider a slightly longer MT which is still so short that the number of tubulin dimers bound to it is small compared to the total number of tubulins, but so long that the number of motors on it significantly depletes the free motor reservoir; in other words, $m \approx M \approx L \ll T$. In this case, the polymerization speed

is still nearly unaffected, $\gamma \approx \hat{\gamma}$, but the motor injection rate is crucially smaller, $\alpha \ll \hat{\alpha}$. Thus, only very few motors enter the MT, and as a consequence their presence at the plus end cannot balance polymerization. Hence, the MT will tend to grow until also the tubulin reservoir is depleted. Because initially short MTs will therefore shrink further and long MTs are likely to grow, the system is bistable in this limit.

Interestingly, the limit $M \ll T$, which corresponds to $c_m \ll c_T$, is the limit which is relevant both in physiological environments *in vivo*, as well as in *in vitro* experiments. Ghaemmaghami et al. have measured the abundance of both kinesin-8 Kip3 and tubulin by creating an *S. cerevisiae* fusion library (212). While they found that in a yeast cell there are only $\sim$ 700 motor molecules, several 10000 tubulin dimers are available. The same limit of small motor concentrations was also used in the *in vitro* experiment presented in Chap. 6, for which bimodal MT length distributions — corresponding to bistable length regulation — were found. We conclude that bistability is not only a theoretical artifact of limited resources, but its implications are also important for *in vitro* setups, and potentially even the biological function of MTs and cells.

7.7. Conclusion

In this Chapter we have in detail considered a lattice gas model describing a length regulation mechanism of MTs. The antagonistic actions of motor-induced MT depolymerization and spontaneous lattice polymerization rely on particles from finite reservoirs. We have concluded that finite resources lead to modified motor density profiles on the MT, and in particular to the emergence of domain walls on the lattice, where the motor density shows a sudden increase. Furthermore, we have demonstrated that in a well-characterized limit two stationary states coexist such that the system is bistable. Remarkably, phase transitions become discontinuous in the case of bistability, while the steady state MT length changes continuously for monostable conditions. We have demonstrated that a phase transition can be caused, e.g., by the change of concentrations of one of the involved proteins. Findings of this kind may have various implications for intracellular behavior where protein concentrations are known to change, and sudden transitions, e.g. during anaphase, are observed.

Part III.

Motor-induced unbinding: the role of interactions for the collective dynamics of molecular motors

8. Introduction

8.1. Motivation

The collective motion of molecular motors on microtubules (MTs) and their interactions with each other are highly complex processes that underlie important intracellular functions. For example, motors of the kinesin-8 family use MTs as molecular tracks along which they perform directed transport (20, 198). Having arrived at the MT end, these motors influence the depolymerisation dynamics at this point, and thus have an effect on MT length (2, 20, 21, 23) and spindle size (126, 127), properties whose tight regulation is crucial for the normal operation of a cell (188).

Kinesin-1 was the first kinesin to be discovered (213), and it is arguably the motor which has been studied in greatest detail. Kinesin-1 is a versatile cargo transporter (214) which uses its two heads (29) to processively walk towards the plus-end of a MT. In the crowded environment of a typical cell, molecular motors and MT-associated proteins (215) compete for a limited number of binding sites on the MTs. As a consequence, "traffic jams" consisting of molecular motors may develop on (parts of) the MT (132, 133).

A central question is how motors interact with each other in crowded situations like this, and how motors affect each other's ability to bind to and detach from MTs. Several studies have reported (apparently) conflicting results relating to these issues: Thus, Vilfan et al. (31) observed that kinesin motors primarily bind near other motors. Similarly, Muto et al. (216) observed long-range cooperative binding, and Roos et al. (217) discovered that the dwell time of motors increases when they are in the proximity of other motors on the MT. In contrast, Leduc et al. (132) found a reduction in the dwell time of kinesin-8 motors on crowded filaments, in agreement with *in vitro* measurements of kinesin-1 carried out by Telley et al. (30).

How can these findings be reconciled? Firstly, we note that interactions may differ depending on whether motors are mobile (30, 132) or have been immobilized by genetic engineering (31, 217): It appears that an increased dwell time of motors on the MT or cooperative attachment to a MT is primarily found for immobile motors, while mobile motors experience no, or at least less attractive interactions. A second differentiator of these studies was pointed out by Telley et al. (30) who found that the label used to visualise motors by fluorescence microscopy can be crucial. In particular, when these authors failed to reproduce their own earlier results (105) for the crowding behaviour of kinesin-1 using a different label, they concluded that extensive labelling or the use of large labels may lead to non-specific interactions between motors. Therefore, attractive potentials may develop which hold motors on the MT.

To minimise these potential effects, Telley et al. removed parts of kinesin's tail (104), such that the motor could still walk with wild-type characteristics (105), and attached a GFP label to only a small proportion of the motors, leaving the vast majority of kinesin motors unlabelled (30). As a consequence, when they varied the abundance of kinesin, they found that this motor's dwell

time was inversely related to its (volume) concentration. In our understanding, the situation considered in this study by Telley et al. (30) is closest to the behaviour in an actual cell. Hence, in our theoretical analysis we will mainly compare our results with their data.

The Totally Asymmetric Simple Exclusion Process with Langmuir Kinetics (TASEP/LK) (154–156) is commonly employed to describe the collective dynamics of motors on a MT. In this stochastic lattice gas model, motors are described as particles on a one-dimensional lattice (a protofilament of a MT) and step stochastically towards the lattice end. This approach has successfully predicted (155, 156) the existence of traffic jams and domain walls, which were recently observed in experiments (132, 133). Several variations of this stochastic process have considered specific properties of motors, such as their longitudinal (218) or lateral (170) extension. Furthermore, additional interactions of motors with each other have been examined (178, 219, 220). Among them are so-called mutually interactive Langmuir kinetics (179, 180, 221), where binding and unbinding of monomeric particles are directly influenced by the occupation of the nearest-neighbour binding sites. Most of these studies concentrated on fundamental physical properties of the dynamics of motors, such as the different phases of their collective motion. Consequently, the impact of motor-motor interactions on experimentally accessible quantities, such as the motor run length, dwell time, velocity or their numbers of landings (initial attachments) on the lattice per unit length and time, was usually not considered.

In this study, we theoretically examine a model which includes motor-motor interactions and a dimeric driven lattice gas. Our aim is to describe the collective motion of processive molecular motors, such as kinesin-1, along a MT. We find that a simple, motor-induced detachment mechanism suffices to quantitatively account for the experimental measurements reported by Telley et al. (30). By developing a mean-field theory, we explore in detail the dependence of motor dwell time, run length, velocity, and landing rate on the volume concentration of kinesin. Furthermore, we find that stochastic pausing of motors on the MT is significantly enhanced by crowding and leads to short-lived traffic jams on the MT, thus recovering the long and frequent periods of interrupted motor motion observed in experiments (30). By comparing the rates of spontaneous detachment and motor-induced detachment from the MT, we gain insight into the stepping cycle of kinesin-1, and find that this motor spends a significant fraction ($\sim 22\%$) of its stepping cycle in a weakly bound state.

The results of the present study have been submitted for publication to *Biophysical Journal*, and are preprinted under the title "Crowding and pausing strongly affect dynamics of kinesin-1 motors along microtubules" as *arXiv:1805.03432* (3).

8.2. Methods

8.2.1. Monte Carlo simulations

We simulate our stochastic lattice gas model with Gillespie's algorithm (201), which provides a way of exactly modelling stochastic processes. In the first step, all possible events are collected and statistically weighed with their rates, and an event is randomly chosen out of the resulting vector. Another random number is drawn from an exponential distribution with the total rate (i.e., the sum of the rates of all possible events) as the decay parameter, in order to obtain the update time.

Subsequently, all rates are updated and the algorithm starts over. In order to account for the long length of MTs compared to the motors' run length (on the order of 100 steps), periodic boundary conditions were employed on a lattice with 2000 sites.

8.2.2. Fitting analytical results to experimental data

For the four sets of quantities measured experimentally (30), namely run length, dwell time, velocity, and landing rate of kinesin motors, analytic equations were obtained, see Eqs. (III.11)–(III.14). The parameters v (hopping rate of motors) and ω_D (their detachment rate) were obtained from the experimental data (30) at low concentrations, as well as the landing rate λ_0 of normalised concentration of motors to the MT. In order to obtain the remaining parameters ω_A and θ, the analytic results were taken at the concentrations tested in experiments, and the deviations from experimental data were weighed by the experimental standard error (30). Subsequently, the sum of the squared weighed errors was taken, and minimized with *Mathematica*'s NMinimize function. In this way, the global fit values ω_D and θ are found, see Eq. (III.18).

8.3. Model description

We wish to analyse the stochastic motion of kinesin-1 motor molecules on MTs. Kinesin-1 is a dimer with two heads (29) that can bind to distinct binding sites (50) on two neighbouring tubulin dimers (111). Powered by the hydrolysis of ATP (112), it moves processively and unidirectionally (222) towards the MT's plus-end (5) along a protofilament (108, 223). It walks hand-over-hand (111), which implies that the rear (lagging) head steps over the front (leading) head to the next binding site in order to complete a step.

To describe the collective dynamics of kinesin-1 motors on protofilaments, we employ a one-dimensional lattice gas model as illustrated in Fig. III.1, where the fluid surrounding the MT can be considered as a homogeneous and constant reservoir of motors with concentration c. The corresponding mathematical model is based on the Totally Asymmetric Simple Exclusion Process with Langmuir Kinetics (TASEP/LK) (155, 156). Here, we extend it to include the dimeric nature of kinesin-1, and consider an additional interaction which accounts for the enhanced detachment of neighbouring motors. To accommodate the extended size of kinesin, and to allow us to adopt simple stepping rules, each motor is described as a rigid particle which simultaneously occupies two sites of a one-dimensional lattice (218). The directed motion of motors is modelled as a stepwise stochastic hopping process with rate v (Poisson process) towards the plus-end (*totally asymmetric*); stepping is possible only if the target site is not occupied by another motor (*exclusion*). In the limit of low coverage of a protofilament, each motor would then move at an average speed $v_0 = va$, where $a = 8.4$ nm (51) is the size of a tubulin heterodimer. Motors from the reservoir can attach to the protofilament lattice at rate ω_A at locations where two adjacent lattice sites are empty. This rate depends on the volume concentration of motors as $\omega_A = \omega_a c$ with a constant ω_a.

There are two pathways that may lead to the detachment of motors from a protofilament. Firstly, motors may detach spontaneously at a rate ω_D. Because this alone cannot explain the decrease in motor dwell time on crowded filaments (30), we secondly assume that motors interact
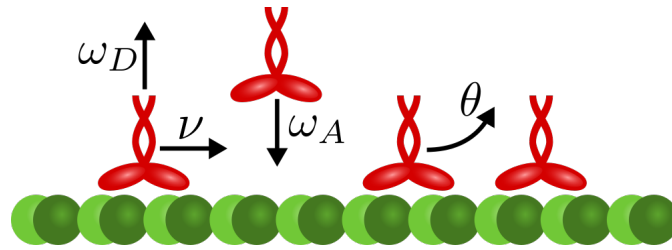
Figure III.1.: Lattice gas model for the collective dynamics of kinesin-1 motor proteins moving along a protofilament of a microtubule (MT). Motors are modelled as dimers that simultaneously occupy two neighbouring lattice sites, and advance unidirectionally towards the plus-end (right) of a protofilament at a rate ν (Poisson stepper), if no other motor occupies the next binding site (exclusion process). Kinesin-1 is also assumed to randomly bind to and detach from the protofilament at rates ω_A and ω_D, respectively. Due to steric exclusion binding is possible only if two adjacent binding sites are empty. In addition to spontaneous detachment with rate ω_D, we also account for facilitated detachment of motors that are immediate neighbours. For specificity, we assume that the dissociation rate of the rear motor, i.e., the motor closer to the minus-end (left) is enhanced by a rate θ.

with each other via a process that enhances the detachment rate of motors which are immediate neighbours. Specifically, when two motors meet, we assume that the *rear* motor's unbinding rate is enhanced by an additional rate θ; the trailing motor therefore "bounces off" the leading motor, which is consistent with experiments showing that when kinesin runs into an obstacle on the MT, the motor (and not the obstacle) is likely to detach (30, 109). The opposite case, where the trailing motor "kicks" the leading motor off the filament, leads to the same phenomena. Alternative scenarios, e.g., enhanced detachment of both motors, have been examined in Ref. (179).

9. Theoretical analysis

9.1. Simulation results

Two central quantities that characterise the collective transport of kinesin-1 along MTs are the motor density ρ and the motor current j. In general, both quantities depend on the position along the MT. At the minus-end, the density is expected to show an initial (approximately) linear increase towards a Langmuir plateau due to an "antenna effect" (132, 155, 156): This gradient arises from the combined effects of random motor attachment to and detachment from the MT, as well as driven transport along it; the slope of the initial increase is proportional to the attachment rate ω_A. Similarly, a density gradient can also be found at the MT's plus-end, in particular for motors which remain bound at this tip for an extended time. Molecular motors with this property include kinesin-8 (132) and kinesin-4 (133); to the best of our knowledge, no such behaviour has been reported for kinesin-1. Due to (potential) gradients at the MT's ends, it is generally difficult to determine the full quantitative behaviour of the motor density (179, 218). One particular property of kinesin-1, the motor in which we are primarily interested in this study, allows for a significant simplification in this respect: its run length (on the order of $1\,\mu\text{m}$ (30)) is significantly less than the length of typical MTs (usually several μm (202)). For this reason, the extent of the gradient region is small relative to the MT length, and the density profile is for the most part spatially uniform on the MT for this motor. By assuming a very long lattice and/or periodic boundary conditions (see Appendix), one can dispense with the specification of the boundary processes.

Figures III.2a and III.2b show the bulk density ρ and current j, respectively, as obtained from stochastic simulations using Gillespie's algorithm (201), see Methods. We find that the additional detachment of motors facilitated by the interaction between neighbouring motors leads to a monotonic decrease in the bulk density (Fig. III.2a) with increasing rate θ; in the limit $\theta = 0$, we recover previous results (218). Interestingly, the motor current shows non-monotonic behaviour as a function of θ (Fig. III.2b). There is an optimal value of θ at which the current is maximal. This can be understood in terms of the ability of motor-induced detachment to remove motors from very crowded MTs. Here, the flow of motors is suboptimal due to the emergence of traffic jams, as in the case of vehicular traffic (148). A decrease in the motor density may therefore enhance the numbers of motors transported along the MT per unit time. We will see later that the existence of a maximum motor current follows naturally from the non-monotonic current-density relation, Eq. (III.10). As an aside, one may thus speculate that motor-induced detachment may serve to optimise cargo transport along MTs by reducing crowding.

In this work, we are mainly interested in examining the collective dynamics of kinesin-1 (213). In experiments, such as those in the study of Telley et al. (30), its collective motion has been characterised in terms of run length on the MT l, dwell time τ, velocity V, and the rate λ (the number of motor landings on the MT per unit time and length). All of these quantities may

motor density ρ motor current j [v]
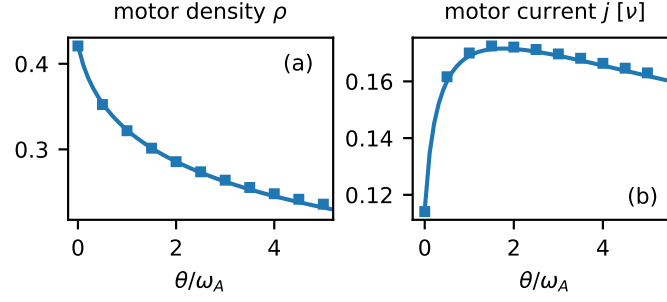
Figure III.2.: Bulk motor density and current. Symbols show data obtained from stochastic simulations, the lines depict the results of the mean-field analysis, cf. Eqs. (III.8) and (III.10) for parameters $\omega_A = 0.01v$ and $\omega_D = \omega_A/10$. (a) The interaction-induced unbinding mechanism reduces the motor density ρ. (b) In contrast, the motor current j reaches a maximum for some finite value of the detachment rate θ.

also be extracted from simulation data. However, not all of the model parameters necessary for simulations can be directly measured in experiments. We will therefore employ the following strategy: First, we develop a theoretical analysis of our model, and extract model parameters from experimental data as far as possible. With analytical expressions for all relevant quantities at hand, we then fit our model to the experimental measurements. Eventually, we will show that, with the global fit parameters obtained in this way, the theoretical predictions and simulation data of our model are in excellent agreement with experimental measurements.

9.2. Development of a mean-field theory

The configuration of a lattice at any given instant in time is described by a set of occupation numbers $\{n_i\}$. A lattice site i (a tubulin heterodimer on the protofilament) is either empty ($n_i = 0$) or occupied by the front head ($n_i = f$) or back head ($n_i = b$) of a motor dimer. For a statistical description we need the one-site and two-site probabilities, defined as

$$p(i, \alpha) = \text{Prob}(n_i = \alpha) \,, \tag{III.1a}$$

$$p(i, \alpha; j, \beta) = \text{Prob}(n_i = \alpha \wedge n_j = \beta) \,. \tag{III.1b}$$

We denote the position of a motor by the position of its front head and define the time-averaged dimer density as

$$\rho_i = p(i, f) \,, \tag{III.2}$$

which is then bounded to $\rho \in [0, \frac{1}{2}]$.

The rate of change of these probabilities can be described in terms of a set of master equations (224). For instance, for the time evolution of the probability that site i is occupied by the

front head of a motor, one obtains

$$\partial_t p(i,f) = v\left[p(i{-}1,f;i,0) - p(i,f;i{+}1,0)\right] \tag{III.3}$$
$$+ \omega_A\, p(i,0;i{-}1,0) - \omega_D\, p(i,f) - \theta\, p(i,f;i{+}1,b)\ .$$

Here, the first term on the right-hand side represents a transport current given by the difference between a gain and a loss term. The gain term describes the probability per unit time that a motor (front head of a dimer) located at lattice site $i{-}1$ moves forward onto an empty site i, and the loss term describes the probability per unit time that a motor hops from site i to the next (empty) site, $i{+}1$. The remaining terms describe attachment and detachment processes with the joint probabilities selecting the allowed lattice configurations. Thus, attachment of a dimer to the lattice is possible only if two neighbouring empty sites are available ($n_i = 0$ and $n_{i-1} = 0$). While an interaction-induced detachment process requires that two dimers are immediate neighbours ($n_i = f$ and $n_{i+1} = b$), the rate of spontaneous detachment is proportional to the single-site probability $p(i,f)$.

In general, the master equation, Eq. (III.3), is not closed as it links single-site to two-site joint probabilities. However, progress can be made by employing a mean-field approximation that neglects all correlations between the positions of motor dimers other than the steric constraint that dimers are not allowed to overlap, i.e. the front and the back heads of different motors cannot occupy the same lattice site. Furthermore, for rigid dimers $n_i = b$ implies that site $i{+}1$ is occupied by the front head of the same motor, $n_{i+1} = f$.

In order to show how the two-site joint probabilities can be reduced to one-site probabilities we will consider as an example $p(i,f;i{+}1,b)$. This probability, like any joint probability, can be expressed in terms of a conditional probability: $p(i,f;i{+}1,b) = p(i{+}1,b|i,f)\, p(i,f)$. As we are neglecting correlations in the position of different dimers, the probability that site $i{+}1$ is occupied by the back head of a dimer is independent of whether site i is occupied by the front head of another dimer or empty: $p(i{+}1,b|i,f) = p(i{+}1,b|i,0)$. Hence, in a mean-field approximation we have $p(i{+}1,b|i,f) = p\left(i{+}1,b|(i,f)\vee(i,0)\right) = p\left(i{+}1,b|\neg(i,b)\right)$. Using Bayes' theorem, this can be rewritten in the form $p\left(\neg(i,b)|i{+}1,b\right) \times p(i{+}1,b)/p\left(\neg(i,b)\right)$. Here, the remaining conditional probability $p\left(\neg(i,b)|i{+}1,b\right)$ equals 1 because the states (i,b) and $(i{+}1,b)$ are mutually exclusive. Hence, we are left with the desired decomposition into single-site occupation probabilities:

$$p(i,f;i{+}1,b) = \frac{p(i{+}1,b)\, p(i,f)}{1 - p(i,b)} = \frac{p(i{+}1,b)\, p(i,f)}{p(\neg(i,b))}\ . \tag{III.4}$$

Compared to a naive decomposition into single-site occupation probabilities $p(i{+}1,b)p(i,f)$, this equation includes a factor $1{-}p(i,b)$ which corrects for dimers spanning sites i and $i{+}1$, i.e., which takes into account those correlations that are due to the dimeric nature of the motor molecules. In the following we refer to such a factor as the local correlation factor. Using $p(i,b) = p(i{+}1,f)$ one may rewrite this result solely in terms of the density ρ_i as

$$p(i,f;i{+}1,b) = \frac{\rho_{i+2}\, \rho_i}{1 - \rho_{i+1}}\ . \tag{III.5}$$

In the same way, cf. Ref. (218), we can also approximate the other joint probabilities of Eq. (III.3).

9. Theoretical analysis

The ensuing mean-field master equation reads

$$\partial_t \rho_i = v \left[\frac{(1-\rho_i-\rho_{i+1})\rho_{i-1}}{1-\rho_i} - \frac{(1-\rho_{i+1}-\rho_{i+2})\rho_i}{1-\rho_{i+1}} \right]$$
$$+ \omega_A \frac{(1-\rho_i-\rho_{i+1})(1-\rho_{i-1}-\rho_i)}{1-\rho_i} - \omega_D \rho_i - \theta \frac{\rho_{i+2}\,\rho_i}{1-\rho_{i+1}} \; . \tag{III.6}$$

In the stationary state, where $\partial_t \rho_i = 0$, this expression recursively determines the occupation density of site i in terms of the densities of the neighbouring sites $i\pm1$. In general, the dynamics of such a system is very rich and entails boundary-induced phase transitions (146, 156, 166, 167, 179, 218).

As discussed above, kinesin-1 has a run length which is short (30) compared to the typical length of MTs (202). We also expect that attachment of motors to the MT occurs at relatively high rates. Here, the focus of our interest lies in the behaviour in the bulk of MTs. Hence, we may assume that the motor density is constant, $\rho_i = \rho$, [5] and arrive at the mean-field equation

$$\partial_t \rho = \omega_A \frac{(1-2\rho)^2}{1-\rho} - \omega_D \rho - \theta \frac{\rho^2}{1-\rho} \; , \tag{III.7}$$

which yields the motor density ρ_s in the stationary state ($\partial_t \rho = 0$) as

$$\rho_s = \frac{2\omega_A}{4\omega_A + \omega_D + \sqrt{4\omega_A\omega_D + 4\theta\omega_A + \omega_D^2}} \; . \tag{III.8}$$

Note that we could also have arrived at Eq. (III.8) by assuming attachment-detachment balance

$$\omega_A\, p(i,0;i-1,0) = \omega_D\, p(i,f) + \theta\, p(i,f;i+1,b) \; . \tag{III.9}$$

As we are only interested in the behaviour at steady state, we will omit the index s in the following, i.e. $\rho := \rho_s$.

By employing the mean-field approximation we can also derive an expression for the motor current j. This quantity is defined as the number of motors that pass through a site on the MT per unit time, and is therefore given by $j_i = vp(i,f;i+1,0)$. By analogy with the derivations of the previous paragraph and Ref. (218), and in agreement with Refs. (146, 166, 167), the motor current simplifies to

$$j(\rho) \approx v \frac{\rho\,(1-2\rho)}{1-\rho} \; . \tag{III.10}$$

In this equation, we again identify the local correlation factor $1/(1-\rho)$. Its significance can be understood as follows: Compared to the current-density relation for monomeric particles, $j(\rho) = \rho(1-\rho)$, Eq. (III.10) is skewed, i.e. its maximum lies at a density exceeding half-occupation, $\rho = \frac{1}{2}(2-\sqrt{2}) \approx 0.29$. This agrees remarkably well with the intuitive value for the density $\frac{1}{3}$, where on average, every dimer is followed by a vacancy, and is therefore free to jump.

---

[5] We have verified this assumption *a posteriori* with the parameters found in Eqs. (III.15)–(III.18) by performing simulations (data not shown). Our results indicate that already at small motor concentrations around 5 nM, boundary effects are restricted to a layer of approximately 100 lattice sites at the MT ends, much below their typical length.

9.3. Derivation of quantities important for experiments

With the analytical expressions for the stationary motor density ρ on the MT [Eq. (III.8)] and their flux $j(\rho)$ [Eq. (III.10)], we now have a description of the most central physical quantities that characterise the collective motion of molecular motors on a MT. As Figs. III.2a and III.2b show, these analytically calculated quantities agree very well with data from stochastic simulations.

Unfortunately, with present-day experimental techniques, it is difficult to measure collective quantities like the density ρ and the current j. It is much easier to determine quantities derived from the observation of single labelled motors. These include the dwell time τ of motors on the MT, their velocity V, run length l, and the landing rate λ. In order to define the link between theory and experiment which we ultimately aim for, we must therefore also find expressions for these quantities.

We first turn to the calculation of the dwell time τ. A motor located at site i can detach either spontaneously at rate ω_D, or additionally at a rate θ when another motor is located right next to it at site $i+2$. The corresponding probability is given by $p(i+2, f | i, f)$, which reduces to $\rho/(1-\rho)$, following the same steps as before. Hence, the dwell time is given by the inverse of the total detachment rate, comprising spontaneous and interaction-induced detachment:

$$\tau \approx \left[\omega_D + \theta \frac{\rho}{1-\rho} \right]^{-1} . \tag{III.11}$$

Similarly, in order to obtain the velocity of a motor we need to consider the probability that a particle located at site i finds the next site empty, $p(i+1, 0 | i, f)$. This gives for the motor velocity, again using a mean-field approximation,

$$V = V_0 \, p(i+1, 0 | i, f) \approx V_0 \, \frac{1-2\rho}{1-\rho} . \tag{III.12}$$

With Eqs. (III.11) and (III.12), the run length of a motor is given by

$$l = \tau V \approx V_0 \, \frac{1-2\rho}{\omega_D(1-\rho) + \theta\rho} . \tag{III.13}$$

Finally, we need to compute the landing rate of kinesin on a MT. In experiments, this quantity is determined by labelling only a small fraction of kinesin, e.g., with GFP, while the vast majority of motors remains unlabelled (30). The concentration of labelled motors is kept constant at a reference concentration c_0, and the unlabelled motors act as crowding agents which are added at varying concentrations. The landing rate is then obtained by counting how many labelled motors land on the MT per unit length and time. In our model, a motor can attach to a site i on the MT only if it finds both site i and the adjacent lattice site $i-1$ empty, $n_i = n_{i+1} = 0$. With λ_0 being the landing rate of the normalised amount (c_0) of labelled kinesin on an otherwise empty MT, the landing rate is $\lambda = \lambda_0 \, p(i, 0; i-1, 0)$, which at the mean-field level is approximated by

$$\lambda \approx \lambda_0 \, \frac{(1 - 2\rho)^2}{1 - \rho} . \tag{III.14}$$

It is important to note that the normalised landing rate λ_0 may differ from $\omega_A(c_0)$. This is because the size of a label such as GFP is comparable to that of the motor. Hence, the attachment rates of labelled and unlabelled motors to the MT may be different.
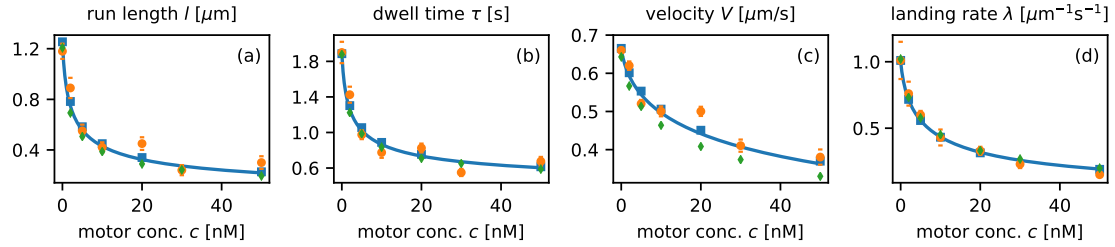
Figure III.3.: Comparison with experimental data. Orange circles show the measurements for (a) the run length, (b) dwell time, (c) velocity, and (d) landing rate of kinesin motors, as measured by Telley et al. (30). In blue, we show the fit of our model to this data. Lines are results of our mean field theory, squares compare these calculations with simulations based on Gillespie's algorithm. Green diamonds show data for a model where motors can temporarily switch to an inactive state, see the main text.
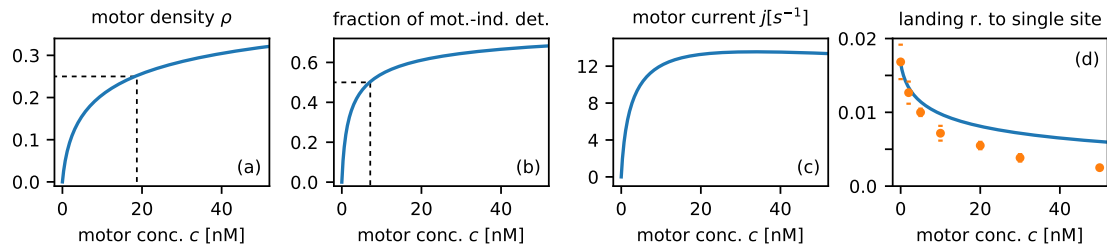
Figure III.4.: Characterisation of crowding effects. The plot depicts important physical quantities available from our model, for the same parameters as in Fig. III.3. (a) The density of motors on the MT. Because kinesin-1 is a dimer, $\rho = \frac{1}{2}$ implies that the lattice is fully decorated with motors. (b) Fraction of detachment events which are due specifically to motor-induced detachment. Even at low concentrations around 7 nM, facilitated dissociation is as prominent as spontaneous detachment. (c) The motor current on the MT, i.e., the number of motors passing over a lattice site per unit time. (d) The landing rate of motors on the MT (orange: experimental data (30), blue: mean-field results), assuming that a single lattice site were sufficient for the landing of a motor. The agreement is worse than for the original model [Fig. III.3d].

9.4. Comparison of model results with experimental data

The primary goal of this work is to compare the predictions of our theoretical model with experimental data. Telley et al. (30) have provided an extensive set of measurements for the motor kinesin-1, which is shown in Fig. III.3. Here, the volume concentration of the motor is varied, and this process is incorporated into our model by setting $\omega_A = \omega_a c$. From their data, we can directly extract several of our model parameters. The hopping rate v is obtained from the velocity V_0 of a

motor in the limit of low motor density (Fig. III.3c),

$$v = 0.66\,\mu\text{m s}^{-1}a^{-1} = 79\,\text{s}^{-1}\ . \tag{III.15}$$

The detachment rate ω_D follows from the dwell time at small motor concentration (Fig. III.3b),

$$\omega_D = \frac{1}{1.9\,\text{s}} = 0.53\,\text{s}^{-1}\ , \tag{III.16}$$

and similarly the landing rate of a normalised amount of labelled kinesin can be directly read off from Fig. III.3d at $c \approx 0$,

$$\lambda_0 = 1.8 \cdot 10^{-2}\mu\text{m}^{-1}\text{s}^{-1}\ . \tag{III.17}$$

This leaves two parameters to be specified, the attachment rate of unlabelled motors to the MT per concentration, ω_a, and the rate θ specifying interaction-induced detachment. As there are four independent sets of quantities that have been measured (30) (run length, dwell time, velocity, and landing rate), comparison of all four with our theoretical results constitutes a stringent test of the validity of the assumptions on which the model is based. We have performed a global fit for the four independent quantities l, τ, V, and λ by minimising the squared sum of deviations between experimental measurements and mean-field results, weighted by the experimental confidence interval, see Methods. This gives the following values for the rates

$$\omega_a = 5.4 \cdot 10^{-2}\,\text{nM}^{-1}\text{s}^{-1}\ , \tag{III.18a}$$
$$\theta = 2.4\,\text{s}^{-1}\ . \tag{III.18b}$$

 As can be seen in Fig. III.3, using these global fit parameters we find excellent agreement between our theory and all experimentally measured quantities.

Both these fit parameters are interesting in themselves. The attachment rate ω_a specifies how quickly kinesin attaches to empty lattice sites. In this context, one must keep in mind the fact that the physical quantity underlying the fit is the total motor density ρ on the MT, while the data from Telley et al. (30) are derived from observations of the small minority of labelled motors. In our model, the rate ω_a specifies the attachment rate of the unlabelled motors, which act as a crowding agent but are otherwise invisible experimentally (30). How then does ω_a compare to the landing rate λ_0 for labelled motors? This rate was measured at a motor concentration of 5 pM and, assuming that motors in the TIRF setup can walk on roughly half of the 13 protofilaments (109), this can be converted into a per-site attachment rate of approximately $5 \cdot 10^{-3}\,\text{nM}^{-1}\text{s}^{-1}$. This value is 10 times smaller than the attachment rate for unlabelled motors, and it demonstrates that, while labelling with GFP conserves many kinetic parameters of native kinesin (105, 225, 226), the attachment rate of the labelled protein is significantly lower.

Secondly, let us look more closely at the rate θ, which quantifies motor-induced detachment from the filament. The value of θ exceeds that of the spontaneous detachment rate ω_D by four-fold. This is remarkable, because it implies that, under crowded conditions, motor-induced detachment is the dominant mechanism by which motors leave the MT. We will analyse this and other implications of these parameters in greater detail in the following section.

One strength of our approach to the quantitative description of the collective dynamics of

molecular motors with a theoretical model is that it allows us to infer physical quantities which are experimentally difficult to access. In particular, it is interesting and instructive to study the behaviour of the motor density along the MT, ρ, which is the fundamental quantity characterising the degree of crowding on the MT. In Figure III.4a, ρ is plotted as a function of the volume concentration of motors c. At small concentrations, the density rises steeply with c, and becomes half-maximal around 20 nM. At this concentration, on average every second binding site on the MT is occupied by a motor head. As c is increased further, the motor density rises only modestly. This is because attachment of additional motors becomes increasingly unlikely when many motors are already present on the MT, and motor-induced detachment becomes more prominent.

Figure III.4b shows the fraction of motor detachments induced by the presence of another motor, plotted as a function of c. With Eq. (III.7), we find that the contributions of spontaneous and motor-induced detachment are already comparable at a motor concentration around 7 nM, significantly below the concentration required for half-occupation [Fig. III.4a]. The reason for this is that the rate θ exceeds ω_D by several-fold, such that motor-induced detachment plays the central role even on filaments with relatively little crowding. The steep increase in the contribution of motor-induced detachment to all dissociation events at low motor concentrations also explains the rapid decrease of quantities such as the motors' run length l [Fig. III.3a] and dwell time τ [Fig. III.3b] at these concentrations.

The motor current j may also be examined directly with our model and the parameters extracted from experimental measurements (Fig. III.4c). Once more, we find a steep increase at low concentrations. The current becomes maximal at around $c \sim 20$ nM, i.e. the concentration where the density is half-maximal, and for higher concentrations the motor current remains almost constant.

Finally, the good agreement of our model with experimental data allows us to study the impact of model variations. For example, it has been suggested (120) that kinesin-1 first binds via a single head to the MT on landing, and subsequently attaches its other head. We have directly tested how a different attachment mechanism might affect the landing rate by assuming that a single binding site is sufficient for the motor to attach to the MT. As a result, the attachment term in Eq. (III.7) reduces to $\omega_A(1 - \rho)$. Fig. III.4d compares the landing rate obtained in this way with experimental data. Clearly, neither with the fit parameters for the original model, nor with parameters fitted to the modified model do we obtain satisfactory agreement between theoretical results and experimental data. Therefore, our data suggest that kinesin can land on the MT only where two adjacent binding sites are empty.

9.5. The origin of periods of no or slow motion of motors

As shown in the previous sections, our mathematical model explains the kinetic data for the run length, dwell time, velocity, and landing rate of kinesin-1 motors on MTs with high accuracy. These quantities are averaged over a large number of motors and characterise their collective transport along MTs very well. However, with our model, as well as in experiments, quantities other than averages are also accessible, such as the statistics of individual steps of motors. Such quantities are instructive, as they afford insight into the stochastic motion of kinesin at a deeper level. A particularly interesting finding made by Telley et al. (30) in this respect was that kinesin-1

motors, which normally move at a speeds as high as 79 steps/s along the MT under uncrowded conditions, sometimes show periods in which they rest on the MT or their motion is at least considerably slowed down. These periods lasted for several tenths of a second, during which a motor would typically proceed by dozens of steps. It was found that the frequency of these periods increased with the volume concentration of kinesin, and hence with the degree of crowding on the MT (30).

However, the authors of that study were only able to image the motors every 0.1 s, such that the localisation accuracy of kinesin-1 was of the same order of magnitude as the typical distance traversed between two measurements. Furthermore, because kinesin's stepping mechanism includes chemical reactions as well as diffusive motion, this motor is a stochastic stepper. Consequently, Telley et al. (30) were faced with the problem of robustly distinguishing periods of no (or very slow) motion,[6] in which motors are assumed to hardly move at all, from stochastically slow motion which simply reflects the stochasticity of kinesin's steps but is otherwise normal.

To overcome these problems, Telley et al. (30) developed a detection scheme for the periods of no or slow motion as follows: The location of the motors was measured every 0.1 s. If a motor failed to advance a critical distance d_c between two time frames, or its motion was directed off-axis or backwards (exceeding a critical angle α_c), this displacement was considered as a *candidate* for the onset of a period of no or slow motion. However, in order to mark the start of such a period, three successive small displacements were required. To account for the effect of experimental noise, single advances exceeding d_c were allowed during a period of no or slow motion, so that the period was only considered as terminated when the displacement was greater than d_c twice in a row.

The key parameters which determine the sensitivity of the detection of periods of no or slow motion are α_c and (in particular) d_c. On the one hand, these quantities should be chosen to be so large that fluctuations due to experimental noise are unlikely to prematurely terminate such periods. On the other hand, the critical distance must be kept so small that these periods can be robustly distinguished from normal motion which is slow because of the stochasticity of kinesin's steps. With the parameters $d_c = 40$ nm and $\alpha_c = 60°$, Telley et al. (30) found that approximately every second kinesin motor showed a period of no or slow motion at some point while it progressed along the MT. During the periods of no or slow motion, motors proceeded on average 10 lattice sites. This value seems large, but it is much less than the expected ~ 30 lattice sites which a motor would traverse under uncrowded condition during the minimal time necessary for detection of these periods (0.3s).

In order to compare the predictions of our model with the experimental data of Telley et al. (30), we adapted and applied their experimental detection scheme for periods of no or slow motion to our system. Note, however, that the motion of motors is restricted to a single dimension in our model, while occasional side-steps, as well as off-axis fluctuations are possible in experiments. Consequently, the two parameters, d_c and α_c, used for the experimental detection have to be reduced to a single parameter d_c for our purposes. Moreover, since a finite progression d_c between

---

[6]Note that Telley et al. (30) use the term "pause" for periods in which no or little motion was detected, and they further distinguish between "wait" and "stop" for such events in which kinesin continued its run subsequent to the pause, or detached from the MT. In this work, we distinguish between the *phenomenon* observed in experiments, which we will call "periods of no or slow motion", and the *cause* of these periods, which we term "pause" in the following.

two frames was allowed primarily in order to account for experimental inaccuracies which are absent in simulations, d_c has to be critically evaluated, and the role of noise must be simulated. To this end, we first chose the same threshold distance d_c = 40 nm as in Ref. (30), corresponding to 5 lattice sites. With this value, we found that the progression of a motor between the beginning and the end of a so defined period of no or slow motion was almost 30 lattice sites [Fig. III.5a]. This is significantly larger than the experimentally measured length of 10 lattice sites, and therefore indicates that most of the detected events in fact do not show behaviour which is physically different from normal motion. Thus, most of the periods of no or slow motion detected with this choice of d_c result from the stochastic motion of kinesin. Even for a threshold distance of 3 lattice sites, the progression exceeded experimental data, so that we had to reduce the value of d_c to 2 lattice sites in order to find agreement with experimental results [Fig. III.5a]. However, the agreement found with this parameter choice deteriorated when Gaussian noise was added to the simulation data (in order to account for experimental fluctuations) before applying the protocol [σ = 20 nm in Fig. III.5a].

Moreover, the statistics of the durations of periods of no or slow motion detected from our simulation data differed from experimental results. While Telley and coworkers (30) report an exponential distribution, our results indicate a non-exponential distribution with peaks around 0.4–0.5 s, see Fig. III.5b. Also the addition of Gaussian noise, or variation of the detection threshold d_c did not qualitatively change this distribution.

We therefore conclude that the detection protocol of Telley et al. (30) is inappropriate for the analysis of the data obtained from stochastic simulations of our original model for two reasons. Firstly, it fails to distinguish reliably between periods of no or slow motion and stochastically slow, but normal motion of kinesin, as the progression of motors between the beginning and end of the detected periods clearly exceeds experimental results. Secondly, the distribution of the durations of periods of no or slow motion in simulations differs fundamentally from the experimental findings of Telley et al. (30). Consequently, in order to understand the full dynamic behaviour of motors on the MT additional stochastic processes must be taken into account, which are not captured by our original model. This will be the focus of the next section.

In order to examine model variations which could possibly explain the experimental findings of Telley et al. (30) on periods in which the motors did not or only very slowly move, we looked at the data they obtained at low motor concentrations. Interestingly, even though motors proceed along the MT (almost) in the absence of other motors at these concentrations, periods of no or slow motion were observed occasionally. This prompted us to study a variant of our model in which motors can stochastically pause on the MT, i.e., they may temporarily switch to an inactive state in which they cannot move. From the experimental data at low concentrations, we read off a per-step chance of lapsing into inactivity of $p_{\text{inactivation}}$ = 0.4%, and a pausing time with average duration T = 0.12 s, after which motors are reactivated again. We therefore introduced rates $r_{\text{inactivation}}$ = $0.004v$ = $0.32\,\text{s}^{-1}$ and $r_{\text{activation}}$ = $1/0.12\,\text{s}^{-1}$ = $8.3\,\text{s}^{-1}$ at which motors switch to an inactive or active state, respectively. At the molecular level, a motor might become inactive, for instance, when a motor is trapped in an unfavourable chemical state due to imperfect synchronisation of its heads (120); however, the particular molecular mechanism involved is not important for the argument below.

Spontaneous pausing of driven particles has in the past been studied in the context of RNA

transcription (227–229) as well as the motion of myosin motors (230, 231). However, these studies focused mostly on collective properties of the systems, as opposed to the statistics of individual steps of kinesin-1 (30) which we aim to describe here. On this level, if motors are allowed to switch into an inactive mode, we expect crowding to enhance the measured probability of undergoing a period of no or slow motion, because other motors will tend to form a traffic jam behind inactive motors. Although the motors caught up in the traffic jam are not intrinsically inactive, they are unable to progress until the inactive motor has become active again. Therefore, crowding should amplify the impact of stochastic pausing and consequently lead to frequent periods in which kinesin motors show no or only slow motion along the MT.

We tested these expectations directly by performing Monte Carlo simulations of this variant model. Since the two additional stochastic processes, namely spontaneous inactivation and activation of motors, are rare events, we found that they have only a small impact on motor run lengths, dwell time, velocity and landing rate (green diamonds in Fig. III.3). In contrast, motor behaviour changed considerably at the level of individual steps: Unlike the case in our original model, Fig. III.1, the durations of periods of no or slow motion were (approximately) exponentially distributed in the variant model, in accordance with experimental findings (30)[7]. Following Telley et al. (30), it is essential to extrapolate this exponential distribution below the cutoff time 0.3 s in order to obtain the corrected frequency and mean duration of the periods of no or slow motion. The reason for this is that the cutoff 0.3 s is a technical choice, but there is no physical reason why motors would not also experience periods of no or slow motion which are shorter than that. As a result, periods of no or slow motion comprise the detected periods (those lasting 0.3 s and longer), as well as the undetected periods (those of shorter duration). The mean duration of the periods of no or slow motion is therefore given by the parameter of the exponential decay of the distribution. Figure III.5c shows the concentration dependence of the mean duration of periods of no or slow motion, as they were extracted from simulation data in this way, and they reproduce the experimental findings (30) well. Moreover, these values were almost independent of the parameter d_c used for the detection algorithm, which ensures that periods of no or slow motion of our model variant are now detected robustly and accurately.

We are now in a position to compare simulation data for the frequencies of periods of no or slow motion with those of the experiments of Telley et al. (30), as shown in Fig. III.5d. While the uncorrected probabilities (asterisks) remain below experimental values, as expected, the frequencies corrected for the cutoff (squares) are comparable to those found experimentally (30) for low concentrations. However, as the concentration is increased, we found that the frequencies measured in our simulations exceed experimental values. This points to the need for further modifications of our model.

In principle, any additional interactions can be included into our model and data obtained

---

[7] As reactivation from an inactive state is a one-step process, the distribution of the duration of periods of no or slow motion should be *exactly* exponentially distributed in the absence of crowding and noise; this agrees with simulation data analysed with the detection algorithm of Telley et al. (30). As the degree of crowding increased due to additional motors on the MT, and as noise was added to the simulation data, the distribution gradually changed and was non-exponential for high crowding and noise level, albeit with an exponential tail for durations > 0.5 s. In order to comply with the procedure of Telley et al. (30), we used the distribution's tail to fit an exponential function to the simulation data, as we extrapolated the distribution below the cutoff value 0.3 s in order to obtain, e.g., the mean duration.

from stochastic simulations. However, a more instructive approach for our purposes is, however, to analyse the physical principles leading to periods of no or slow motion, and explore how exactly the inactivation of a single motor results in the formation of traffic jams which amplify the effect of pausing. To study this, we employed a different algorithm to detect periods of no or slow motion: Here, we only counted motors that were (i) inactive themselves, or (ii) trapped in a traffic jam behind an inactive motor. In contrast, events in which motors moved slowly because they were caught up in a stochastically assembled traffic jam (in which no motor is inactive) were not taken into account. The frequencies of periods of no or slow motion obtained with this alternative algorithm (triangles in Fig. III.5d) agree well with those calculated with the original algorithm (squares in the same Figure). This implies that although stochastically arising traffic jams (in which no motor is inactive) slow down the collective motion of motors (132, 156), they do not increase the incidence of periods of no or slow motion. In contrast, these periods are predominantly due to the spontaneous (and transient) inactivation of motors and the associated formation of traffic jams behind these motors.

Given that the dominant cause of periods of no or slow motion is the formation of traffic jams behind inactive motors, further insight can be gained by estimating theoretically the length of these traffic jams. Imagine that a motor pauses at some lattice site. Then, the n-th motor behind this inactive motor is on average n/ρ sites away from it. Since each motor requires two binding sites on the MT, the n-th motor therefore typically has to travel $n/\rho - 2n$ sites to reach the end of the traffic jam. Hence, the time needed for the n-th motor to reach the end of the traffic jam may be estimated as $t(n) = (n/\rho - 2n)/V$. As a consequence, during the time T required for reactivation of an inactive motor, a traffic jam containing $N_1 = n(T) = TV/(\rho^{-1} - 2)$ motors will form. After the inactive motor has resumed its run, all the motors stuck in the traffic jam can start moving again one after another, so that it will typically take a time $N_1 v^{-1}$ before the original traffic jam has completely dissolved. During this time, another $N_2 = n(N_1 v^{-1})$ motors will have reached the end of the traffic jam, and more time will be needed until this additional traffic jam is dispersed, and so on. Taking the sum over the number of motors caught in traffic jams found in this way, the number of motors $N = N_1 + N_2 + \ldots$ which are ultimately affected by a single spontaneously pausing motor is consequently obtained from a geometric series, yielding

$$N = \frac{Tv}{\rho^{-1} - 2 - Vv^{-1}} \, . \tag{III.19}$$

This equation suggests that the effect of spontaneous pausing is considerably amplified by crowding. While the *cause* of traffic jams is the inactivation of a single motor, the *phenomenon* detected with the scheme of Telley et al. (30) is also visible for N other motors that are effectively caught in a traffic jam; consequently, $p_{\text{per. no/slow mot.}} = p_{\text{inactivation}}(1+N)$. Figure III.5d shows the probability per step obtained in this way. Given the level of the heuristic arguments, the agreement with simulation data is satisfactory.

Having a theoretical estimate for the density dependence, and with Eq. (III.8) also the concentration dependence, of the frequencies of periods of no or slow motion at hand, further model variations can now be tested in a relatively simple way. For example, it seems plausible that motors align in a traffic jam very compactly, such that each motor requires a single lattice site on the MT only. This would be in accordance with studies in which the decoration of MT sheets with

immobilised dimeric kinesin was investigated, and it was found that kinesin binds to the MT via a single head only under certain conditions (31, 232). For this model, the n-th motor behind an inactive motor would then have to travel further compared to the original (i.e., spaced) jamming model, namely $n/\rho - n$ sites. In consequence, the term $\rho^{-1} - 2$ in Eq. (III.19) would be modified to $\rho^{-1} - 1$, and the amplification of spontaneous pausing changes accordingly. As shown in dashed lines in Fig. III.5d, the resulting per step probability of entering a period of no or slow motion reproduces the experimental concentration dependence (30) better than the original model in which motors align spaciously in a traffic jam.

In conclusion, we have shown that spontaneous and transient inactivation of motors is the key to an understanding of the occurrence of periods of no or slow motion. The frequency of these periods is determined by the formation of traffic jams, in which motors (which are not intrinsically inactive themselves) cannot, or only slowly progress. However, we are at present unable to uniquely determine the precise mechanisms of jamming, and predict quantitatively how exactly they amplify the frequencies of periods of no or slow motion of molecular motors. A central problem seems to be that periods of no or slow motion are relatively short-lived compared to the threshold time required to detect such an event. This implies that large numbers of these events remain undetected, and can only be resolved by extrapolating the duration distribution, as explained above. As a consequence, we expect that the estimates of the frequencies of periods in which kinesin motors move only very slowly or come to a complete halt on the MT are subject to relatively large errors. It will in the future therefore be important to further investigate the origin of these periods; in particular, algorithms have to be developed which allow a more direct detection of short pauses, e.g., by increasing the frame rate of experiments. Furthermore, direct visualisation of the inactive state would be highly informative. In summary, crowding is most probably not the underlying reason for periods of no or slow motion of motors, but acts as an amplifier to increase their frequency, although their ultimate cause is related to inactive states of kinesin motors.

9.6. Insight into the stepping cycle of kinesin

Our findings concerning the motor-induced detachment of kinesin motors provide insight into their stepping cycle. We would like to emphasise first that none of the results presented in the previous sections depends on whether disengagement of the front or rear motor from the MT is enhanced by the presence of another motor. Consequently, "bouncing off" (the rear motor detaches) and "kicking off" (the front motor detaches) interactions lead to identical results (data not shown). In fact, there are experimental indications that it is the trailing motor which bounces off when it encounters another motor on the MT. This was suggested by, among others, Telley et al. (30), who used non-motile rigour mutants, in addition to wild-type kinesin-1. Here, the tightly bound mutant motors act as obstacles on the MT, and the wild-type motors detach at an enhanced rate on encountering such an obstacle. This would also suggest that when two wild-type kinesin motors come into contact on the MT, it is the trailing motor that is more likely to detach.

At the molecular level, these indications enables us to associate the motor-induced unbinding process with a specific state in the mechanochemical cycle of kinesin. This cycle comprises transitions between several states in which one or both kinesin heads are bound to the MT, and the

two heads contain different bound nucleotides. During the stepping cycle, kinesin passes through a state in which only a single head is bound to the MT. This weakly bound state is reached after the back (i.e., the tethered) head is released from the MT, and the head that remains bound to the MT binds and hydrolyses ATP. It is likely that this one-head-bound (1HB) state, in which the head attached to the MT is associated either with ADP or ADP·P_i, is the state from which motors usually detach into the cytosol at finishing their run (97, 119). If the lifetime of this state is increased, kinesin should therefore also unbind at an enhanced probability.

We hypothesise that the increase in the detachment rate seen when two motors occupy directly adjacent binding sites on the MT is directly related to this weakly bound state. Our idea is related to that of Klumpp et al. (233) who found that molecular motors with a two-step mechanochemical cycle show crowding-dependent unbinding when detachment happens at different rates from both states. More specifically, we suspect when the rear motor's tethered head attempts to step to the next binding site, but finds this site occupied by another motor, the rear motor can leave its 1HB state only by stepping back (which is rare (121)), or by waiting until the next site is vacated. In this case, the back motor is "trapped" in a weakly bound state, and the detachment rate is enhanced accordingly. We, therefore, interpret θ as the dissociation rate of kinesin from the 1HB ADP(·P_i) state. This interpretation is also supported by measurements of the dissociation rate of single-headed kinesin motors which are artificially held in the ADP and ADP·P_i state, where rates of $3.7\,s^{-1}$ and $3.8\,s^{-1}$, were found, respectively (97); these measurements are remarkably similar to the value of θ obtained from Eq. (III.18b). Following these arguments, the time fraction f which a motor spends in the 1HB state during a normal step, may be determined from $\omega_D = f\theta$. By direct comparison, we obtain $f = 0.22$, which implies that kinesin-1 remains in the 1HB ADP(·P_i) state for approximately 22% of the time needed to complete a stepping cycle.

In summary, our findings suggest that the kinesin-1 step cycle comprises (at least) two transitions which are of similar duration, as opposed to a single rate-limiting step. This is in agreement with a recent interpretation of the kinesin step cycle (113). We believe that our study will also help to reconcile conflicting results on the number and type of rate-limiting steps obtained from optical trapping experiments (100, 121), dark-field (122) and interferometric scattering (120) microscopy experiments, as well as from measurements of the statistics of single motor runs (124). While the methods employed in most of these experiments give rise to much shorter length and time scales, labelling of the heads of motors, or applying force to them using an optical trap risks interfering with the step cycle. The advantage of our analysis is that interference effects are minimised. Therefore, crowding experiments (30) provide unique insight into a microscopic process in a minimally invasive way.
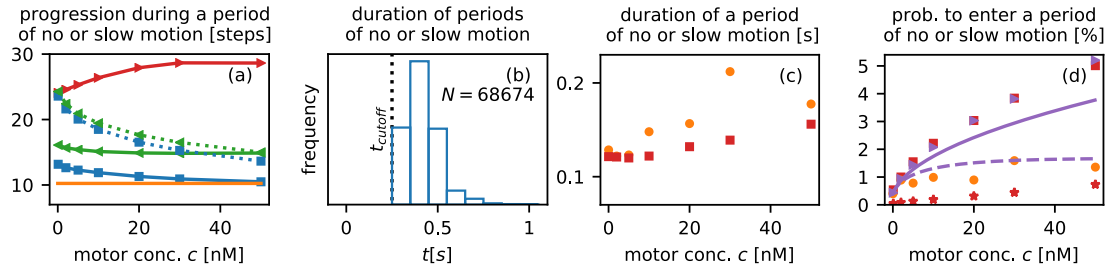
Figure III.5.: Periods in which kinesin-1 motors show no or only very slow motion. The model parameters are the same as in Fig. III.3. Experimental measurements from Telley et al. (30) are shown in orange. For the detection of these periods, the protocol of Telley et al. (30) was used (see the main text). (a)–(b) Our model cannot explain the frequent periods of no or slow motion of motors observed experimentally. (a) Distance travelled by a motor between the beginning and end of such a period. A threshold value of d_c = 5 sites (red line) is too large for reliable detection of these periods: Motors traverse for almost 30 lattice sites between the beginning and end of such a period, which is three times the experimental result (orange line). This implies that most of the detected events actually reflect stochastically slow motion which is otherwise normal, and hence the scheme detects these events inaccurately with this choice of d_c. Reduction of the threshold to d_c = 3 sites (green), or d_c = 2 sites (blue) leads to results that are in closer agreement with experimental data. However, this correspondence deteriorates on addition of Gaussian noise (σ = 20nm) to the simulation data before applying the detection protocol (dashed lines) (b) Duration of the so detected periods of no or slow motion for c = 20 nM and a detection threshold d_c = 2 sites. In contrast to the experimental findings, where an exponential distribution was observed, the duration peaks around 0.4 s. This result does not change qualitatively when d_c is varied, or Gaussian noise is added at various strengths. (c)–(d) Qualitative agreement with experiments is found when motors can spontaneously switch between an active and inactive mode at rates extracted from experimental data (30). (c) The duration of periods of no or slow motion detected from simulations of this model variant (red squares) is similar to those measured in experiments (30). The duration was computed by extrapolating the (now) approximately exponential distribution of the detected periods below the cutoff time 0.3 s (30) and the main text for details. (d) The per-step probability that a motor is found in a period of no or slow motion. The direct yield from the detection algorithm (red asterisks) is below experimentally observed (30) values. When their frequency is corrected for the time cutoff (red squares), similar to the procedure used in experiments (30), good qualitative agreement is found, in particular at low motor concentrations. Violet triangles show the frequencies obtained with a different algorithm which counts motors that are inactive, or caught up in a traffic jam behind an inactive motor, but not motors which move slowly due to their stochastic motion. The good agreement between these results and the original detection protocol (red squares) reveals that spontaneously inactivated motors are the dominant contribution for periods of no or slow motion. Solid and dashed lines show heuristic estimates of the probability of entering such a period, assuming that motors in a traffic jam require two, or only one binding site on the lattice. For details, see the main text.

10. Conclusion

In this work, we have theoretically studied the impact of interactions between kinesin-1 motors on their motility and transport properties along microtubules. Based on experimental observations, we have generalised a lattice gas model (155, 156) that has previously proven successful in explaining collective phenomena, such as the existence of traffic jams, which have recently been observed experimentally for kinesin-8 (132), and kinesin-4 (133). The generalised model includes the additional process of motor-induced detachment from the microtubule when one motor is directly adjacent to another, as well as the stochastic inactivation (pausing) of motors. With only two fit parameters, namely the rate of motor-induced detachment θ, and the attachment rate of motors to empty lattice sites ω_A, our model can account for four independent sets of measurements from *in vitro* experiments (30) with kinesin-1 (Fig. III.3).

The level of agreement of our model with experimental data allows us to explore the origin of the relatively long periods during which motors hardly move along the MT at all, which have been observed in experiments (30). We find that crowding alone cannot explain the high frequency of these periods (Fig. III.5). We therefore hypothesize that motors may stochastically switch into an inactive mode. Consequently, crowding leads to the formation of traffic jams behind inactive motors; these traffic jams significantly amplify the number of motors which pause on the filament, Eq. (III.19). Our findings suggest that motors might actually be aligned very densely in a traffic jam (Fig. III.5) such that every motor occupies only a single tubulin dimer, in accordance with Ref. (31). By comparing the rates of motor-induced detachment and spontaneous unbinding, we find that kinesin-1 motors spend approximately 22% of their stepping cycle in a weakly bound state. Most probably, motor-induced detachment occurs when the rear motor is held in this state for a prolonged time when two motors are directly adjacent, and that its unbinding is therefore increasingly likely.

Our approach to quantitatively model the dynamics of molecular motors enables us to investigate collective properties of kinesin-1 motors in a "real life" situation. Firstly, in the experiments of Telley and coworkers (30), on which our model is based, only a small fraction of motors was labelled. Secondly, insight into the interactions of motors with each other has been gained in our study without perturbing motor behaviour by applying forces etc. Our results enable us, for example, to compare the landing rates of labelled and unlabelled motors, and we have found that in fact labelled motors attach to the MT more slowly than unlabelled motors. This illustrates that the choice of a large label can have a crucial impact on certain quantities, and thus great care should be taken in interpreting experimental data. Most importantly, our model and the experiments of Telley et al. (30) provide unique insight into the stepping cycle of kinesin, which allows us to estimate the lifetime of a specific, weakly bound state. The major drawback of our method is at once its greatest strength: Our approach is very indirect. The application of forces to kinesin motors, e.g. by using optical traps (100, 119), as well as the attachment of large labels such as gold particles to kinesin heads (120, 122) might have crucial influence on motor dynamics (123). Therefore,

indirect methods (124, 125) such as the approach employed in this work are essential to confirm, and improve experimental results found by direct observation.

Future studies, both theoretical and experimental, will have to examine more closely the formation and dissolution of traffic jams induced by the spontaneous inactivity of a motor, for example. In the same way, the spatial arrangement and conformation of motors in a traffic jam requires closer attention. Such studies are essential to further improve our understanding of the role of interaction between molecular motors for the dynamics along cytoskeletal filaments. This might have important implications for the biological function of such processes in the crowded environments within cells.

Bibliography

[1] M. Rank, L. Reese, and E. Frey, Physical Review E **87**, 032706 (2013).

[2] M. Rank, A. Mitra, L. Reese, S. Diez, and E. Frey, Physical Review Letters **120**, 148101 (2018).

[3] M. Rank and E. Frey, arXiv:1805.03432 (2018).

[4] J. Howard, *Mechanics of Motor Proteins and the Cytoskeleton* (Sinauer Associates, 2001).

[5] J. Howard and A. A. Hyman, Nature **422**, 753 (2003).

[6] E. Karsenti and I. Vernos, Science **294**, 543 (2001).

[7] B. Alberts, A. Johnson, J. Lewis, M. Raff, K. Roberts, and P. Walter, *Molecular Biology of the Cell*, 5th ed. (Garland Science, 2008).

[8] T. Antal and P. Krapivsky, Physical Review E **76**, 21121 (2007).

[9] T. Antal, P. L. Krapivsky, and K. Mallick, Journal of Statistical Mechanics: Theory and Experiment **2007**, P08027 (2007).

[10] F. Jülicher and J. Prost, Physical Review Letters **75**, 2618 (1995).

[11] S. Kassem, T. van Leeuwen, A. S. Lubbe, M. R. Wilson, B. L. Feringa, and D. A. Leigh, Chem. Soc. Rev. **46**, 2592 (2017).

[12] R. Pei, S. K. Taylor, D. Stefanovic, S. Rudchenko, T. E. Mitchell, and M. N. Stojanovic, Journal of the American Chemical Society **128**, 12693 (2006).

[13] K. Lund, A. J. Manzo, N. Dabby, N. Michelotti, A. Johnson-Buck, J. Nangreave, S. Taylor, R. Pei, M. N. Stojanovic, N. G. Walter, E. Winfree, and H. Yan, Nature **465**, 206 (2010).

[14] S. Klumpp and R. Lipowsky, Proceedings of the National Academy of Sciences **102**, 17284 (2005).

[15] A. R. Rogers, J. W. Driver, P. E. Constantinou, D. Kenneth Jamison, and M. R. Diehl, Physical Chemistry Chemical Physics **11**, 4882 (2009).

[16] D. K. Jamison, J. W. Driver, A. R. Rogers, P. E. Constantinou, and M. R. Diehl, Biophysical Journal **99**, 2967 (2010).

[17] J. W. Driver, A. R. Rogers, D. K. Jamison, R. K. Das, A. B. Kolomeisky, and M. R. Diehl, Physical chemistry chemical physics : PCCP **12**, 10398 (2010).

Bibliography

[18] F. Berger, C. Keller, S. Klumpp, and R. Lipowsky, Physical Review Letters **108**, 208101 (2012).

[19] J. Brugués, V. Nuzzo, E. Mazur, and D. J. Needleman, Cell **149**, 554 (2012).

[20] V. Varga, J. Helenius, K. Tanaka, A. A. Hyman, T. U. Tanaka, and J. Howard, Nature Cell Biology **8**, 957 (2006).

[21] V. Varga, C. Leduc, V. Bormuth, S. Diez, and J. Howard, Cell **138**, 1174 (2009).

[22] L. Reese, A. Melbinger, and E. Frey, Biophysical Journal **101**, 2190 (2011).

[23] A. Melbinger, L. Reese, and E. Frey, Physical Review Letters **108**, 258104 (2012).

[24] J. Hazel, K. Krutkramelis, P. Mooney, M. Tomschik, K. Gerow, J. Oakey, and J. C. Gatlin, Science **342**, 853 (2013).

[25] M. C. Good, M. D. Vahey, A. Skandarajah, D. A. Fletcher, and R. Heald, Science **342**, 856 (2013).

[26] J. Halatek and E. Frey, Cell Reports **1**, 741 (2012).

[27] M. Winey, C. L. Mamay, E. T. O'Toole, D. N. Mastronarde, T. H. Giddings, K. L. McDonald, and J. R. McIntosh, The Journal of Cell Biology **129**, 1601 (1995).

[28] T. Mitchison and M. Kirschner, Nature **312**, 237 (1984).

[29] N. Hirokawa, Science **279**, 519 (1998).

[30] I. A. Telley, P. Bieling, and T. Surrey, Biophysical Journal **96**, 3341 (2009).

[31] A. Vilfan, E. Frey, F. Schwabl, M. Thormählen, Y.-H. Song, and E. Mandelkow, Journal of Molecular Biology **312**, 1011 (2001).

[32] B. J. Reddy, S. Tripathy, M. Vershinin, M. E. Tanenbaum, J. Xu, M. Mattson-Hoss, K. Arabi, D. Chapman, T. Doolin, C. Hyeon, and S. P. Gross, Traffic **18**, 658 (2017).

[33] A. Bottero, *Analysis of a two species TASEP as a model for heterogeneous transport on microtubules*, Master thesis, Ludwig-Maximilians-Universität München (2017).

[34] D. Doody, *Basics of Space Flight* (Bluroof Press, 2011).

[35] F. Tarducci, *The Life of Christopher Columbus* (H.F. Brownson, 1890).

[36] "Creative Commons Attribution-ShareAlike 4.0 International Public License", https://creativecommons.org/licenses/by-sa/4.0/legalcode .

[37] "Wikimedia: Kinetochore", https://commons.wikimedia.org/wiki/File:Kinetochore.jpg .

[38] G. Borisy (EMBL Symposium: Microtubules: From Atoms to Complex Systems, Heidelberg, 2016).

[39] S. Inoué and K. Dan, Journal of Morphology **89**, 423 (1951).

[40] M. C. Ledbetter, The Journal of Cell Biology **19**, 239 (1963).

[41] G. G. Borisy and E. W. Taylor, Journal of Cell Biology **34**, 525 (1967).

[42] G. G. Borisy and E. W. Taylor, Journal of Cell Biology **34**, 535 (1967).

[43] H. Mohri, Nature **217**, 1053 (1968).

[44] K. Roberts, in *Principles of Biolomecular Organization*, edited by G. E. W. Wolstenholme and M. O'Connor (J & A Churchill Ltd, London, 1966).

[45] D. Axelrod, The Journal of Cell Biology **89**, 141 (1981).

[46] M. Adrian, J. Dubochet, J. Lepault, and A. W. McDowall, Nature **308**, 32 (1984).

[47] O. Shimomura, F. H. Johnson, and Y. Saiga, Journal of Cellular and Comparative Physiology **59**, 223 (1962).

[48] M. Chalfie, Y. Tu, G. Euskirchen, W. Ward, and D. Prasher, Science **263**, 802 (1994).

[49] A. A. Hyman, S. Salser, D. N. Drechsel, N. Unwin, and T. J. Mitchison, Molecular Biology of the Cell **3**, 1155 (1992).

[50] E. Nogales, S. G. Wolf, and K. H. Downing, Nature **391**, 199 (1998).

[51] A. A. Hyman, The Journal of Cell Biology **128**, 117 (1995).

[52] L. Bergen and G. Borisy, Electron Microscope Analysis of Seeded Assembly **84**, 141 (1980).

[53] G. B. Pierson, P. R. Burton, and R. H. Himes, Journal of Cell Biology **76**, 223 (1978).

[54] R. H. Wade, D. Chrétien, and D. Job, Journal of Molecular Biology **212**, 775 (1990).

[55] K. Summers and M. W. Kirschner, Journal of Cell Biology **83**, 205 (1979).

[56] T. Horio and H. Hotani, Nature **321**, 605 (1986).

[57] R. Walker, E. O'Brien, N. Pryer, M. Soboeiro, W. Voter, H. Erickson, and E. Salmon, The Journal of Cell Biology **107**, 1437 (1988).

[58] G. Alushin, G. Lander, E. Kellogg, R. Zhang, D. Baker, and E. Nogales, Cell **157**, 1117 (2014).

[59] G. J. Brouhard and L. M. Rice, The Journal of Cell Biology **207**, 323 (2014).

[60] H. P. Erickson and E. T. O'Brien, Annual Review of Biophysics and Biomolecular Structure **21**, 145 (1992).

[61] R. Padinhateeri, A. B. Kolomeisky, and D. Lacoste, Biophysical Journal **102**, 1274 (2012).

[62] M. Caplow and R. Reid, Proceedings of the National Academy of Sciences **82**, 3267 (1985).

Bibliography

[63] M. F. Carlier, D. Didry, and D. Pantaloni, Biochemistry **26**, 4428 (1987).

[64] R. Melki, M. F. Carlier, and D. Pantaloni, Biochemistry **29**, 8921 (1990).

[65] H. Bowne-Anderson, M. Zanic, M. Kauer, and J. Howard, BioEssays **35**, 452 (2013).

[66] P. Bayley, M. Schilstra, and S. Martin, FEBS Letters **259**, 181 (1989).

[67] R. A. Walker, The Journal of Cell Biology **114**, 73 (1991).

[68] C. Duellberg, N. I. Cade, D. Holmes, and T. Surrey, eLife **5**, 1 (2016).

[69] M. F. Carlier, T. L. Hill, and Y. Chen, Proceedings of the National Academy of Sciences **81**, 771 (1984).

[70] M. K. Gardner, B. D. Charlebois, I. M. Jánosi, J. Howard, A. J. Hunt, and D. J. Odde, Cell **146**, 582 (2011).

[71] S. P. Maurer, F. J. Fourniol, G. Bohner, C. A. Moores, and T. Surrey, Cell **149**, 371 (2012).

[72] S. P. Maurer, N. I. Cade, G. Bohner, N. Gustafsson, E. Boutant, and T. Surrey, Current Biology **24**, 372 (2014).

[73] D. Odde, L. Cassimeris, and H. Buettner, Biophysical Journal **69**, 796 (1995).

[74] M. K. Gardner, M. Zanic, C. Gell, V. Bormuth, and J. Howard, Cell **147**, 1092 (2011).

[75] V. Jemseena and M. Gopalakrishnan, Physical Review E **91**, 052704 (2015).

[76] P. Zakharov, N. Gudimchuk, V. Voevodin, A. Tikhonravov, F. I. Ataullakhanov, and E. L. Grishchuk, Biophysical Journal **109**, 2574 (2015).

[77] V. VanBuren, D. J. Odde, and L. Cassimeris, Proceedings of the National Academy of Sciences **99**, 6035 (2002).

[78] P. J. Sammak and G. G. Borisy, Nature **332**, 724 (1988).

[79] L. Cassimeris, The Journal of Cell Biology **107**, 2223 (1988).

[80] J. Howard and A. A. Hyman, Nature Reviews Molecular Cell Biology **10**, 569 (2009).

[81] "Creative Commons Attribution 3.0 Unported licence", https://creativecommons.org/licenses/by/3.0/deed.en .

[82] N. Hirokawa, Y. Noda, Y. Tanaka, and S. Niwa, Nature Reviews Molecular Cell Biology **10**, 682 (2009).

[83] S. S. Brown, Annual Review of Cell and Developmental Biology **15**, 63 (1999).

[84] R. Gavin, International Review of Cytology **173**, 207 (1997).

[85] M. J. I. Müller, S. Klumpp, and R. Lipowsky, Proceedings of the National Academy of Sciences **105**, 4609 (2008).

[86] M. López-Preciado, F. Huber, I. Grigoriev, M. O. Steinmetz, A. Akhmanova, G. H. Koenderink, and M. Dogterom, Nature Communications **5**, 4778 (2014).

[87] B. Prevo, P. Mangeol, F. Oswald, J. M. Scholey, and E. J. G. Peterman, Nature Cell Biology **17**, 1536 (2015).

[88] S. L. Reck-Peterson, A. Yildiz, A. P. Carter, A. Gennerich, N. Zhang, and R. D. Vale, Cell **126**, 335 (2006).

[89] M. E. Porter and K. A. Johnson, Annual Review of Cell Biology **5**, 119 (1989).

[90] C. M. Pfarr, M. Coue, P. M. Grissom, T. S. Hays, M. E. Porter, and J. R. McIntosh, Nature **345**, 263 (1990).

[91] E. R. Steuer, L. Wordeman, T. A. Schroer, and M. P. Sheetz, Nature **345**, 266 (1990).

[92] A. A. Hyman and T. J. Mitchison, Nature **351**, 206 (1991).

[93] J. Gepner, M. Li, S. Ludmann, C. Kortas, K. Boylan, S. J. Iyadurai, M. McGrail, and T. S. Hays, Genetics **142**, 865 (1996).

[94] R. Nambiar, R. E. McConnell, and M. J. Tyska, Cellular and Molecular Life Sciences **67**, 1239 (2010).

[95] I. Rayment, H. Holden, M. Whittaker, C. Yohn, M. Lorenz, K. Holmes, and R. Milligan, Science **261**, 58 (1993).

[96] W. O. Hancock and J. Howard, The Journal of Cell Biology **140**, 1395 (1998).

[97] W. O. Hancock and J. Howard, Proceedings of the National Academy of Sciences **96**, 13147 (1999).

[98] F. Jon Kull, E. P. Sablin, R. Lau, R. J. Fletterick, and R. D. Vale, Nature **380**, 550 (1996).

[99] R. Vale, Cell **112**, 467 (2003).

[100] J. O. Andreasson, B. Milic, G.-Y. Chen, N. R. Guydosh, W. O. Hancock, and S. M. Block, eLife **4**, 1 (2015).

[101] M. Brunnbauer, R. Dombi, T.-H. Ho, M. Schliwa, M. Rief, and Z. Ökten, Molecular Cell **46**, 147 (2012).

[102] W. L. Stepp, G. Merck, F. Mueller-Planitz, and Z. Ökten, EMBO reports **18**, 1947 (2017).

[103] A. Yildiz, M. Tomishige, A. Gennerich, and R. D. Vale, Cell **134**, 1030 (2008).

[104] E. Berliner, E. C. Young, K. Anderson, H. K. Mahtani, and J. Gelles, Nature **373**, 718 (1995).

Bibliography

[105] A. Seitz and T. Surrey, The EMBO Journal **25**, 267 (2006).

[106] V. Bormuth, B. Nitzsche, F. Ruhnow, A. Mitra, M. Storch, B. Rammner, J. Howard, and S. Diez, Biophysical Journal **103**, L4 (2012).

[107] M. Bugiel, E. Böhl, and E. Schäffer, Biophysical Journal **108**, 2019 (2015).

[108] S. Ray, The Journal of Cell Biology **121**, 1083 (1993).

[109] R. Schneider, T. Korten, W. J. Walter, and S. Diez, Biophysical Journal **108**, 2249 (2015).

[110] C. L. Asbury, Science **302**, 2130 (2003).

[111] A. Yildiz, Science **303**, 676 (2004).

[112] W. Hua, E. C. Young, M. L. Fleming, and J. Gelles, Nature **388**, 390 (1997).

[113] W. O. Hancock, Biophysical Journal **110**, 1216 (2016).

[114] S. M. Block, Biophysical Journal **92**, 2986 (2007).

[115] S. S. Rosenfeld, P. M. Fordyce, G. M. Jefferson, P. H. King, and S. M. Block, Journal of Biological Chemistry **278**, 18550 (2003).

[116] L. M. Klumpp, A. Hoenger, and S. P. Gilbert, Proceedings of the National Academy of Sciences **101**, 3444 (2004).

[117] N. R. Guydosh and S. M. Block, Proceedings of the National Academy of Sciences **103**, 8054 (2006).

[118] S. Rice, A. W. Lin, D. Safer, C. L. Hart, N. Naber, B. O. Carragher, S. M. Cain, E. Pechatnikova, E. M. Wilson-Kubalek, M. Whittaker, E. Pate, R. Cooke, E. W. Taylor, R. A. Milligan, and R. D. Vale, Nature **402**, 778 (1999).

[119] B. Milic, J. O. L. Andreasson, W. O. Hancock, and S. M. Block, Proceedings of the National Academy of Sciences **111**, 14136 (2014).

[120] K. J. Mickolajczyk, N. C. Deffenbaugh, J. Ortega Arroyo, J. Andrecka, P. Kukura, and W. O. Hancock, Proceedings of the National Academy of Sciences **112**, E7186 (2015).

[121] B. E. Clancy, W. M. Behnke-Parks, J. O. L. Andreasson, S. S. Rosenfeld, and S. M. Block, Nature Structural & Molecular Biology **18**, 1020 (2011).

[122] H. Isojima, R. Iino, Y. Niitani, H. Noji, and M. Tomishige, Nature Chemical Biology **12**, 290 (2016).

[123] H. Khataee, S. Naseri, Y. Zhong, and A. W.-C. Liew, Molecular Informatics **37**, 1700092 (2018).

[124] S. Verbrugge, S. M. van den Wildenberg, and E. J. Peterman, Biophysical Journal **97**, 2287 (2009).

[125] K. Sozański, F. Ruhnow, A. Wiśniewska, M. Tabaka, S. Diez, and R. Hołyst, Physical Review Letters **115**, 218102 (2015).

[126] G. Goshima, R. Wollman, N. Stuurman, J. M. Scholey, and R. D. Vale, Current Biology **15**, 1979 (2005).

[127] J. Stumpff, G. von Dassow, M. Wagenbach, C. Asbury, and L. Wordeman, Developmental Cell **14**, 252 (2008).

[128] J. Helenius, G. Brouhard, Y. Kalaidzidis, S. Diez, and J. Howard, Nature **441**, 115 (2006).

[129] E. Reithmann, L. Reese, and E. Frey, Biophysical Journal **108**, 787 (2015).

[130] E. Reithmann, L. Reese, and E. Frey, Physical Review Letters **117**, 078102 (2016).

[131] M. Striebel, *Driven lattice gas model of particles with lateral extension*, Master thesis, Ludwig-Maximilians-Universität München (2017).

[132] C. Leduc, K. Padberg-Gehle, V. Varga, D. Helbing, S. Diez, and J. Howard, Proceedings of the National Academy of Sciences **109**, 6100 (2012).

[133] R. Subramanian, S.-C. Ti, L. Tan, S. A. Darst, and T. M. Kapoor, Cell **154**, 377 (2013).

[134] M. Eckl, *A Region Capture Mechanism with Maturation Kinetics for Molecular Motors on Microtubules*, Master thesis, Ludwig-Maximilians-Universität München (2016).

[135] P. W. K. Rothemund, Nature **440**, 297 (2006).

[136] S. M. Douglas, H. Dietz, T. Liedl, B. Högberg, F. Graf, and W. M. Shih, Nature **459**, 414 (2009).

[137] J. Bath and A. J. Turberfield, Nature Nanotechnology **2**, 275 (2007).

[138] R. D. Astumian, Biophysical Journal **98**, 2401 (2010).

[139] A. V. Pinheiro, D. Han, W. M. Shih, and H. Yan, Nature Nanotechnology **6**, 763 (2011).

[140] W. B. Sherman and N. C. Seeman, Nano Letters **4**, 1203 (2004).

[141] J.-S. Shin and N. A. Pierce, Journal of the American Chemical Society **126**, 10834 (2004).

[142] M. von Delius and D. A. Leigh, Chemical Society Reviews **40**, 3656 (2011).

[143] Y. Tian, Y. He, Y. Chen, P. Yin, and C. Mao, Angewandte Chemie International Edition **44**, 4355 (2005).

[144] T. Krüger, *Brownian Dynamics Simulations of Soft Materials*, Master thesis, Ludwig-Maximilians-Universität München (2015).

[145] T. Chou, K. Mallick, and R. K. P. Zia, Reports on Progress in Physics **74**, 116601 (2011).

[146] C. T. MacDonald, J. H. Gibbs, and A. C. Pipkin, Biopolymers **6**, 1 (1968).

[147] F. Spitzer, Advances in Mathematics **5**, 246 (1970).

[148] K. Nagel and M. Schreckenberg, Journal de Physique I **2**, 2221 (1992).

[149] P. L. Krapivsky, S. Redner, and E. Ben-Naim, *A Kinetic View of Statistical Physics* (Cambridge University Press, 2010).

[150] B. Derrida, M. R. Evans, V. Hakim, and V. Pasquier, Journal of Physics A: Mathematical and General **26**, 1493 (1993).

[151] R. A. Blythe and M. R. Evans, Journal of Physics A: Mathematical and Theoretical **40**, R333 (2007).

[152] A. B. Kolomeisky, G. M. Schütz, E. B. Kolomeisky, and J. P. Straley, Journal of Physics A: Mathematical and General **31**, 6911 (1998).

[153] C. Appert-Rolland, M. Ebbinghaus, and L. Santen, Physics Reports **593**, 1 (2015).

[154] R. Lipowsky, S. Klumpp, and T. M. Nieuwenhuizen, Physical Review Letters **87**, 108101 (2001).

[155] A. Parmeggiani, T. Franosch, and E. Frey, Physical Review Letters **90**, 086601 (2003).

[156] A. Parmeggiani, T. Franosch, and E. Frey, Physical Review E **70**, 046101 (2004).

[157] K. Sugden, M. Evans, W. Poon, and N. Read, Physical Review E **75**, 031909 (2007).

[158] M. Evans and K. Sugden, Physica A: Statistical Mechanics and its Applications **384**, 53 (2007).

[159] K. E. P. Sugden and M. R. Evans, Journal of Statistical Mechanics: Theory and Experiment **2007**, P11013 (2007).

[160] S. Nowak, P.-W. Fok, and T. Chou, Physical Review E **76**, 1 (2007).

[161] D. A. Adams, B. Schmittmann, and R. K. P. Zia, Journal of Statistical Mechanics: Theory and Experiment **2008**, P06009 (2008).

[162] L. J. Cook and R. K. P. Zia, Journal of Statistical Mechanics: Theory and Experiment **2009**, P02012 (2009).

[163] P. Greulich, L. Ciandrini, R. J. Allen, and M. C. Romano, Physical Review E **85**, 011142 (2012).

[164] L. Ciandrini, I. Neri, J. C. Walter, O. Dauloudet, and A. Parmeggiani, Physical Biology **11**, 056006 (2014).

[165] C. A. Brackley, L. Ciandrini, and M. C. Romano, Journal of Statistical Mechanics: Theory and Experiment **2012**, P03002 (2012).

[166] L. B. Shaw, R. K. P. Zia, and K. H. Lee, Physical Review E **68**, 021910 (2003).

[167] G. Lakatos and T. Chou, Journal of Physics A: Mathematical and General **36**, 2027 (2003).

[168] P. Pierobon, M. Mobilia, R. Kouyos, and E. Frey, Physical Review E **74**, 1 (2006).

[169] V. Popkov and I. Peschel, Physical Review E **64**, 026126 (2001).

[170] A. Melbinger, T. Reichenbach, T. Franosch, and E. Frey, Physical Review E **83**, 031923 (2011).

[171] E. Pronina and A. B. Kolomeisky, Journal of Physics A: Mathematical and General **37**, 9907 (2004).

[172] T. Reichenbach, E. Frey, and T. Franosch, New Journal of Physics **9**, 159 (2007).

[173] M. R. Evans, Y. Kafri, K. E. P. Sugden, and J. Tailleur, Journal of Statistical Mechanics: Theory and Experiment **2011**, P06009 (2011).

[174] I. R. Graf and E. Frey, Physical Review Letters **118**, 6 (2017).

[175] P. Wilke, E. Reithmann, and E. Frey, in preparation (2018).

[176] S. Katz, J. L. Lebowitz, and H. Spohn, Physical Review B **28**, 1655 (1983).

[177] S. Katz, J. L. Lebowitz, and H. Spohn, Journal of Statistical Physics **34**, 497 (1984).

[178] H. Teimouri, A. B. Kolomeisky, and K. Mehrabiani, Journal of Physics A: Mathematical and Theoretical **48**, 065001 (2015).

[179] H. D. Vuijk, R. Rens, M. Vahabi, F. C. MacKintosh, and A. Sharma, Physical Review E **91**, 032143 (2015).

[180] J. Messelink, R. Rens, M. Vahabi, F. C. MacKintosh, and A. Sharma, Physical Review E **93**, 012119 (2016).

[181] Y. Chai, S. Klumpp, M. J. I. Müller, and R. Lipowsky, Physical Review E **80**, 041928 (2009).

[182] M. Song and Y. Zhang, Canadian Journal of Physics **95**, 370 (2017).

[183] I. Pinkoviezky and N. S. Gov, Physical Review Letters **118**, 1 (2017).

[184] P. Hänggi, Reviews of Modern Physics **81**, 387 (2009).

[185] O. Semenov, M. J. Olah, and D. Stefanovic, Physical Review E **83**, 021117 (2011).

[186] L. Samii, H. Linke, M. J. Zuckermann, and N. R. Forde, Physical Review E **81**, 1 (2010).

[187] L. Samii, G. Blab, E. H. Bromley, H. Linke, P. M. Curmi, M. Zuckermann, and N. Forde, Physical Review E **84**, 1 (2011).

[188] M. A. Jordan and L. Wilson, Nature Reviews Cancer **4**, 253 (2004).

Bibliography

[189] J. Howard and A. A. Hyman, Current Opinion in Cell Biology **19**, 31 (2007).

[190] M. I. Mayr, S. Hümmer, J. Bormann, T. Grüner, S. Adio, G. Woehlke, and T. U. Mayer, Current Biology **17**, 488 (2007).

[191] L. Reese, A. Melbinger, and E. Frey, Interface Focus **4**, 20140031 (2014).

[192] J. D. Wilbur and R. Heald, eLife **2**, e00290 (2013).

[193] L. J. Cook, R. K. P. Zia, and B. Schmittmann, Physical Review E **80**, 031142 (2009).

[194] C. A. Brackley, M. C. Romano, and M. Thiel, Physical Review E **82**, 051920 (2010).

[195] L. Mohapatra, B. L. Goode, P. Jelenkovic, R. Phillips, and J. Kondev, Annual Review of Biophysics **45**, 85 (2016).

[196] L. Mohapatra, T. J. Lagny, D. Harbage, P. R. Jelenkovic, and J. Kondev, Cell Systems **4**, 559 (2017).

[197] S. Klumpp and R. Lipowsky, Journal of Statistical Physics **113**, 233 (2003).

[198] M. L. Gupta, P. Carvalho, D. M. Roof, and D. Pellman, Nature Cell Biology **8**, 913 (2006).

[199] C. E. Walczak, S. Gayek, and R. Ohi, Annual Review of Cell and Developmental Biology **29**, 417 (2013).

[200] G. J. Brouhard, J. H. Stear, T. L. Noetzel, J. Al-Bassam, K. Kinoshita, S. C. Harrison, J. Howard, and A. A. Hyman, Cell **132**, 79 (2008).

[201] D. T. Gillespie, The Journal of Physical Chemistry **81**, 2340 (1977).

[202] Y. Jeune-Smith and H. Hess, Soft Matter **6**, 1778 (2010).

[203] J. Krug, Physical Review Letters **67**, 1882 (1991).

[204] E. Frey, A. Parmeggiani, and T. Franosch, Genome informatics. International Conference on Genome Informatics **15**, 46 (2004).

[205] S. H. Strogatz, *Nonlinear Dynamics and Chaos* (Westview Press, 2014).

[206] J. Halatek and E. Frey, Nature Physics **14**, 507 (2018).

[207] E. D. Salmon, W. M. Saxton, R. J. Leslie, M. L. Karow, and J. R. McIntosh, Journal of Cell Biology **99**, 2157 (1984).

[208] M. Castoldi and A. V. Popov, Protein Expression and Purification **32**, 83 (2003).

[209] T. Korten, B. Nitzsche, C. Gell, F. Ruhnow, C. Leduc, and S. Diez, "Fluorescence Imaging of Single Kinesin Motors on Immobilized Microtubules," in *Single Molecule Analysis: Methods and Protocols*, edited by E. J. G. Peterman and G. J. L. Wuite (Humana Press, Totowa, NJ, 2011) pp. 121–137.

[210] F. Ruhnow, D. Zwicker, and S. Diez, Biophysical Journal **100**, 2820 (2011).

[211] Z. Shang, K. Zhou, C. Xu, R. Csencsits, J. C. Cochran, and C. V. Sindelar, eLife **3**, e04686 (2014).

[212] S. Ghaemmaghami, W.-K. Huh, K. Bower, R. W. Howson, A. Belle, N. Dephoure, E. K. O'Shea, and J. S. Weissman, Nature **425**, 737 (2003).

[213] R. D. Vale, T. S. Reese, and M. P. Sheetz, Cell Methods in Molecular Biology, **42**, 39 (1985).

[214] N. Hirokawa and R. Takemura, Nature Reviews Neuroscience **6**, 201 (2005).

[215] A. Akhmanova and M. O. Steinmetz, Nature Reviews Molecular Cell Biology **9**, 309 (2008).

[216] E. Muto, H. Sakai, and K. Kaseda, The Journal of Cell Biology **168**, 691 (2005).

[217] W. H Roos, O. Campàs, F. Montel, G. Woehlke, J. P. Spatz, P. Bassereau, and G. Cappello, Physical Biology **5**, 046004 (2008).

[218] P. Pierobon, E. Frey, and T. Franosch, Physical Review E **74**, 031920 (2006).

[219] D. Celis-Garza, H. Teimouri, and A. B. Kolomeisky, Journal of Statistical Mechanics: Theory and Experiment **2015**, P04013 (2015).

[220] S. Chandel, A. Chaudhuri, and S. Muhuri, EPL (Europhysics Letters) **110**, 18002 (2015).

[221] A. K. Gupta, Journal of Statistical Physics **162**, 1571 (2016).

[222] R. D. Vale, T. Funatsu, D. W. Pierce, L. Romberg, Y. Harada, and T. Yanagida, Nature **380**, 451 (1996).

[223] J. Howard, Annual Review of Physiology **58**, 703 (1996).

[224] M. F. Weber and E. Frey, Reports on Progress in Physics **80**, 046601 (2017).

[225] S. M. Block, C. L. Asbury, J. W. Shaevitz, and M. J. Lang, Proceedings of the National Academy of Sciences **100**, 2351 (2003).

[226] N. R. Guydosh and S. M. Block, Nature **461**, 125 (2009).

[227] S. Klumpp and T. Hwa, Proceedings of the National Academy of Sciences **105**, 18159 (2008).

[228] S. Klumpp, Journal of Statistical Physics **142**, 1252 (2011).

[229] J. Wang, B. Pfeuty, Q. Thommen, M. C. Romano, and M. Lefranc, Physical Review E **90**, 050701 (2014) .

[230] I. Pinkoviezky and N. S. Gov, New Journal of Physics **15**, 025009 (2013).

[231] I. Pinkoviezky and N. S. Gov, Physical Review E **88**, 022714 (2013).

[232] M. L. Moyer, S. P. Gilbert, and K. A. Johnson, Biochemistry **37**, 800 (1998).

[233] S. Klumpp, Y. Chai, and R. Lipowsky, Physical Review E **78**, 041909 (2008).

Acknowledgements

Zunächst möchte ich meinem Doktorvater Erwin Frey Dank aussprechen. Vielen Dank, Erwin, für die schöne Zeit an deinem Lehrstuhl und für die Möglichkeiten, die mir dort eröffnet wurden. Auch wenn es sicher nicht immer die einfachste und schnellste Art war, spannende Effekte zu beobachten, habe ich es sehr genossen, mit deiner Hilfe meine eigene Forschung selbst zu entwickeln und steuern zu dürfen.

I would also very much like to thank my collaboration partners Aniruddha Mitra and Stefan Diez. It was always a pleasure to work and discuss with you and I honestly believe our project is now worth so much more as it would have been with theory alone.

Ebenso dankbar bin ich dir, Louis, dass du mich schon als Betreuer meiner Diplomarbeit unterstützt hast, mir aber gerade zu Beginn meiner Doktorarbeit immer nett und freundlich zur Seite gestanden hast und das bis heute tust.

Während meiner Zeit als Doktorand aber auch schon als Student hatte ich das große Glück, ein Stipendium des Cusanuswerks zu erhalten. Das war finanziell beruhigend, vor allem durfte ich aber in den vielen Ferienakademien und Graduiertentagungen Einblick in so viele interessante Themengebiete erhalten und eine so unglaubliche Dichte interessanter Menschen kennen lernen.

Selbstverständlich gilt mein besonderer Dank auch den vielen netten Leuten am Lehrstuhl, die ich über die Jahre sehr zu schätzen gelernt habe. Zunächst ist das natürlich mein Bürokollege, der "andere Matthias", den ich in den letzten sechs Jahren wohl so viel gesehen habe wie sonst niemand anderen — besonders, seit er seinen großen Bildschirm abgetreten hat. Ebenso dankbar bin ich aber auch Marianne (für die (gegenseitige) Unterstützung in allen Lebenslagen), Hannes (nicht nur für die GoPro, sondern generell für deine frohe Natur), meinen "Dortmunder Kollegen" Markus und Karl (dafür, dass ihr in der Diaspora stark geblieben seid), Isabella (für deine Hilfsbereitschaft), Cornelius (weil du ungefähr jedes Buch aus der Beck'schen Reihe auswendig kennst) und allen hier namentlich nicht genannten, die zur guten Atmosphäre am Lehrstuhl beigetragen haben.

Großer Dank gilt auch meinen Masterstudenten Timo, Maria, Alessandro und Moritz. Natürlich wäre ein so selbstverantwortliches Arbeiten wie an unserem Lehrstuhl nicht möglich ohne eine gute "Cloud": Ein herzliches Dankeschön also an Louis, Emanuel, Isabella, Patrick, Maria, Mareike, Alessandro und Moritz für die gegenseitige Unterstützung.

Mindestens ein Getränk schulde ich Marianne, Isabella und Emanuel für umfangreiche und wertvolle Kommentare zum Text dieser Arbeit.

Ein ganz besonderer Dank geht natürlich an meine Eltern Angelika und Ernst. Ihr habt mir ein (gründliches) Studium ermöglicht und mich generell immer in Allem, was ich tun wollte, unterstützt.

Ganz am Ende, sozusagen auf dem "Ehrenplatz" steht aber die, die meine Launen in den letzten Wochen vor Abgabe dieser Arbeit aber auch schon davor am direktesten miterlebt hat. Danke, dass du da bist, Ramona.